UAB

Universitat Autònoma de Barcelona

Synthesis and characterization of ZnO finewires for the conceptual design of a mechanical battery

Ph. D. Thesis written by

Oscar Gilberto Súchil Pérez

Under the supervision of

Francesc Torres and Gabriel Abadal

Electronic Circuits and Systems and NOEMS for energy laboratory

Bellaterra (Cerdanyola del Vallès), May 2017

The undersigned, Dr, **Francesc Torres and Gabriel Abadal**,

Professors of the Electronic Engineering Department (Engineering School) of the *Universitat Autònoma de Barcelona*,

CERTIFY:

That the thesis entitled "Synthesis and characterization of ZnO finewires for the conceptual design of a mechanical battery" has been written by **Oscar Gilberto Súchil Pérez** under their supervision, in fulfillment of the requirements for the PhD degree of Electronic Engineering.

And hereby to acknowledge the above, sign the present.

Frances Torres   Gabriel Abadal

Bellaterra (Cerdanyola del vallès, May 2017)

Acknowledgments

Oscar Gilberto Súchil Pérez

Barcelona, 2017

Abstract

The synthesis and characterization for a ZnO array have been done with the aim of fabricate an experimental battery that uses the strain energy as energy source. The storage principle is based on a common spring which is loaded by the force associated to the energy to be harvested. By following the same principle our approach is based on pressing an array of fine wires (fws) grown vertically on a substrate surface. The ZnO has been chosen as a fabrication material due fine wires growth is cheap and simple using the hydrothermal method. By taking the best aligned ZnO array samples obtained from our previous experiments the characterization was performed in two phases, firstly a statistical study was computed for quantify the ZnO fws physical dimensions as average density, diameters and lengths. Secondly a mechanical study for a single fine wire was done applying the linear elastic theory and later corroborated by a FEM simulation. The boundary conditions free-fixed and pinned-fixed as possible behaviors were considered. Finally the fine wires array was submitted to a compression test in order to see the deformation levels and energy storage capability as an experimental reference.

Resumen

La caracterización de arreglos de micro hilos de óxido de Zinc (ZnO) se ha realizado con la finalidad de diseñar una batería experimental que utiliza la energía de deformación como fuente de energía. El principio de almacenamiento esta basado en la compression simple de un muelle cuya fuerza de compression se encuentra asociada a la energía que es cosechada. Mediante el mismo principio se propone la compression de un arreglo de nanohilos de ZnO crecidos de forma alineada perpendiculars al sustrato de crecimiento, funcionando como muelles elásticos que almacenen energía en un medio enteramente mecánico. El ZnO se ha elegido por ser un material en el que se pueden crecer nanoestructuras con forma de hilos, barras y filamentos de manera sencilla y de bajo coste a través de un método de síntesis llamado método hidrotérmico.

Tomando en cuenta las mejores muestras alineadas de microhilos de ZnO, se realizó un proeso para su caracterización mecánica en dos fases principales. La primera fase coniste en el estudio estadístico para dimensionar su morfología y tamaños asaí como su densidad de crecimiento media por toda la muestra. En segundo lugar se llevó a cabo la realización de la aplicación de la teoría lineal elástica que después fue corroborada y replicada con simulaciones de elementos finitos (FEM). Las condiciones de contorno consideradas como comportamientos posibles en los microhilos de ZnO fuero libre-empotrado y articulado-empotrado. Finalmente los microhilos se sometieron a pruebas de compresión simple utilizando un nanoindentador comercial, para llevar a cabo el análisis experimental puntual de las propiedades del material del que se conforman y así determinar la discrepancia con el modelo teórico así como su capacidad de almacenamiento de energía real.

Index

LIST OF FIGURES

List of tables

List of equations

Abbreviations

ACG	Aqueous Chemical Growth
AlN	Aluminum Nitride
CVTC	Chemical vapor transport and condensation
HCl	Chloride Acid
CCS	Customized Compression Set-Up
Fws	Fine wires
FEM	Finite Element Method
GaN	Galium Nitride
GPa	Giga Pascal
$(CH_2)_6N_4$	Hexamine
HMTA	Hexamine
HTM	Hydrothermal Method
HTM	Hydrothermal Method
ITO	Indium Tin Oxide
MESS	Mechanical Energy Storage System
MOCVD	Methal Organic Chemical Vapor Deposition
NWs	Nano wires
OCS	Optical Calibration System
OFWs	Optical Fiber Wires
PET	Polyethylene terephthalate
PDMS	Polydimethylsiloxane
SEM	Scanning Electron Microscope
Si	Silicon
TMAH	Tetra methyl ammonium hydroxide
TEM	Transmission electron microscophy
VLS	Vapor Liqud Solid
Wz	Wurtzite
Zn	Zinc
ZAH	Zinc Acetate Hydrate
$Zn(OH)_2$	Zinc Hydroxide
Zn^{2+}	Zinc Ion
$Zn(NO_3)_2*6H_2O$	Zinc Nitrate Hexahydrate
ZnO	Zinc Oxide
ZnOfws	Zinc Oxide Finewires
ZnOHMRs	Zinc Oxide Hexagonal Micro Rods
ZnONWs	Zinc Oxide Nano wires
ZnONRs	Zinc Oxide Rods

Chapter 1.   INTRODUCTION

D ue to a continuous growth on the energy demand and a continous aim on diminish the dependence on fossil fuels as the main energy source, renewable energy sources have gained importance in study. Therefore, as collateral need, the energy storage systems have been adapted to the new energy alternatives.

Since the first electrochemical battery was developed in the eighteenth century, the energy storage systems have been evolving in order to fulfill the energy storage demands. For instance, from a macro-scale point of view, the energy storage plays a critical role in the electrical energy generation plants, because they are used to stabilize the supply-demand or to bring an extra amount of energy if the demand is higher than expected. On the other hand, at a micro/nano scale point of view, the electronic industry and the mobile technologies have provoked also the research and development of new energy storage systems, focused on storing energy to supply microelectronic circuits and also MEMS/NEMS devices with specific requirements.

Therefore, in this chapter a brief description of the energy storage systems at three different dimentions levels is explained. Later, the importance of center our study in energy storage in the mechanical domain, including a global view of the literature on previous studies that have been used as background for this work, are also reported.

Finally, the general outline for this thesis is described, with the main goals to accomplish during the research, as well as the methodology followed for the conceptualization of a mechanical energy storage system (*MESS)*, taking into account diferent strategies and materials.

1.1   Energy storage systems

1.1.1   Energy storage systems at macro-scale

Nowadays, the electrical energy represents 12% of total energy processed by humanity, is predicted to grow in the next eight years up to 34%[1], due to the costumers demand.

The introduction of alternative renewable sources to the electrical grid, and the continuous need of delocalize electricity, increases the difficulty of stabilize the power network. Therefore, it is a critical need not just to generate, transmit and convert the energy but also to store it.

To store electrical energy it has to be transformed first, for later transform it back when it is required. Some of the main forms of energy storage are mechanical, chemical and thermal, and they can be grouped in four principal categories (see Figure 1-1).
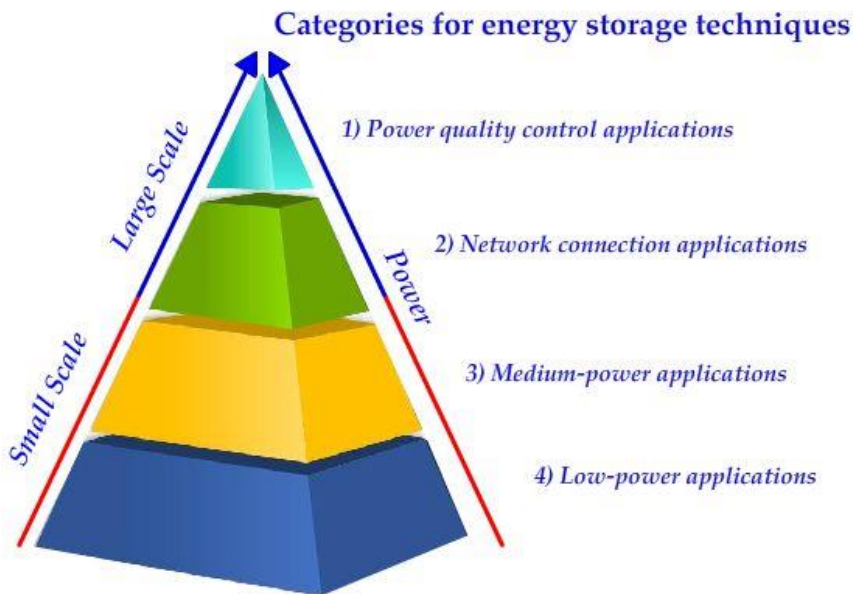
Figure 1-1: Categories for energy storage techniques according with its application

The energy storage techniques are associated to their field of application, and as a consequence, to the amount of power that they can supply. For the large scale, the energy storage can reach from 10 to 10^4 MWh.   For small scale, the energy storage can go from 1 kWh to 10 MWh. In order to explain the applications of all these categories a list of some examples for each scale is summarized below.

1.1.1.1   Large-scale energy storage techniques

Pumped hydro storage (PHS): it uses water as energy storage material**.** Its working principle is based on two states: first the *Accumulation* state appears when the energy demand is low and the conventional electricity is used to pump water from a lower reservoir to the upper reservoir. Secondly, on the *Restitution* state, demand is high again and the water flows out the upper reservoir activating the turbines to generate power. The

stored energy on these plants can reach **272 Wh** per ton of mass falling at 100 m, giving in consequence tens of GWh with efficiency of about 65-80%[1][2].

Thermal energy storage (TES): there are two types of TES systems according to their energy storage material used: latent heat or sensible heat. For the latent heat TES, the energy is stored in a liquid-solid transition of a material at a constant temperature. The energy storage starts when the bulk material shifts from solid to liquid. Then, the heat is transferred between a thermal accumulator and the exterior environment through a heat-transfer fluid. Sodium hydroxide is oftenly used as a good storage fluid with an energy storage capacity of **206 kWh** per ton. On the other hand, the sensible heat TES stores energy in a bulk material as for instance, sodium or molten salt. But for this case, the material do not change states during energy storage, in consequence no transfer fluid is needed. Once material is heated, this heat is recovered to produce water vapor, which drives a turbo-alternator system generating electrical energy, the stored energy can achieve up to **40 MWh** [1][2].

Compressed air energy storage (CAES): this technique is used as an additional energy storage source for a conventional power plant. It improves its fuel consumption, by expanding air in a combustion chamber before feeding into the turbines. Residual heat from the smoke is recovered and used for heat air. It uses compressed air, which is stored at high pressures (40 to 70 bars) at ambient temperature. Air is compressed during the off-peak hours with electricity on chambers. Once is compressed, during high peak hours is heated with residual heat, and conducted to activate a turbine for generate electricity. The stored energy is about **12 kWh** per m^3 with an efficiency of 70% [1][2].

1.1.1.2   Small-scale energy storage techniques

Flywheel energy storage (FES): it uses the *kinetic energy* from a composite flywheel coupled with a motorgenerator and special brackets, housed in a low pressure environment to avoid selfdischarges. Its estimated energy storage capacity can reach up to **200 kW,** with an efficiency which starts from 85% dropping to 78% after 5h and, after a day, decreasing to 45%. On large installations of forty flywheels with output of **25 kWh** each, a stored energy capacity of about **1MW** can be realeased in 1h [1][2].

Supercapacitor (SC): it uses the generation of an electric field between two electrodes as energy storage principle, similar to a capacitor, but instead of using an insulating material between electrodes, it is used an electrolyte ionic conductor. Due to the fact that the rate of output voltage of a single unit do not exceeds 2.5 or 3 V, a serial connection is needed. These modules can reach a stored energy of about **500Wh** with a 95% efficiency, susceptible to selfdischarges of about 5% per day [1][2].

Fuel cells Hydrogen energy storage (FC-HES): it uses the oxidation-reduction processs between hydrogen and oxygen, as energy storage principle, which ocurrs between two electrodes separated by an electrolyte. Once electricity is generated, hydrogen and oxygen are combined to form water. To restart energy storage cycle this water has to be separated in hydrogen and oxygen by an electrolyzer. Due to the fact that it is necessary an electrolyzer with an efficiency of 70%, and a fuel cell with efficiency of 50%, its total efficiency is of 35% with a stored energy of **100 kWh**[3],[4]. The previously energy storage

techniques are summarized in Figure 1-2 .
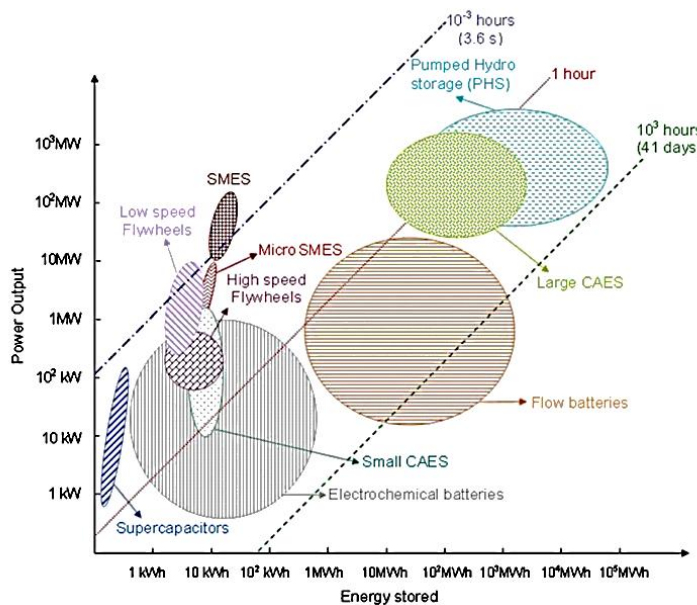
Figure 1-2: Different energy storage techniques categorized by output power and energy stored [5]

Once the energy storage systems at macro-scale have been described, in the next section a brief description for energy storage systems from micro and nano scale point of view will be reported.

1.1.2   Energy storage systems at micro/nano-scale

As it was noticed in the previous section, the energy storage systems are designed depending on the final application where they will be used and, in consequence, the energy storage capacity can be suitable by the same criteria. In this section, a view on energy storage systems at a micro and nano scale will be reported, explaining as before the different techniques that are common used in MEMS/NEMS and Nanotechnology industry.

1.1.2.1   Micro-scale energy storage applications

Micro fuel cell (MFC): its working principle uses two different ways: the first way uses a *direct energy conversion* which may involve fuels such as methanol, ethanol, formic acid or ethylene, which can be converted into electrons through a direct fuel cell system. The second way uses an *indirect energy conversion,* which involves a reformation of a gas[1] (methanol, ethanol or sodium borohydride) to produce hydrogen, followed by feeding a fuel cell with this reformate gas. For a micro-scale, *MFCs* can reach a maximum power capability less than *5W*[6]. Other types of *MFCs* fabricated by different companies and laboratories, like micro-formic acid fuel cell or hydrogen fed micro fuel cell, can store

---

[1] Reforming gas: is a method for producing hydrogen, carbon monoxide, or other products from hydrocarbon fuels such as natural gas. It ocurrs through a processing device, called a reformer which reacts steam at high temperature with fossil fuel. A steam methane reformer is widely used in industry to make pure hydrogen[143].

different energy levels of *2.77Wh*[7]*,0.33Wh*[8]*, 0.4Wh*[9] and *2Wh*[10].

Micro Li-ion battery (MLiB): its main difference compare to conventional *Li-ion* batteries, is that *MLiBs* do not required a separator, due to it is a solid state microbattery. Therefore, the overall mass of the cell decreases, causing an increase in the energy density per unit of mass[11]. Since the miniaturization of the battery, the diffusion path of the ions is also decreased and the ionic and electronic conduction depend only in the electrode material. Therefore, the electrode thickness gives the overall resistance for the *MLiBs* and then, if the thickness is increased, the resistence is also increased. Their main variation is based on the selection of materials and electrochemical couples. Some examples are: *MLiBs 3dNickelSulphide electrode* with a surface current capacity of *1.5mAh/cm²,* or *Ink-jet printed porous of Lithium iron phosphate (LiFePO₄) electrode* with surface current capactiy of *300µAh/cm²* [12]–[14]*.*

Micro Supercapacitor (MSC): its working principle is similar to *SC* but its miniaturization increases the energy density that could be delivered at a higher efficiency [15]. They have a higher power density, long cycle life, large rate capability and less environmental harmful[16].As in the case of *MLiBs,* their electrodes can be fabricated by different techniques, for instance the *Ink-jet printed MWCNTs/Ag ink* with a energy density of *1.28 mWh/cm³* [17], or using the screen printing technique with PVA-H₃PO₄ as gel electrolyte, that can reach a energy density of *0.3 mWh/cm³* [18] and for laser printing technique *MSC* on Polyethylene Terephthalate (PET) substrate, that can reach a current density of *0.1 mA/cm³* and a volumetric energy density of *5.83 mWh/cm³*[19].

1.1.2.2   Nano-scale of energy storage applications

Hybrid electrochemical energy storage using Ni-Sn/PANI nanowires: developed as an hybrid technology between a battery and a supercapacitor, *Sanket R.Gowda et al* [20] developed a composite nanostructured for an electrochemical device with an anode (Ni-Sn) and a cathode (polyaniline, PANI) (nanowires). The system uses the nanowires packaged, within a polymer core-shell separator. Its working principle is divided into two separated processes. During the *charge process* Li ion insertion takes place into the Ni-Sn electrode through electrochemical alloying mechanism and PF₆ ions doped into the polyaniline electrode. For the discharge *process,* the process consists in the Li ion deinsertion and PF₆ ion undoping from Ni-Sn and PANI electrodes respectively. In this system, the parallel array can reach a surface energy storage of about *3µAh/cm²*.

Carbon Nano Tubes (CNTs) used to enhance fuel cell performance: eventhough fuel cells have a high reliable effectiveness in transform chemical to electrical energy. In order to perform this transformation, the use of Platinum (Pt) as a catalyst is necessary and the size of the Pt particles have a high contribution on the effectiveness in energy transformation.

Its deposition is patterned over the support structure[21], nevertheless Pt has a poor catalyst loading per unit area. This improvement can be done by adding catalyst support materials, with superior specific surface and electrochemical stability, when there are subjected to fuel cell working conditions. To achieve this goal, common catalyst supports are include, as it can be carbon (C), graphene or nanomaterials as carbon nano tubes (*CNTs*).Using *CNTs* gives several advantages for instance: superior surface area, electrical conductivity, lighter weight and remarkable mechanical and electro-chemical characteristics. *Pt/CNTs supports* have a power density of about *400 mW/cm²*, which is higher in comparison with *Pt/C supports 360 mW/cm²*.

1.1.3   Storing energy in the mechanical domain

As it was mentioned in the two previous sections, a growing interest on develop new energy storage strategies have become a constant necessity. In this section the main reasons for study the energy storage in the mechanical domain are explained.

Firstly, is necessary to take a look at a micro-scale for those microdevices that capture its own energy from the environment. These devices are also known as *energy harvesters,* which collect its energy from different energy residual sources for instance: heat, light, sound or mechanical vibrations (see Figure 1-3). Their main use is dedicated to improve efficiency on microelectronic systems. They can help to enable new technologies as wireless network sensors or for replace batteries on small and low power electronic devices. These combined systems are also known as *maintenance free* or *unmanned systems*[22].
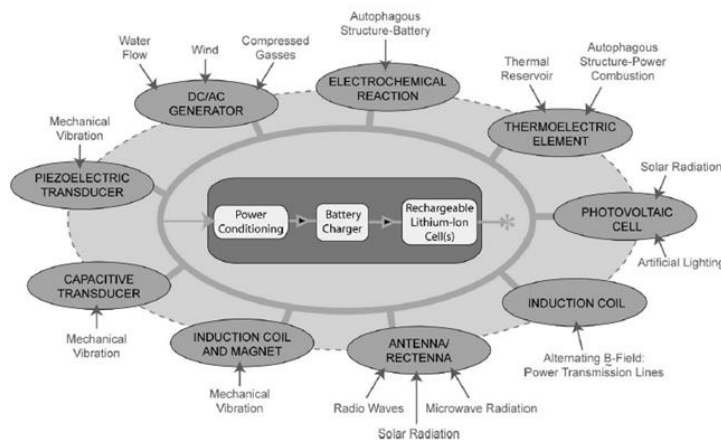
Figure 1-3: Different scavengable energies that can be converted and later used by small unmanned systems[23]

For these systems, the energy first has to be collected, then transformed and finally stored, in order to feed the unmanned systems. The main issue of this process, which sacrifices efficiency for the energy storage, lies in the energy losses that occur between each energy

conversion. Therefore, trying to reduce these energy losses, the mechanical energy harvesters are selected to propose the next system shown on Figure 1-4.
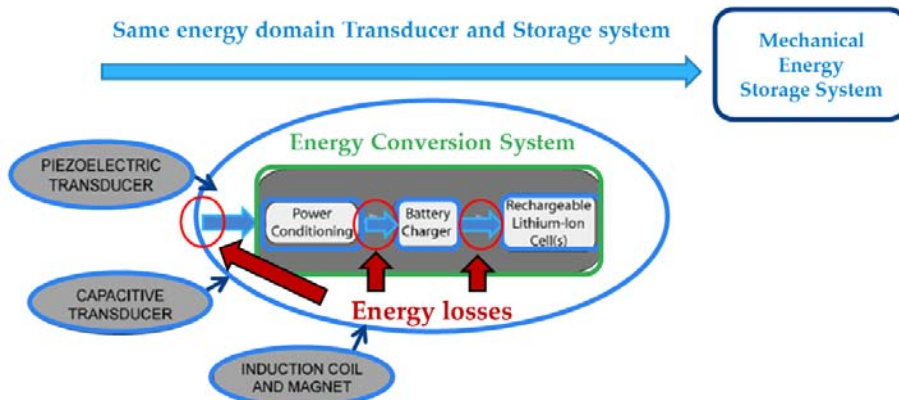
Figure 1-4: Mechanical energy storage system (MESS) proposal to help reduce energy losses on mechanical energy harvesters.

The main importance described on Figure 1-4 is that, rather than convert the energy each time, it is proposed as more beneficial keeping the same domain, from harvest to the energy storage, avoiding with this the possible energy losses that can ocurr at the conversion system. Some of the main conceptual advantages of a *MESS* are listed below:

1) *Longer operation life:* if energy is stored in a complete mechanical process, rather than an electrochemical process, a longer life for the storage system could be reached. This may occur, due to the fact that the materials have an aging degradation or fatigue process. This aging process can be slower and less harmful than the chemical degradation during the electrolysis process, in the case of the electro-chemical batteries.

2) *Low self-discharge*: for the electro-chemical batteries, its energy stored is reduced, depending on the internal chemical reactions or environmental temperature, suffering self-discharges, even when are not in use, up to 20% monthly[24]. If energy is stored in a mechanical process, during operation the materials can be exposed to possible fatigue with use or, in the case that the environmental temperature reaches levels on which thermal deformation can appear, the materials can suffer a plastic deformation and, consequently reduces significantly its performance.

3) *Quick release of energy*: the electro-chemical batteries have the best efficiency when the discharge is slow, in comparison a mechanical energy storage system can release a high amount of energy quickly without compromising its efficiency [24].

1.2   General approach to the mechanical energy storage system

In this section, we present a literature review focused on previous works done, for store mechanical energy. Then, the main works that were used for the *MESS* proposal are highlighted.

The reviewed literature is described in three different categories that are listed below:

1) **Category 1:** *"Mechanical energy storage on micro systems"*

2) **Category 2:** *"Mechanical energy storage on Nanotubes"*

3) **Category 3:** *"Mechanical energy harvesting with Nanowire interfaces"*

1.2.1   Category 1: "Mechanical energy storage on MEMS"

Storing mechanical energy through a MEMS rapid release system

In this work *M.Steven Rodgers et al*[25] present a complex MEMS low-power micromachined electrostatic actuation system that stores energy in the mechanical domain. Energy storage is based on the use of a 5-level microengine[26] and transmission assemblies conformed by 18 cantilever beams paired together, in order to create a system that has a total of 9 "medieval crossbow-shape" with a central shaft.The energy is stored in the 9 bow-beams deflection created by the displacement of the rack, caused by the micro engine transmission. The central shaft is connected to the microengine transmission by a polysilicon filament, an array of 3 carrying springs. For release the energy stored, once the 9 bow-beams are loaded and voltage is applied through the 3 current carrying springs, and when this voltage is high enough, the polysilicon filament blows, transforming the potential energy stored in a mechanical deformation to a kinetic energy that is later directed to a mechanical load (see Figure 1-5).
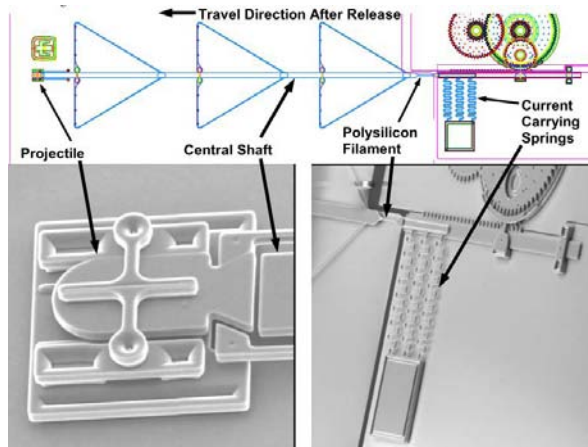
Figure 1-5: At left the small projectile that is later ejected by the impact from the central shaft after the polysilicon filament is blown. At right the polysilicon filament connected with the central shaft is shown.

The energy stored in the system was approach as a function of the deflection from the bow-beams reaching a maximum peak of **80 nJ** with a maximum deflection of **100 µm.** Its main

disadvantage is that it can be used a single time, since the polysilicon filament is broken, reducing its capability for as a rechargable energy storage device.

Reusable micromechanical energy storage with assembled elastomers

In this work, Sarah Bergbreiter et al[27] present a micromechanical energy storage/quick release system, using micro rubber bands of silicon fabricated by two different methods: laser cut and molded. The micro rubbers were assembled in a microstructure fabricated by a two-mask silicion on insulator (SOI) process. The mechanical energy storage is based on the deformation of these micro rubbers. For the first tests of tension, the microrubbers achieve strain levels of *200%,* storing a maximum strain energy of about *19 µJ*. The microrubbers were embedded later in a fully integrated micromechanical energy storage system (see Figure 1-6) with the addition of an electrostatic inchworm motor, in order to stretch the microrubbers, performing the storage and release the energy. After the integration of the overall system, an estimated energy of *4.9 nJ* was stored.

The maximum energy stored is calculated for the elastomer according with the maximum energy that can be stored in a beam under tension. The heat on the spring material appears to be an important parameter for the spring efficiency, due to the fact that the energy is lost in heat form. For the microrubber fabrication, it was observed that Silicon is better than polymers, due to its rigid crystaline nature. The energy losses are smaller than in polymers case, in which the energy is lost accordingly with the dissipation factor. Namely, higher is the dissipation factor larger is the viscosity material and, in consequence, greater the lose of energy. This system is proposed to be used as a storage system for autonomous jumping microbot.
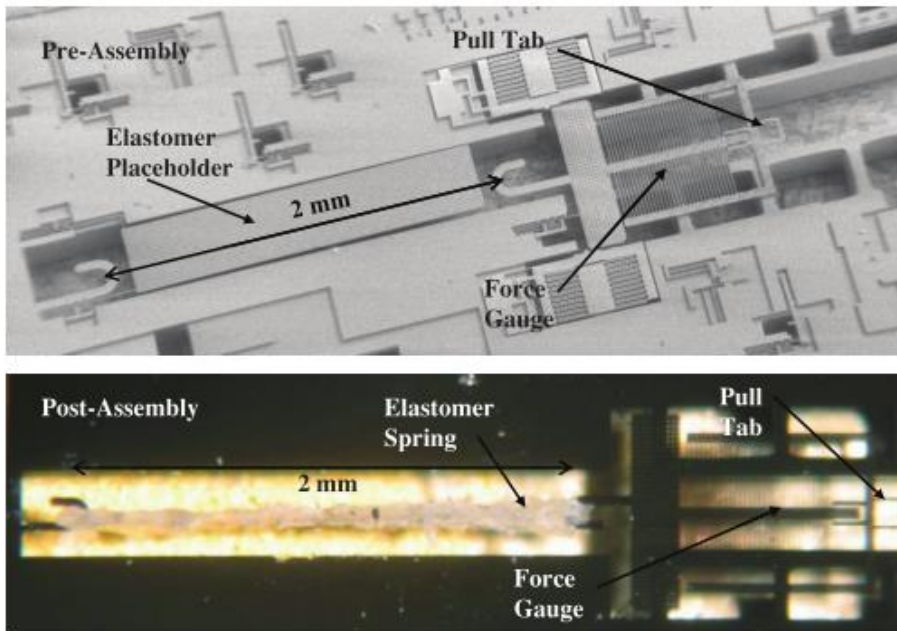
Figure 1-6: The force gauge test structure for characterize the microrruber band

__Approach to a mechanical battery conformed by an electrostatic transducer__

An electrostatic transducer is modified with the use of a nonlinear mechanical spring in order to keep the voltage nearly constant while charge is stored or extracted from the device. The nonlinear spring counteracts the electrostatic attraction forces[28]. Therefore, the transducer, during the performance, responds as a rechargeable battery storing electric charge in elastic deformation.

The nonlinear spring used consists in flexure of a double beam, which are bent over cams guiding their deformation (see Figure 1-7). The displacement of the double beam is driven by a voltage applied to the electrodes that becomes larger as shorter is the gap between electrodes. It was observed that as larger is the contact of the beams with the cam, stiffer is the structure, until a security distance of 1 μm between electrodes (*top/bottom*) is reached. After the structure reaches this security point, it is fixed and there is no more displacement of the top electrode. In consequence, the voltage applied is maintained while a charge is stored or extracted from the system.
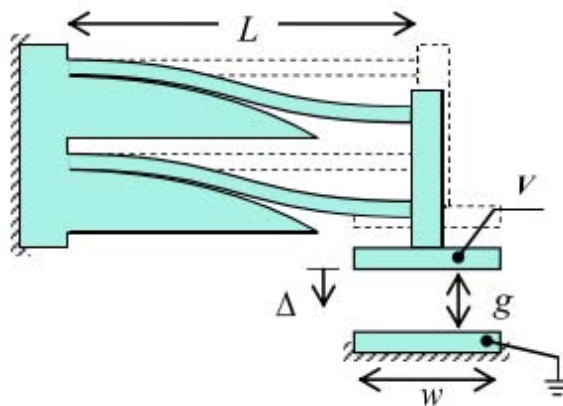
Figure 1-7: Schematic description of the actuator with a nonlinear elastic spring. Two flexures are connected at their far edge, thus constraining edge rotation and imposing parallel motion of the suspended electrode. The stiffness is increased by effectively shortening the beams as they are wrapped over curved cams.

The main advantage of the conceptual mechanical battery mentioned in this work was that the charge/ discharge process may be faster than in chemical batteries, because a mechanical battery avoids the slow process of ion transportation. A clear disadvantage was that the capacitance stored is extremely small, about *30 nF*[29]**.** Therefore, to consider a mechanical battery as an energy storage alternative resource, a redesign that increases considerably this capacitance is needed.

1.2.2   Category 2:"Mechanical energy storage on Nanotubes"

__Storing mechanical energy on carbon nanotubes springs__

There is a growing interest in carbon nanotubes (CNTs) due to its particular physical properties, for instance: metallic conductivity, hight stiffness and axial strength. Some other advantages found in the CNTs structure are that they can withstand extreme distorsions

without break. This deformation can be reversible [30],[31], a unic property only for nanotubes, inasmuch neither as graphite nor C$_{60}$ possesses reversible deformation modes reducing their volume.

Other studies have described the mechanical storage energy in carbon nanotubes (CNTs), reported by *F.A.Hill et al* [24], [32], [33] , estimating the magnitudes for the Young's modulus of two different types of CNTs which are: the Single-Walled Carbon Nanotubes (SWCNTs) and the Multi-Walled Carbon Nanotubes (MWCNTs). Both types have a Young's modulus of **1 TPa**. They have also an elastic strain equal to **6%**, demonstrated experimentally.

In this work, using a molecular dynamic model, a reversible tensile strain with value of 20% is demonstrated. This shows that the CNTs are highly flexible, and they can stand significant compression stresses, elongation, twisting and bending in reversible manners [34]. It was also reported the estimation of the elastic energy stored on a deformed body under a broad range of different loading conditions, the resultant volumetric energy density as a function of the tensile load on SWCNT and MWCNT using the mechanical model is shown on Figure 1-8.
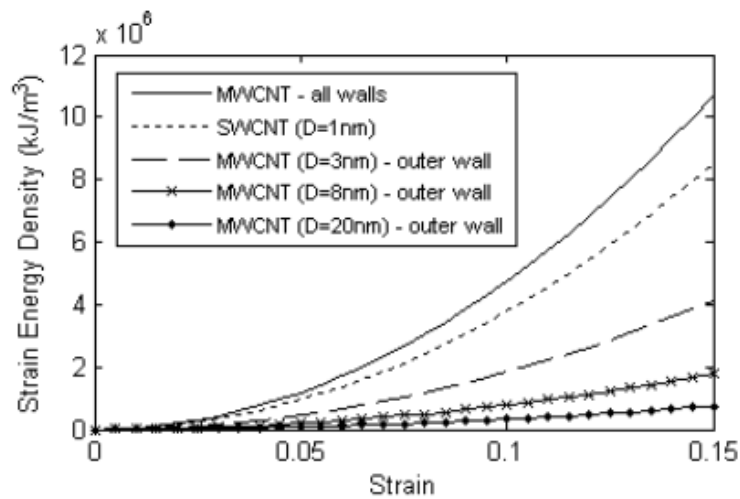
Figure 1-8: Volumetric energy density as a function of tensile strain for SWCNTs and MWCNT[24], [32], [33].

The results of the CNTs predictions made by the mechanical model shows a maximum energy density of CNT springs, loaded in tension and at the highest levels of strain, to be 7000 times greater than that of steel springs and eight times greater than the energy density of lithium-ion batteries. Practical considerations have to be taken into account, such as the need for a support structure or additional extraction hardware.

Subsequetnly to this main approach, experimental works were done on ultralong CNTs/TiO$_2$ reported by *Rufan Zhang et al* [35] where a maximum strain energy density values of *1125, 1085 and 970 Wh/kg*. These results showed good agreement with theoretical values where a value of **1163 Wh/kg was expected at a strain of 17%**.

1.2.3 Category 3:"Mechanical energy harvesting with Nanowire interfaces"

Piezoelectric Nanogenerators using Zinc Oxide nanowire arrays

As part of an alternative on mechanical energy harvesting systems, *Zhong Lin Wang et al* [36] present a conversion system of mechanical energy into electrical energy, at the nanoscale, through zinc oxide nanowire (NW) arrays. These aligned NWs are deflected with a conductive atomic force microscope tip in contact mode. The coupling of piezoelectric and semiconducting properties of zinc oxide creates a strain and, simultaneously, a charge separation across the NW, resulting in a mechanical bending. Due to a rectifying characteristic of the Schottky barrier appearings between the conductive tip and the NW, an electrical current is generated. The overall efficiency on the NWs-based piezoelectric power generator is estimated to be between 17 and 30%. This system enables the possibility of convert mechanical, vibrational, neumatic or hydraulic energy into electrical power to feed nanodevices of low consumption. The experimental design presented is shown in Figure 1-9.
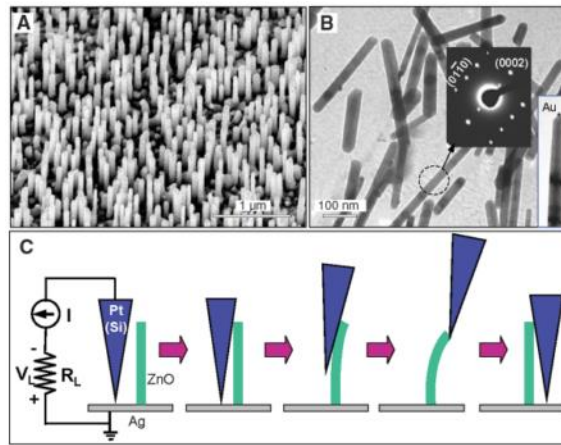
Figure 1-9: The experimental design for converting nanoscale mechanical energy into electrical energy, by vertical piezoelectric (PZ) ZnO NW's. (A) Scanning electron microscopy images of aligned ZnO NWs grown on a-Al2O3 substrate. (B) Transmission electron microscopy images of ZnO NWs, showing the typical structure of the NW's. The inset shows the electron diffraction pattern from a NW and, at the right hand side, shows a NW with an Au (seed). (C) Experimental setup and procedures for generating electricity by deforming a PZ NW with a conductive AFM tip. The base of the NW is grounded and an external load of R_L is applied, which is much larger than the resistance R_I of the NW. The AFM scans across the NW arrays in contact mode[36].

Another research on energy harvesting, done by *Guang Zhu et al*[37], consists in the fabrication of self-powered nanosystems, using the mechanical-electric energy conversion, that has been demonstrated through a piezoelectric cantilever working at its resonating mode [38]. A similar principle is used to the fabrication of High Output Nano Generators (HONGs), with the use of piezoelectric ZnO nanowires (NWs) grown vertically aligned on Si substrates synthesized using physical vapor deposition method. NWs have ~50 μm of length, ~200 nm of diameter, and grown direction along the c-axis direction. The HONGs fabrication process was done by the following steps:

1) <u>Transfer of the NWs to the substrate</u>: A small piece of Si substrate with grown ZnO NWs was mounted onto stage 1 and a piece of Kapton film with thickness of 125 µm was attached to stage 2. The Silicon substrate is placed down, and holds the vertical aligned ZnONWs. The stage 2 has a curved surface that holds the receiving substrate. Polydimethylsiloxane (PDMS) is used as a cushion layer to support the receiving substrate and keep the alignment of the ZnO NWs.

2) <u>Electrodes deposition</u>: in this step the electrodes are deposited in order to connect all the NWs together. The general dimensions of the ZnO NWs were of lengths ≈ 50 µm and diameters of 200 nm and growth direction along the c-axis.

After the assembling of theZnO NWs was completed, 600 rows of stripe-shaped Au electrodes with 10 µm spacing were obtained. This Au electrodes form a Schottky contact with the ZnO NWs that is the basic work principle of the HONG, there is an approximate density of about 3×10^5 NWs, in an effective working area of 1 cm2. Finally, in order to protect the general system, PDMS for is used to packaging the entire structure against invasive chemicals (see Figure 1-10).
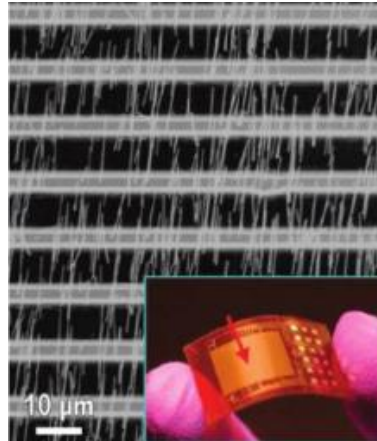
Figure 1-10: SEM image of ZnO NW arrays bonded by Au electrodes. Inset: demonstration of an as-fabricated HONG on its final packaging

The main principle of operation is based on the mechanical deformation of the ZnO NWs arrays, which are connected in parallel between each electrode to increase the output current, and in serie on each row to increase the output voltage. The final output voltage is generated due to they were oriented in the same sweep direction and their piezo electric potential was also aligned. To analyze the HONG's performance, a linear motor was used to periodically deform the HONG in a cyclic stretching-releasing agitation *(0.33 Hz)*.

The results from the characterization showed an output voltage of *2.03 V* and a current of *107 nA*. In comparison, the performance obtained has a peak output power density of *0.22 µW/cm2* for ZnO NWs with diameters of *200nm* which is 12 to 22 times a PZT based cantilever energy harvester.

Piezoelectric nanogenerators that harvest mechanical energy from environment

Following researchs done on the same field of nanogenerators (NGs), *Xudong Wang et al*[39] has presented a the design of self-sufficient power source that directly draws energy from ambient mechanical resources. As it was mentioned in the previous section, piezoelectric nanowires (NWs) are the building blocks of NGs. Therefore, in this work, the study of ZnO Nw as an ideal isolated piezoelectric and, secondly, with the contribution of a moderate doping with a more realistic point of view, were reported.

Nanowires are considered a one dimension (1D) nanomaterial that typically has diameters less than 100 nm and lengths larger than 1 μm. For the majority of ceramic NWs, they are found as single crystals which offer unique advantages in comparison with thin-film based piezoelectric cantilevers transducers, which are:

1. *They can enhance up to **400 or 500%** the piezoelectric effect when a strain gradient is presented in a ferroelectric NW with some tens of nanometers on thickness[40].*

2. *They have superior mechanical properties due to the lattice perfection on NWs. which enables much larger critical strain, higher flexibility and longer operational lifetime.*

3. *NWs have high sensitivy to small forces due to its large aspect ratio and small thickness, allowing them the creation of significant strains under forces of nano or pico Newtons.*

One of the main highlights of this work is the theoretical predictions for the estimation of the maximum piezoelectric potential that a **ZnONw** can reach. This theoretical model is based on the well known assumption that, when a NW is deflected, a piezoelectric potential can be generated on the side surfaces due to the crystal lattice distortion. For the case of the **ZnONWs,** the tensile surface trends to give a positive potential, while the compression side is polarized with a negative potential.

Two studies were done using the piezoelectric simulation model presented. The first study was done over a cylindrical ZnO Nw subjected to a punctual force f_y at the top face (see Figure 1-11 a). Firstly, considering an ideal perfect insulated piezoelectric material (see Figure 1-11 b) and, secondly, taking into account the contribution of defects on **ZnO** corresponding to an **n type** with a typical dopant concentration of 10^{17} **cm³** (see Figure 1-11c).
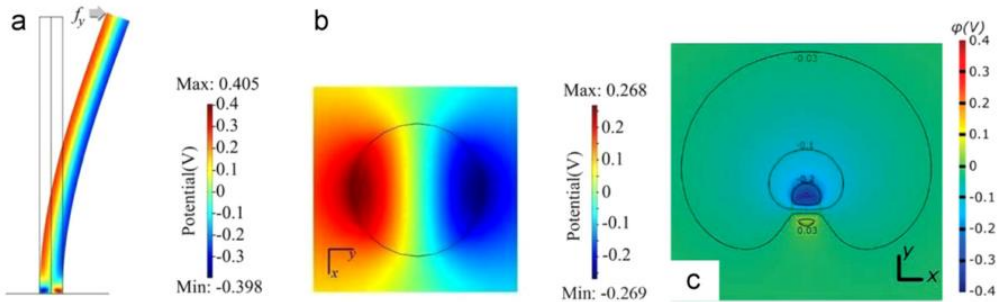
Figure 1-11: Potential distribution for a ZnO NW. (a) Side view of the potential profile. (b) Cross-sectional view of the piezoelectric potential. (c) Cross-sectional view of the piezoelectric potential when the contribution of free electrons is considered.

The results from the calculations, showed an electric field distribution on the NW cross-section, where the highest potential of **±0.27** was identified. The dimensions of the Nw were **50 nm** of diameter and **600 nm** of length, and is bent **145 nm** laterally at the tip by an 80 nN lateral force (see Figure 1-11 a). The comparison between the two studies showed that the maximum electrical potential for the positive side for the ideal piezoelectric case was of ≈ 0.3 V (Figure 1-11 b), larger than the case where the defects were considered, where the potential was less than **0.05 V**.

As it was reported **ZnONW** is the first nanomaterial that has been applied for NG development. Leading by the research on ZnO NWs, NWs were made from other piezoelectric materials, including BaTiO3, PZT, and PVDF.

1.2.4 Scope of research and methodology

With aim to develop a novel mechanical energy storage, on the mechanical domain, avoiding energy losses as it was described deeply on section 1.1.3, two main researchs described on section 1.1.2, will be used as back-bone conceptual approaches, to define our conceptual energy storage principle.

The first study in which is based this mechanical energy storage proposal is based on the analytical model described previously to store mechanical energy on the elastic deformation of CNTs, but instead of submit the material to tension and torsion, in our approach a compression will be used to transfer the mechanical energy to a **"spring-like"** material, storing this energy on the material's deformation, keeping it until the material is released from its deformed state, releasing the potential energy stored.

During the compression stage, the input force is related with the energy harvested available. Therefore, the necessary amount of this harvested energy is dependent on the mechanical properties of the **"spring-like"** material.

The mechanical energy storage system (**MESS)** will be charged and discharged for several cycles so, it is necessary that permanent deformations do not ocurr, or its degradation by deformation or fatigue have to be low enough, in order to ensure a long life of the **MESS**.

For the **"spring-like"** material selection, the next considerations ordered by priority need to be taken in to account:

1) *Elasticity:* the material has to be elastic, to withstand several deformations caused by duty cycle. It is preferent that can reach high strain levels, due to the fact that the amount of energy is related with the amount of strain.

2) *Scale*: initially the material is planned to be integrated on a micro energy harvester, then, a low volume and mass for the material, allows giving high energy density.

3) *Piezoelectricity:* eventhough initially the proposal is focused on store only mechanical energy, namely potential energy, that can be converted later in kinetic energy, for instance for using as an output force, is highly effective and versatile for the **MESS** to convert mechanical energy into electrical, as an intrinsic material's property.

When the mechanical properties needed for our **MESS** were analyzed, the second part of

the research (explained on section 1.2.3) was started, which consisted in the mechanical energy harvesting by using ZnO nanowires (*ZnONws*) in order to create High Output Nano Generators *HONGs*.

The main benefits of use ZnO nanowires as *"spring-like"* materials are listed below:

1) *Flexible and elastic:* it has been reported by *Chen C Q et al* [41] that *ZnONws* are highly flexible and elastics, showing that a pure single *ZnO* crystal of 100 nm diameter can be bent into the same arc as one micrometer diameter circle. *Xudong Wang et al* [39] demonstrate that *ZnONws* have superior mechanical properties, due to the lattice perfection, which enables larger critical strain, higher flexibility and longer operational lifetime.

2) *Scalability*: it was mentioned for the *HONGs* application that eventhough *ZnONws* keep a nano-scale, they can be arranged and deposited onto polymer substrates to increase scale and mechanical and electrical capabilities, depending on the application for they will be used.

3) *Piezoelectric and semiconductive materials:* as it was reviewed on 1.2.3 they are highly efficient for piezoelectric applications. They can enhance up to *400 or 500%* the piezoelectric effect when a strain gradient is presented in a *NW* with some tens of nanometers on thickness [40].

4) *Easy and low cost fabrication:* it has been reported by *M.Riaz et al* [42] that *ZnONws* can be fabricated by *Aqueous Chemical Growth* (*ACG*) or *Vapor Liquid Solid* (*VLS*) methods. Where *ACG* has an economic and easy method called *"Hydrothermal Method (HTM)"* reported by *Vayssieres et al* [43] which consists in a simple aqueous synthesis which produces *ZnO* nano structures through a thermal degradation of a *Zn* salt mixed with and organic compound, for instance Hexamine, this method will be explained deeply in the next chapter. These facts give us an extra benefit of using this kind of materials

The basic arquitecture of the MESS is showed in Figure 1-12.
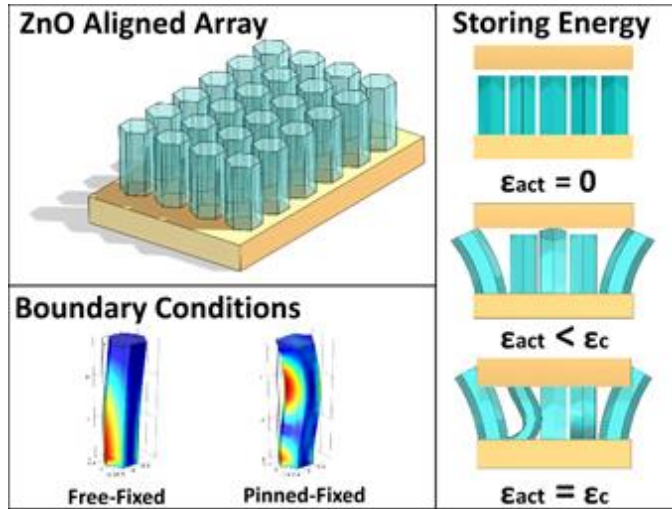
Figure 1-12: Mechanical Energy Storage System (MESS) conceptual design. Top left: ZnO Nws array, aligned perpendicularly, grown onto a substrate for using on a simple compression. Bottom left: the three main possible behaviors expected on the ZnONws during compression is shown, guided-fixed, free-fixed and Pinned-Fixed. Right: the energy storage process up to linear elastic buckling point.

1.2.5   Methodology proposed for design of MESS

<u>*Main objectives for MESS design*</u>

1) Improvement on Hydrothermal Method Synthesis growing more homogeneous morphologies of ZnONws and increase the growth density overall the substrate surface

2) Statistical analysis of dimensions and densities of growth overall substrate

3) Develope a mechanical model using the linear elastic theory supported by computing Finite Element Method (*FEM*) simulations, analyzing the preliminary limits of linear buckling and, also, its strain energy values that can withstand

4) Perform a mechanical characterization of the samples, comparing it with theoretical model, verifying experimental and realistic values for the Young's Modulus.

5) As an alternative of mechanical characterization, in order to emulate a large scale *MESS*, the fabrication and assembly of a Costumized Compression Set-up (*CCS*), will be used to characterize mechanically the *ZnOfws* and alternative materials.

Methodology to follow separated by phases of development

Phase 1 : Synthesis and optimization of HTM fabrication process for ZnONws

By using the previous background experience for the hydrothermal method synthesis of ZnONws, in this phase of the research, a new ZnO layer deposition technique will be used, in order to enhance the overall density of growth on the substrate surface. It will also be tested the contribution of the Au layer during the aqueous chemical growth, in order to explore the capabilities of the method for better results on morphology and dimensions.

Phase 2 : Statistical analysis of best results of ZnONws

By using a statistical dimensions method, based on SEM images treatment, the estimation of values for densities of growth, length and diameters will be performed. In order to obtain, a statistical footprint of the ZnO Nws dimensions, that will be used on Phase 3.

Phase 3 : Theoretical model and FEM simulations for mechanical behavior of a single ZnONw

By using the linear elastic theory with *ZnONws* statistical footprint, the analysis of a single *ZnONw* will be performed, in order to evaluate its capabilites to store strain energy using the linear buckling as a preliminar limit and, later on, studying its behaviour on postbuckling.

Phase 4 : Mechanical characterization for best samples of ZnONws

Once the theoretical model for a single *ZnONw* is completed, sacrificial tests will be done on the material, using a commercial nanoindentator, which will give us the experimental values needed for updating the theoretical model and, also, analyzing the viability to fabricate a *MESS* which stores mechanical energy in the *ZnONws* arrays.

Chapter 2. FABRICATION OF ZNO NANO/MICRO STRUCTURES

T his chapter is dedicated to describe the synthesis and optimization process, for the Zinc Oxide Nanowires (**ZnONWs**), which will be used as a **"spring-like"** material, for mechanical energy storage.

Firstly, a global view of the Zinc Oxide (**ZnO**) as a material is presented, focusing the literature review to see how the material can achieve different crystallization structures. Secondly, the main advantages of using the Hydrothermal Method (**HTM**) will be presented, showing its principal characteristics and preliminary results obtained on **ZnO** nanostructures.

Afterwards, after the **ZnONWs** morphologies were observed, a statistical study of dimensions on the **ZnO** nanostructures was done, in order to obtain the initial parameters for the theoretical model.

Finally, a discussion of which morphologies and which samples are the most optimal, for the arquitecture of the **MESS** proposal, is reported.

2.1. General properties of ZnO

In order to describe **ZnO** as our **"spring-like"** material, is necessary to give, firstly, an overview of its properties, focusing our attention on using this material to store mechanical energy. **ZnO** is located as part of the group II-VI binary compound semiconductors, it crystallizes in Rocksalt, Zinc blende or Hexagonal Wurtzite structures (see Figure 2-1) [44],[45].
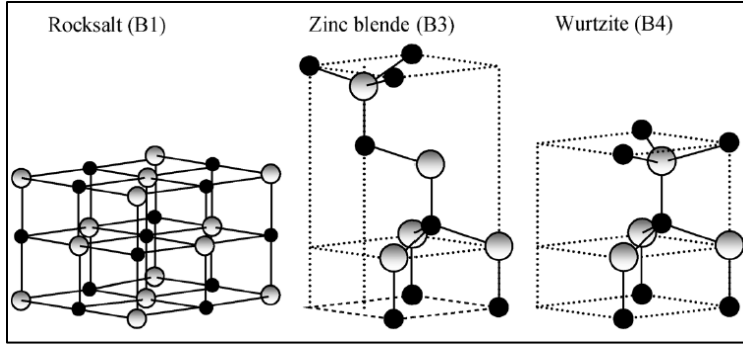
Figure 2-1: Representation of ZnO crystal structures, the gray and black spheres represent Zn and O[44].

From these crystal structures, the Rocksalt can be obtained using high pressures just as the Galium Nitride (**GaN**), the Zinc blende can be stable only by growing on cubic substrates and, finally, the Wurtzite **(Wz)** structure has a hexagonal unit cell, conformed by an anion that is surrounded by four cations, on each vertex of a tetrahedron.

An important fact to consider for **ZnO** is that, as part of other semiconductors from the group II-VI, **ZnO** can be transformed to the rocksalt structure at relatively modest external hydrostatic pressures. It is due to a decrease of the lattice dimensions caused by a Coulomb interaction, which favors the ionicity moreover the covalent nature that this can occurs. The transition of the **ZnO** undergoes a structural phase transformation, with a pressure of **10 GPa,** and it is completed at a pressure of **15 GPa**. In contrast, this transition was reported to be reversible at room temperature, with pressures ranges of **1.9±0.2 GPa**, where only wurtzite structures were observed by *Schmidt-Mende L* and *Chen D* [46], [47].

From the literature[48] we can have a clear approach of some of the mechanical properties of the ZnO, for each of its crystallization phases, this can be summarized in the Table 2-1.

Parameters	Wurtzite	Zinc blende	Rocksalt
C_{11} (GPa)	209.7^a, 206^b, 157^c, 190^d, 207^e, 209^f, 230^g, 231^h, 246^i	193^i	
C_{12} (GPa)	121.1^a, 117^b, 89^c, 110^d, 117.7^e, 85^f, 82^g, 111^h, 127^i	139^i	
C_{13} (GPa)	105.1^a, 118^b, 83^c, 90^d, 106.1^e, 95^f, 64^g, 104^h, 105^i		
C_{33} (GPa)	210.9^a, 211^b, 208^c, 196^d, 209.5^e, 270^f, 247^g, 183^h, 246^i		
C_{44} (GPa)	42.47^a, 44.3^b, 38^c, 39^d, 44.8^e, 46^f, 75^g, 72^h, 56^i	96^i	
C_{66} (GPa)	44.29^a, 44.6^b, 34^c, 40^d, 44.6^e, 62^f, 60^h, 115^i		
Bulk modulus, B (GPa)	142.4^j, 183^k, 170^j, 160^m, 162.3^n, 133.7^o, 156.8^k	161.7^n, 135.3^o, 154.4^k	202.5^j, 228^p, 205^m, 205.7^n, 172.7^o, 203.3^k
dB/dP	3.6^j, 4.0^p, 4.4^m, 4.05^n, 3.83^o, 3.6^k	3.95^n, 3.72^o, 3.6^k	3.54^j, 4.0^p, 4.88^m, 3.90^n, 3.77^o, 3.6^k
Young's modulus, E (GPa)	111.2 ± 4.7^q		
Hardness (GPa)	5.0 ± 0.1^q		
e_{31} (C m^{-2})	-0.62^r, -0.51^c, -0.39^s, -0.53^t, -0.51^u, -0.55^i, -0.66^v		
e_{33} (C m^{-2})	0.96^r, 1.22^c, 0.92^s, 1.19^t, 1.21^u, 1.19^i, 1.30^v		
e_{15} (C m^{-2})	-0.37^r, -0.45^c, -0.46^i		
e_{14} (C m^{-2})		0.69^j, 0.64^w	
Spontaneous polarization (C m^{-2})	-0.057^t, -0.047^x, -0.057^u		
Born effective charge, Z^*	2.06^t, 2.11^u, 2.10^w, 2.1^x		

[a]Ultrasonic measurement on single-crystal ZnO grown by chemical reaction in vapor state [86].
[b]Surface Brillouin scattering on polycrystalline ZnO film deposited by RF sputtering on (1 0 0) Si substrate [96].
[c]Acoustic investigation technique on ZnO film deposited by RF magnetron sputtering on sapphire substrate [97].
[d]Polarized Brillouin scattering on bulk ZnO single crystal [98].
[e]Ultrasonic resonance method on ZnO single crystal [99].
[f]Calculated by using LDA [14].
[g]Calculated by using GGA [14].
[h]Atomistic calculations based on an interatomic pair potential within the shell model approach [19].
[i]Calculated by using *ab initio* periodic LCAO method, based mainly on the Hartree–Fock Hamiltonian, with an all-electron Gaussian-type basis set [32].
[j]X-ray diffraction by using synchrotron radiation on polycrystalline ZnO (99.99% purity) [12].

Table 2-1 Mechanical properties of the ZnO obtained experimentally and by theoretical calculations. It can be observed that for the ZnO bulk, the Young's modulus is about of 111.2 GPa. For hexagonal crystals, only five independent stiffness constants remain: C11, C33, C12, C13,and C44. In piezoelectric crystals, electrical polarization is produced in the presence of stress, which is described by using the piezoelectric strain coefficients eijk, for hexagonal wurtzite only three independent components remain (e31, e33, and e15) [48].

Finally, as part of other properties of the *ZnO* we have to mention that since *ZnO* has an assimetric structure, and it is part of the tetrahedrally bonded semiconductors, it can have a high piezoelectric constant with electromechanical coupling, larger than in *GaN* and Aluminum Nitride (*AlN*). This property makes it a technologicaclly material for more applications, for example, it can be useful as a piezotransducer. However it has been also reported by *Hill and Wagmare et al* [48], [49] that piezoelectric ZnO constant is strongly sensitive to both temperature and stress, changing by about 20%(Hill) and 15–30% (Wagmare) respectively. These, dependences were primarily attributed to the changes in structural parameters, as manifested through the phonon and strain coupling (see Figure 2-2).
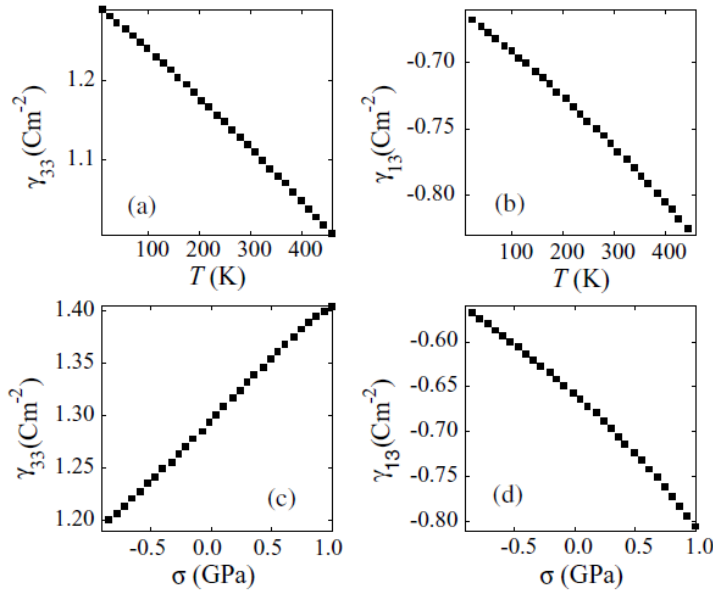
Figure 2-2: Dependence of the piezoelectric constants Y33 and Y13 of the ZnO submitted to temperature (a, b), and submitted to stress (c, d) [5].

For the **MESS** arquitecture, the best **ZnO** crystal structure for our proposal is the **Wz** structure, due to its **"hexagonal rod-like"** morphology, that could benefit the mechanism of compression by having a complete contact with the substrate and the compressor electrode. The second advantage of **Wz** is its piezoelectric and semiconductive properties, mentioned before.

As it was presented in Chapter 1, is desirable that the **NWs** are piezoelectric, to simplify the conversion from mechanical energy to electrical energy. In order to fulfill the fabrication process, in the next section, the experimental procedure followed to obtain the best **ZnO** structures will be described.

2.2. Fabrication of ZnO microstructures using the Hydrothermal Method

2.2.1. Description of Hydrothermal Method

It is well known that **ZnONWs** can be synthesized by several techniques, for instance: Chemical vapor transport and condensation (**CVTC**) with vapor liqud solid (**VLS**)[50], Laser synthesis[51],Methal Organic Chemical Vapor Deposition (**MOCVD**)[52], Anodization and high-vacuum die casting technique[53], Electron beam lithography[54],Layer by layer ZnO growth[55],Chemical Vapor Deposition[56],High-temperature vapor-phase process [57].

For the majority of the cases, these techniques are expensive and energy-consuming, therefore as an alterantive, **ZnONWs** can also be produced by solution-phase techniques.

They have been used because of their low growth temperatures (90-95 °C), and good potential for scaleup. One of the most common used, because of its simplicity and relatively low cost requirements, is the "Hydrothermal Method (**HTM)**"[47], [58]–[66], [43], [67], [68] and it has been selected for the **ZnONws** fabrication.

The hydrothermal process consists in the thermal degradation of Hexamine and Zinc Nitrate, by mixing the Zinc Nitrate Hexahydrate **(Zn(NO₃)₂ 6H₂O)** and Hexamine **(CH₂)₆N₄,** with equal concentrations and dissolved in deionized water.

To start the chemical reaction, the solution has to be heated, starting the thermal degradation, releasing the Zinc Ion (**Zn²⁺**) and the hydroxide (**OH⁻**) ions, for later produce **ZnO**. The general process is summarized in the following reactions:

$$(CH_2)6N_4 \ + \ 6H_2O \ \leftrightarrow \ 6HCHO \ + \ 4NH_3, \text{ (2-1)}$$

$$NH_3 \ + \ H_2O \ \leftrightarrow \ NH_4^+ + OH^-, \text{ (2-2)}$$

$$2OH^- \ + \ Zn^{2+} \ \rightarrow \ ZnO(s) \ + H_2O. \text{ (2-3)}$$
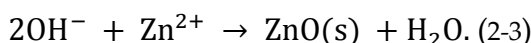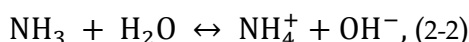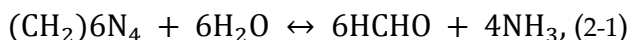
Some other solution phases techniques that are also used are listed below [69]:

A) Zinc Acetate Hydrate (**ZAH**) in alcoholic solutions with sodium hydroxide (**NaOH**) or tetra methyl ammonium hydroxide (**TMAH**)[70][71]
B) Template assisted growth[72]
C) Spray pyrolysis for growth of thin films[73]
D) Electrophoresis[74]

Several groups of morphologies that can be obtained due to the different combination of the compounds, are presented in the Table 2-2[75].

Additives	Particle properties	
	Morphology	Size (nm)
Tributylamine	Rod-like	200–300
Triethylamine	Rod-like	100–300
Triethanolamie	Spindle-like	100–300
Diisopropylamine	Rod-like	200–400
Ammonium phosphate	Rod-like	200–500
1, 6-Hexadianol	Rod-like	300–700
Triethyldiethylnol	Rod-like	100–300
Isopropylamine	Rod or sheet-like	
Cyclohexylamine	Sheet-like	300–500
n-Butylamine	Sheet-like	200–400
Ammonium chloride	Sheet	50–200
Hexamethylenetetramine	Snow-flake like	20–50
Ethylene glycol	Ellipse	40–100
Ethanolamine	Polyhedron	50–200

Table 2-2 Morphologies obtained using different compounds [75]*.*

The synthesis of different structures also depends on the variation of the parameters of the solution. Some of these parameters that have influence in the structure are:

A) **_pH level_** *during the chemical reaction on the hydrothermal bath*

B) **_Role of hexamine and concentration of compounds_** *during the growth process*

C) **_Growth temperature_** *during the hydrothermal process*

For the **pH Influence** on the hydrothermal growth, it has been reported [76] that **ZnONws** morphologies can vary according with the solution pH. These variations are presented on Table 2-3.

pH	Morphology		Shape
9.0	Coalescence of Zno	Coalescence	Budding flower
9.5	Nano-particles	↑	
10.0	Zno nanorod		Blossom
10.5	Separation sharp rods	Separation	Chestnut but or echinoid
11.0	Separation of thick rods	↓	Dense chestnut bur
11.5	Coalescence of rods		Gingko leaves
11.8	Archetype of thick rods	Coalescence	Dendelion

Table 2-3 Morphologies obtained depending on the pH level **[76].**

Another parameter of study is the use of the Hexamine (**HMTA)**, which is the source of the hydroxyl ions that helps the precipitation in the reaction. The contribution of the **HMTA** as a pH buffer has been reported in the literature[77], when is added it slows the release of OH⁻ ions, through thermal decomposition. It has been also demonstrated that the rate of decomposition of **HMTA** is independent of the reaction, moreover the **HMTA** acts as a kinetic buffer. As larger is the pH level, smaller is the **Zn** ions concentration and, therefore, Zinc Hydroxide **Zn(OH)$_2$** becomes unstable thermodynamically, and it will start to dissolve. Another demonstrated role of the **HMTA**, as a long chain polymer and a nonpolar chelating agent, is that it attaches preferentially to the non-polar facets of the zincite crystal, leaving the **Zn^{2+}** ions only in the polar (**001**) face, creating in consequence an epitaxial growth. Therefore, the **HMTA** acts also as a shape-inducer polymer surfactant more than a buffer [61], [78].

Other observations made on previous researches report were, that the concentration of the precursors in the chemical bath can also influence in a significant way the growth of the nanowires and also, the morphology [78]. It was reported the influence of the concentration of the precursors in the chemical bath for the **HTM**. Showing the evolution via epitaxial growth of the ZnO from seeds fixed on glass to lengths exceeding 5 microns (**μm)**, and 30 nanometers (**nm)** of diameter.

Finally for the **_effect of the temperature_** on the synthesis of nanowires, it was reported the obtention of different densities and morphologies, by controlling the growth temperature [30], [31].

2.2.2. Background on Hydrothermal Growth

From all these reviewed variation parameters to considered for the *HTM*, we have made our own conclusions, based on our experiments done with variations on initial pH level, growth temperature and concentration of compounds for the aqueous solution. The results and morphologies that we obtained, performing temperature and intial pH variations have been reported by *OG Suchil et al* [79].

For the next set of experiments described the general HTM process, followed the same steps: first the substrate was cleaned with ethanol and dried by Nitrogen, to eliminate any organic impurity. Then, in a second step the aqueous solution was prepared with an equimolar concentration, later the substrate was deposited in the acqueous chemical bath, finally the substrate with the *ZnO* nanorods was extracted and rinsed with deionized water, once it was cooled to room temperature. The general view of this process is shown on Figure 2-3.
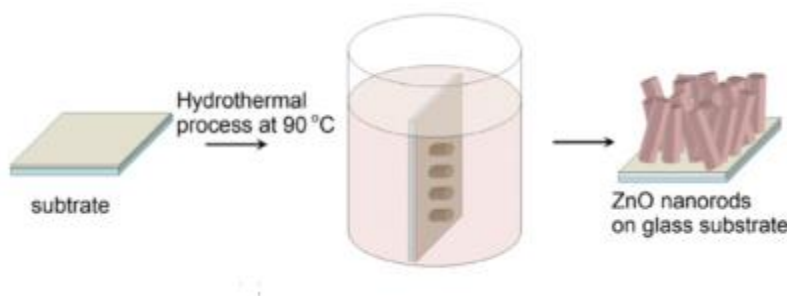
Figure 2-3: Hydrothermal process global view[80]

Our experiments were conducted following the *HTM* method separating growth samples in three different groups: for the first group, the temperature was varied using 50 °C, 70 °C and 90 °C while the heating time and the concentration of the solution were kept constant.

For the second group the pH level was varied, while the temperature (80ºC) and the heating time were kept constant. The solution had an initial pH level of 6.6, which was changed in order to obtain the levels for each test (5.7, 6.6, 7, 7.7, 11.7), by using Chloride Acid (*HCl*) and Sodium Hydroxide (*NaOH*). For the two group of experiments, an aqueous solution was used, by mixing *(Zn(NO₃)₂ 6H₂O)* as a source of Zn^{2+} ions, with *HMTA,* at a concentration for both compounds of 5 *mM*. The growth surface for each sample had 1 cm² on a substrate of 500 µm thick of Silicon (*Si)*, with 20 nm of Crome *(Cr)* and 100 nm of gold (*Au*), deposited on top by the electron beam deposition method. The main objective of these experiments was to see, if it exists, a relation by changing the initial pH level and growth temperature, which affects the *ZnONWs* morphologies. Results are shown on Figure 2-3 and Figure 2-4.

To summarize these experiments the general conditions of the hydrothermal method for the best results, are mentioned on Table 2-1.

Sample	Initial pH	Growth Temperature (°C)	Growth Time (h)	Compounds Concentration (mM)
TA	6	90	5	5
TB	6	70	5	5
TC	6	50	5	5
pHA	6.6	80	5	5
pHC	7.7	80	5	5
pHE	11.7	80	5	5

Table 2-4: Experimental conditions for our temperature and initial pH variation on HTM.
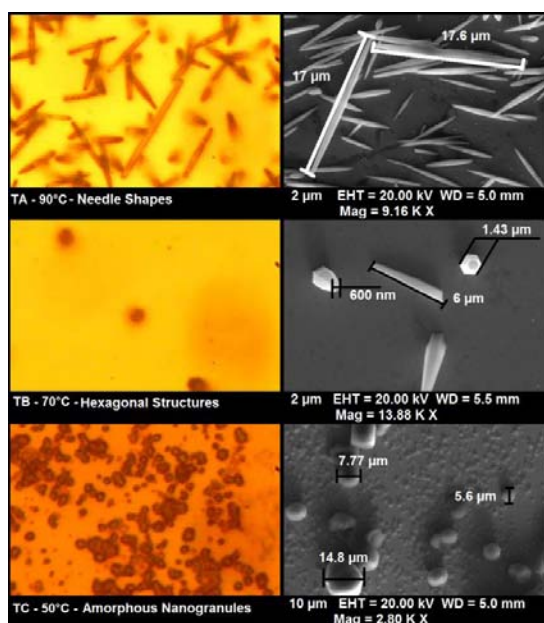
Figure 2-4: Results of temperature variation. At left column optical images done at 150x. At right column Scanning Electronic Microscope (SEM) images of morphologies [79]
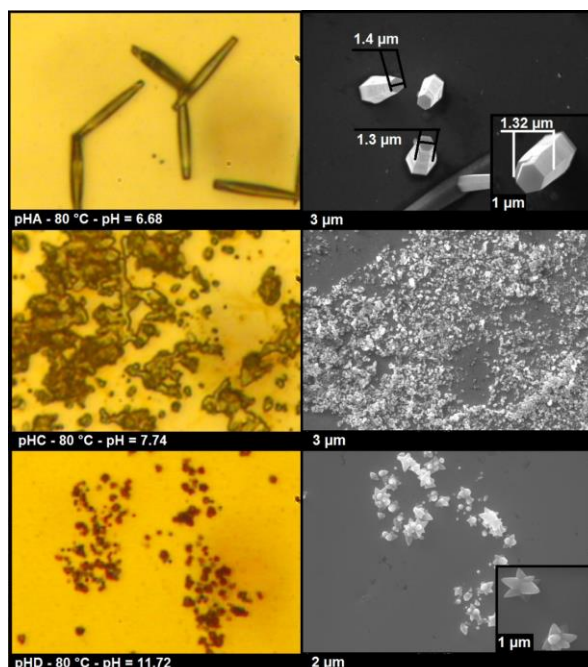
Figure 2-5: Results of pH variation. At left column optical images at 150 x. At right column SEM images of obtained morphologies. pHB sample was discarded in this image due to no growth results were found as pHC case [79]

In summary, from the temperature variation experiments, it was observed that nucleation[2] of **ZnO** structures starts from a temperature above 40 ºC (see **¡Error! No se encuentra el origen de la referencia.**-TC), but is not until 70ºC is reached, that "*hexagonal micro rod*" structures, with average diameters and lengths of 1.43 and 6 *µm* resepecively, were obtained (see **¡Error! No se encuentra el origen de la referencia.**-TB). Finally, at 90ºC "*needle-like*" structures, with diameters and lengths of 600 *nm* and 17 *µm* respectively, were obtained with a high number of structures per *µm*2 (density) overall the growth substrate (see **¡Error! No se encuentra el origen de la referencia.**-TA).

It seems that temperature influences **ZnO** morphologies and, simultaneously, the growth density over the substrate surface. Therefore, by these initial observations, the temperature was kept at 80°C for these experiments in which the pH level was varied, in order to verify if "*hexagonal micro rod*" structures (70ºC) or "*needle-like*" structures (90ºC) can be obtained.

From these experiments, it was observed that "*hexagonal micro rod*" structures were obtained with acid or nearly neutral pH levels (see **¡Error! No se encuentra el origen de la referencia.**-pHA). It was also observed that, for some cases, this "*hexagonal micro rod*" structures were formed with a larger diameter at the base than at the top face. This morphology has been reported by **S.Baruah et al**[61] and **Wang et al**[81], growing two-dimensional arrays of **"obelisk-shape ZnO nanorods"**, on quartz or glass substrate with

---

[2] Nucleation: is the first step in the formation of either a new thermodynamic phase or a new structure via self-assembly or self-organisation. Nucleation is typically defined to be the process that determines how long we have to wait before the new phase or self-organised structure appears.[144]

Zinc Nitrate, Ammonia and Ammonium Hydroxide as precursors, and explaining that the possible formation can be attributed to multiple layered structures. Moreover, with pH levels between 7 and 10, crystallization was not conclusive in a particular shape, on the contrary, it was more often found the formation of **"amorphous masses"** (see **¡Error! No se encuentra el origen de la referencia.**-pHC). Finally with a pH of about 11, particular **"flower shape-like"** morphologies were found, with out any presence of **"hexagonal micro rod"** shape (see **¡Error! No se encuentra el origen de la referencia.**-pHD).

Once it was observed from both groups of experiments, that an acid pH with a growth temperature between 80ºC and 90ºC can be beneficial for the obtention of hexagonal micro rods morphologies, a new challenge was presented: the perpendicular alignment and the homogeneous density of **ZnO hexagonal micro rods (ZnOHMRs)**, was a new issue of study to develop a well aligned **ZnONWs** array.

Therefore, from literature **Lukas Schmidth-Mende et al** [46], **Kuveshni Govender et al** [82]**, Vayssieres et al**[68] have reported a highly oriented and dense **ZnONWs** growth on Silicon (Si) substrates, by using a ZnO seed layer deposition, and using variation on the concentration of the compounds **((Zn(NO$_3$)$_2$6H$_2$O) and HMTA)**, from **25 mM** to **100 mM**.

Based on these assumptions, we perform a third group of experiments, with the objective of enhance the overall density and to obtain better alignment on structures. These experiments were conducted by varying the compounds concentration, during the hydrothermal process. The growth temperature and time were fixed at 90ºC and 2 hours of growing time, with an initial pH of 6. The concentration values used were 25, 50 and 100 mM for both compounds, over a Si substrate 500 μm thick, 20 nm of Cr and 100 nm of Au, deposited on top by the electron beam deposition method, with a growth surface of 1 cm^2. Results from these experiments are shown on Figure 2-6.
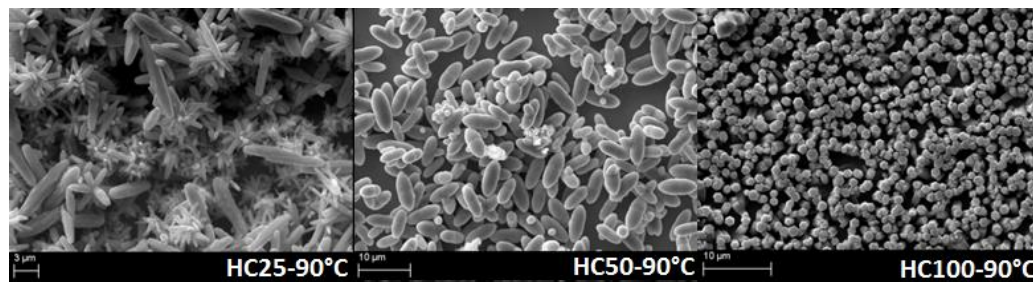
Figure 2-6: SEM images of concentration variation. At 25 mM (HC25) "flower-like"were formed. At 50 mM (HC50) structures with "egg-shape" appeared. At 100 mM (HC100) aligned "Hexagonal micro-rods" were obtained.

From the concentration experiments, it was always observed a high density of crystallizations over the substrate and, therefore, is inferable that concentrations above 25 mM have a bigger contribution for the density of crystallizations. A second observation is that the compounds concentration affects directly the morphology of the **ZnO** structures, modifying its shape from **"stars-like "**to **"hexagonal micro-rods"**.

Finally focusing on the _MESS_ proposal, the best structures in morphology, density and alligment were obtained at sample _HC100-90_.

Eventhough sample **HC100-90** showed the best results, it was clear that its density was concentrated just in three specific zones (see Figure 2-7-A). Rather than only some specific zones, it would be desirable found a high growth density overall substrate, to increase the compression area for the **MESS**.
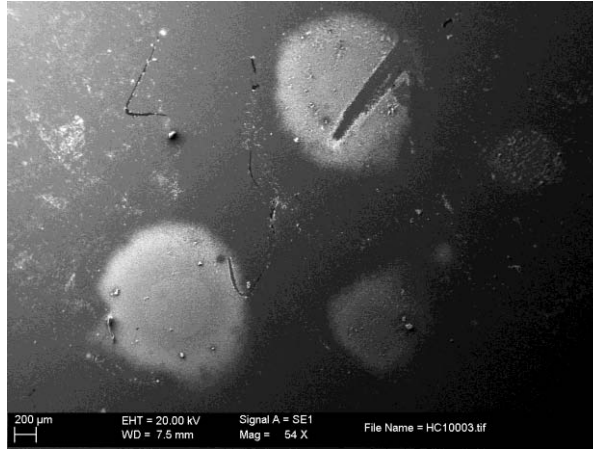
Figure 2-7: SEM images of HC100-90 sample showing 3 dense zones of chrystallizations.

With the aim to enhance the results from sample **HC100-90** in a homogeneous density, instead of specific zones, of well aligned **ZnO hexagonal micro-rods (ZnOHMRs)**, a new group of experiments was performed, using a well-known **ZnO** deposition layer method used by **Lori E. Greene et al** [83]**,** to fabricate **ZnONWs** arrays using textured **ZnO** seeds, this method and a group of related experiments are described deeply on the next section.

2.2.3. Optimization process of HTM with ZnO seed deposition

With the main objective to fabricate an array of well-aligned **ZnOHMRs** overall substrate surface, a group of experiments were conducted by using a **ZnO** seeds deposition method reported by **Lori E. Greene et al** [83][84]**.**

This method presents a high alignment growth of the **ZnONws,** by gas-phase or solution-phase fabrication, due to a pre-deposition process of **ZnO** nanocrystal seeds. It also demonstrates how this alignment is substrate-independent, showing that growth of **ZnONws** can be done on Silicon substrates, Indium thin oxide (**ITO)** glass, sapphire, titanium foil, and polymer surfaces like polydimethylsiloxane (**PDMS**) [84]. Finally, it was showed that vertical **ZnO** wires were grown from seeded substrates without gold film, which can be attractive from an economic point of view.

This **ZnO** seed layer deposition method is summarized by the following steps[83]:

1) The chosen substrate is cleaned with ethanol to clear from any organic residue

2) The source of the **ZnO** will be through the decomposition of Zn acetate $(Zn(O_2CCH_3)_2)$ *(98% Aldrich),* that has to be prepared in a solution of 5 **mM** dissolved in ethanol.

3) A droplet of this **Zn** acetate solution will be put it in the substrate, and then, it will be rinsed with clean ethanol for 10 s and dried with argon. This step has to be repeated from 3 to 5 times, in order to ensure a thin **Zn** acetate layer.

4) After the deposition of a fine layer of **Zn** acetate crystallites, the substrate is heat up to 350 ºC in air during 20 min. This final step is done for create an alignment of the ZnO seeds,as it has been reporte in the literature by *Greene et al*[83] . The entire process has to be repeated twice in order to ensure the correct deposition of the **ZnO** seeds.

After the **ZnO** seed layer deposition process is finished, either gas-phase or solution-phase can be chosen for fabricate the **ZnONWs** array. A comparison reported at the literature to see how the **ZnO** seed layer deposition process affects the alignment for hydrothermal and gas-phase growth is observed in figures (Figure 2-1, Figure 2-2).
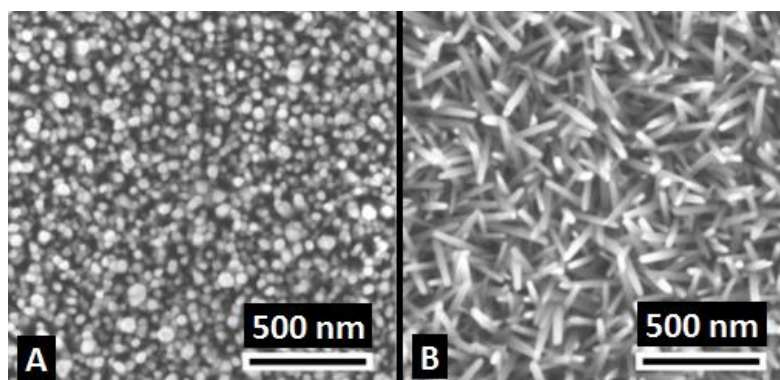
Figure 2-1 ZnO nanorod arrays grown on aqueous solution at 90ºC using HTM.(A) SEM Top-View of an array grown from ZnO nanocrystal seeds formed in Silicon surface through decomposition of Zn Acetate at 350ºC.(B) SEM Top-view of an array grown from preformed ZnO quantum dots on silicon by dip-coating [83]**.**
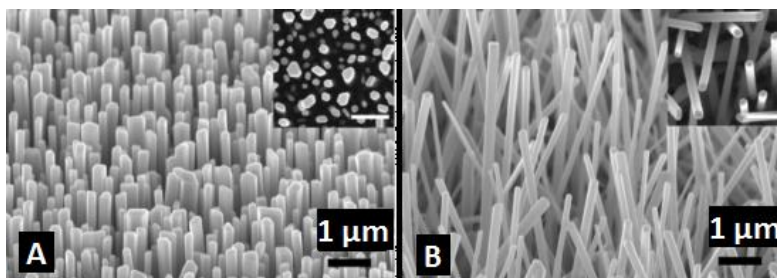
Figure 2-2 ZnO nanorod arrays grown by gas-phase on nonepitaxial substrates.(A) 45º Tilt SEM image of ZnONWs grown on a Silicon surface from acetate-derived seeds. Inset is a top-view image.(B) 45º Tilt SEM image of ZnONWs grown on same substrate without seeds and with gold as catalyst.Inset is a top-view image [83]**.**

Once the **ZnO** seed layer deposition method was observed to be beneficial for a high dense and well-alligned **ZnONWs** growth, we have adapted this method to our hydrothermal process. For our approach we decided to adapt the seed deposition compounds to our available compounds, namely instead of using **Zn** acetate we used a **ZnO** powder as our seeds crystal source. Since **ZnO** powder is insoluble in ethanol, we diluted it in 100 **ml** of deionized water, with the same concentration of 5 **mM** as in the original process. Seed deposition process was repeated 5 times, over a Silicion substrate without gold as catalyst. The annealing temperature was 350ºC during 20 minutes, the same as in the original method.

After the **ZnO** seeds deposition process, optical microscope observations were taken (see Figure 2-3). It was observed a low density addition of seed crystals on the substrate before annealing process (see Figure 2-3-A). After the annealing process, an increase in masses of crystals was observed (see Figure 2-3-B).
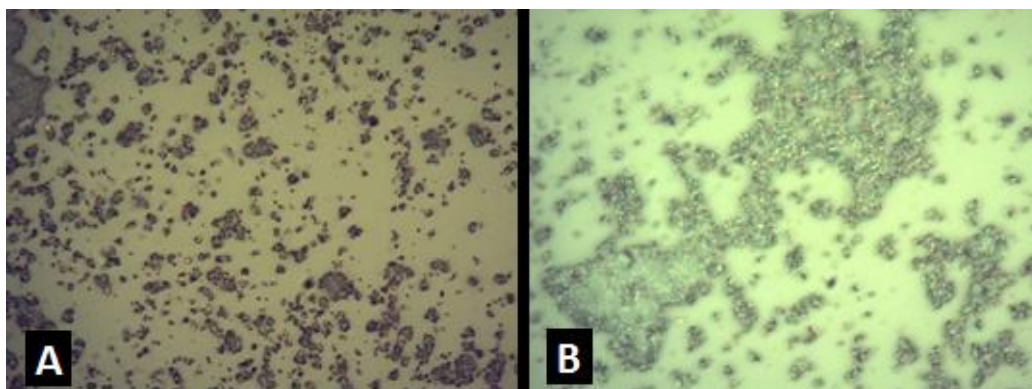
Figure 2-3 Optical images of ZnO seed layer deposition process at 150x.(A) ZnO seeds deposition before annealing process.(B) ZnO seeds deposition after annealing process.

After seeds deposition was finished, hydrothermal growth was done. The compounds used for hydrothermal process were the same as usual described in section 2.2.2. **((Zn(NO₃)₂ 6H₂O** and **HMTA** with an equimolar concentration of 75 **mM**. The growth temperature and time were 90ºC and 15 hours of growting time, in order to ensure enough nucleation time.

After hydrothermal process was carried out, the sample was rinsed with deionized water and cooled to room temperature for 30 minutes. Optical and SEM observations of results after hydrothermal process are observed in Figure 2-4 , Figure 2-5 and Figure 2-6.
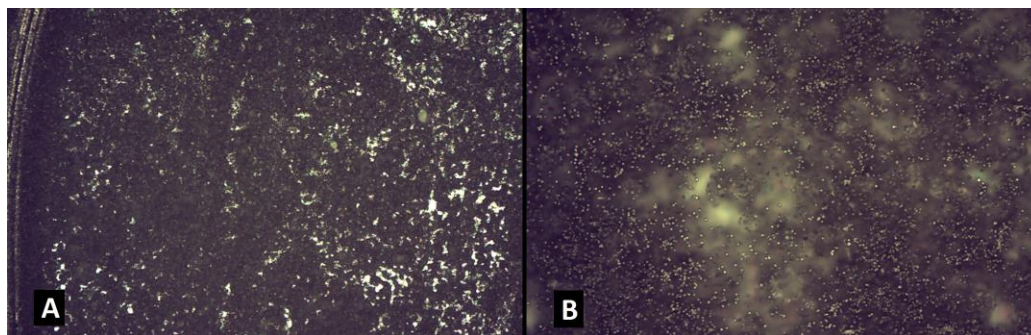
Figure 2-4 Optical images of ZnO seed deposition layer after hydrothermal process.(A) Plan-view of crystallizations formed at 10 x.(B) Plan-view of aligned ZnO rods observed at 150 x.
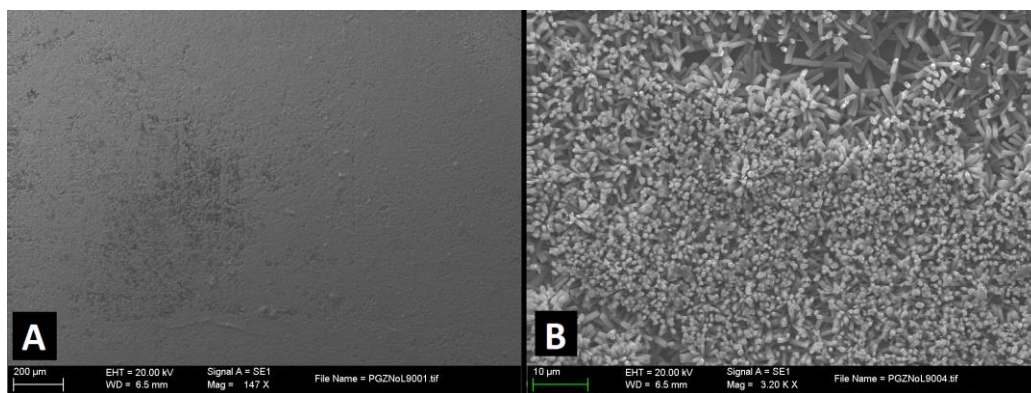
Figure 2-5 SEM images of ZnO seed deposition layer after hydrothermal process.(A) Top view of the ZnO crystallization growth at the substrate surface.(B) Top-view of ZnO micro rods grown aligned perpendicular to the Silicon substrate.

Figure 2-6 45º Tilt SEM image showing a high density ZnOHMRs grew overall surface.

It was observed from this preliminary experiment, that **ZnO** powder can crystallizes on the Silicon growth substrate, to later been used as pattern or seed layer. It was observed also that **ZnOHMRs** grew successfully over a Silicon substrate without using a gold surface as catalyst. Another observation was that **ZnO** seeds deposition is not easy to control and also there is no uniformity overall the substrate.

Nevertheless, through a high concentration on the hydrothermal compounds, over 75 **mM**, a dense and uniform crystallization overall the surface was achieved. On the other hand, in comparison with the original **ZnO** seed layer deposition method, it was observed that **ZnOHMRs** showed on Figure 2-5-B grew in two different levels, namely, in a first level, the formation of un-aligned **ZnOHMRs** were found lying on the substrate surface, and, over these formations, a growth of a second level of **ZnOHMRs,** aligned perpendicular with a smaller aspect ratio was found. It was not conclusive if this second level came from the seeds deposition or due to the high compounds concentration.

Therefore, following the same experimental methodology showed in section 2.2.2, the next experiments reported have, as main objective, to find the best conditions in which ZnO seeds deposition layer method with *HTM* can be optimal to achieve high quality **ZnONWs** aligned arrays. Experiments were separated in 5 different parameters which are: *HTM compounds concentration, Growth temperature, Number of annealings during ZnO seeds deposition and ZnO precursor for seeds deposition*.
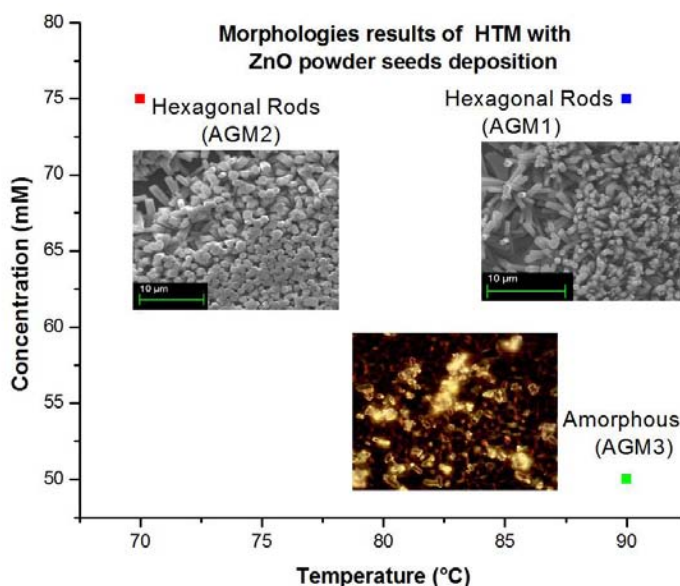
Figure 2-7 Results from concentration and temperature variation are shown. All experiments were done with a growth time of 15 hours and 2 ZnO seed depositions.

Experiments done using concentration results of 75*mM* and temperatures between 70°C and 90°C showed the same morphologies of *"hexagonal rods"* shape. On the other hand, at 50 *mM* not consistent morphologies were observed. Another aspect to consider is the importance of annealings after each *ZnO* seeds deposition process. To check the importance, an experiment was carried out withouth annealing process at growth temperature, time and concentration of 90°C, 15 hours and 75 mM (optimal) respectively, and no growth was observed. Therefore, annealings have to be always taken into account, for a successful growth with this adapted method.

With the objective of analyze deeply the *ZnO* seeds deposition method, a last group of experiments were performed, but using *Zn* acetate as seeds precursor, as it is mentioned in the literature [83][84]. Results from these experiments are shown on **¡Error! No se encuentra el origen de la referencia.**.
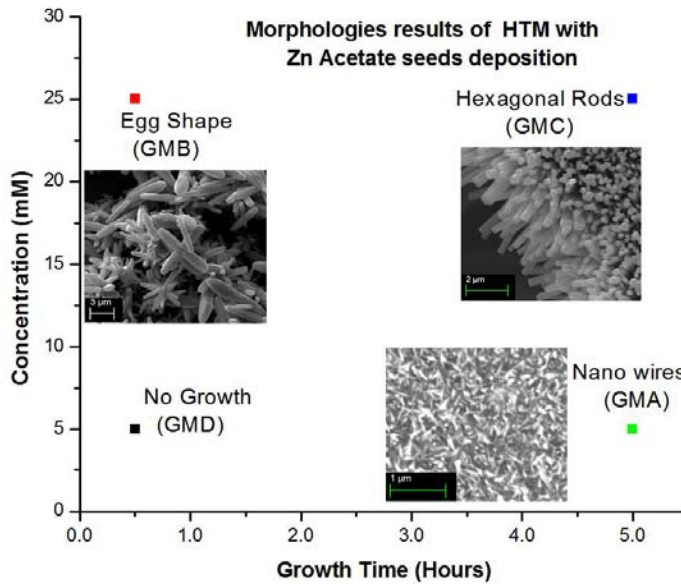
Figure 2-8: Results from concentration and growth time variation are shown. All experiments were carried out with a growth temperature of 90°C on Si/Au substrates.

In summary from experiments done with **ZnO** powder as seeds precursors it was observed that for crystallizations of **"Hexagonal rods"** is necessary to use a growth temperature between 70 and 90 °C, at least 2 annealings and a **HTM** compounds concentration above 50 **mM**. For the original method using **Zn** acetate as seeds precursor, the obtention of **"Nano wires"** or **"Hexagonal rods"**, can be done with a growth time of 15 hours, compounds concentration between 5 and 25 **mM** and a temperature of 90°C. In the next section, a selection of the best qualititative morphologies will be done, in order to analyze its statistical dimensions and densities.

2.2.4. Statistical analysis of dimensions and densities for ZnO microstructures

This section is dedicated to explain the statistical analysis carried out, in order to measure average diameters, lengths and densities through SEM images treatment. The main goal of this statistical analysis is to help on the selection for the best **ZnO** hexagonal rods or nanowires samples, which will be analyzed mechanically for subsequent chapters, and bring statistical information that will conduct the theoretical and experimental procedures.

The analysis starts by using top-view and 45° tilt SEM images taken from the selected sample. These images are treated with a commercial image processor program [85]. This program is used to create a grid that is superimposed over the original SEM image.

The grid is conformed by an array of cells, which have specific dimensions that match in scale with the original SEM image and, subsequently, each cell is treated separately, to measure individually every diameter and simultaneously, quantify the number of

hexagonal rods or nanowires found on the sample. For length measurements, SEM images with 45° tilt are used and no grid is required. The lengths are measured individually, taking into account the projection of 45° to avoid wrong measurements.

The result from this process is a hyper matrix conformed by values measured on each cell of diameters and densities. For lengths, a list is created instead of a matrix. Every cell is saved in a plane text file. These files are post-processed, to extract their corresponding values for average and standard deviation and of diameters, lengths and densities[86].

For a better understanding of this process, **HC100** sample with **ZnO finewires (fws)** described at section 2.2.2 is analyzed below. Analysis uses a SEM image at top-view with dimensions of [50 x 70] *µm,* according to original scale (see Figure 2-8), with grid cells of [10 x 10] *µm,* and 45° tilt SEM images for lengths measurements (see Figure 2-9).
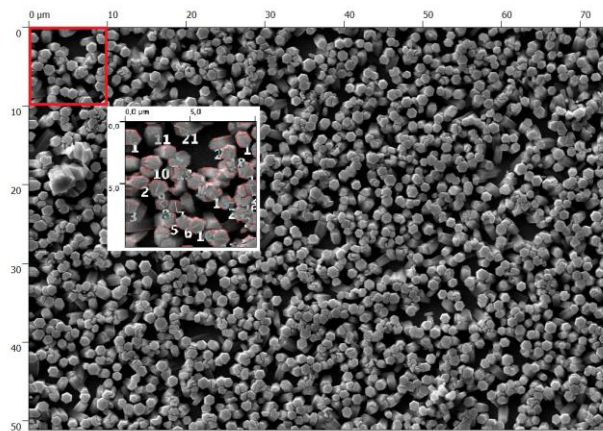
Figure 2-8 SEM Top view of sample HC100. Inset shows a treated cell (10x10) µm for diameters and densities measurement.
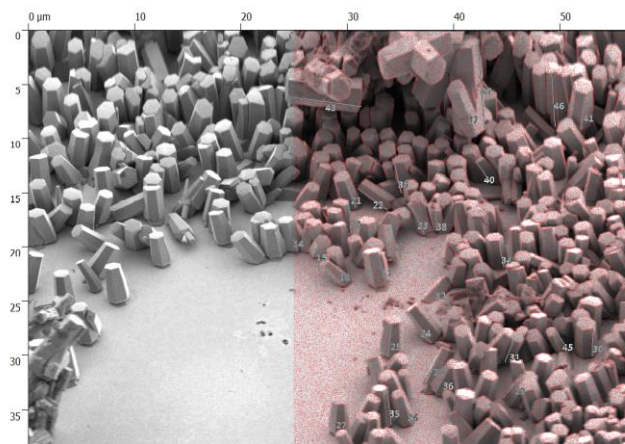
Figure 2-9 45º tilt SEM image of the sample HC100 is shown. At left half the original image without treatment. At right half in red shade a view of the image analyzed for length measurements.
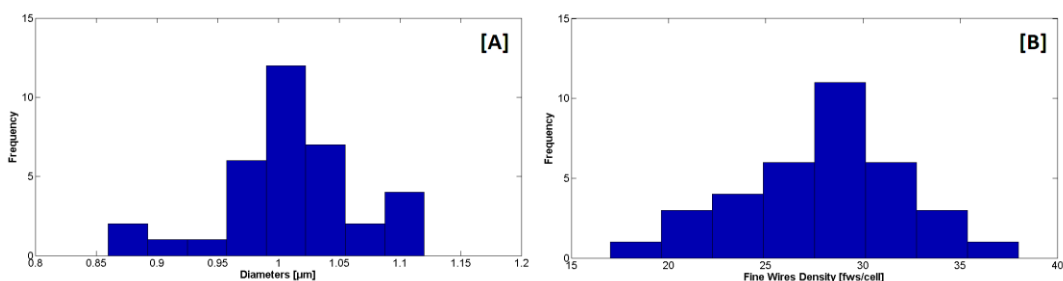
Figure 2-10 Results of statistical diameters and densities for sample HC100 are shown. (A) The histogram shows an average diameter of 1.05 ± 0.059 μm. (B) The histogram shows an average density of 0.28 ± 0.054 fws/ μm².
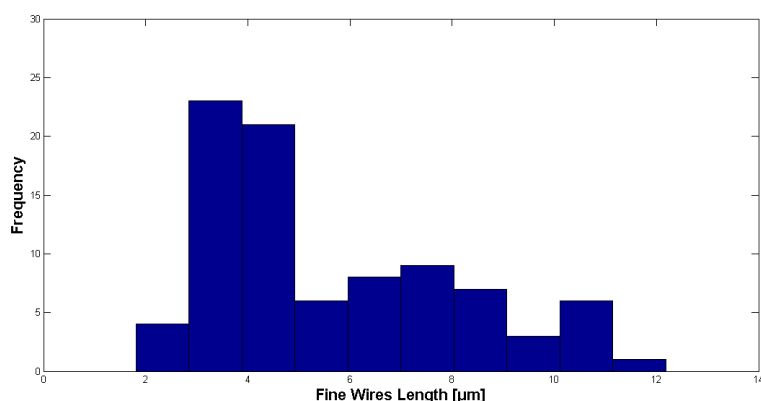
Figure 2-11 Results of statistical lengths for sample HC100 are shown. The histogram shows an average length of 5.7 ± 0.19 μm.

The statistical analysis was applied to all the samples that were observed with a high density of *ZnO* stuctures, with *"hexagonal rod"* or *"nanowire"* shape, which will be mention for convenience as *"finewires"* (*fws)*. Results are shown on Table 2-5.

Sample	Diameter (μm)	Length(μm)	Density(fws/ μm²)	ZnOfws Aspect Ratio (L/D)
HC100	1.05 ±0.059	5.7 ±0.19	0.28 ±0.054	5.43 ± 0.2
AGM1	0.63 ±0.19	1.67 ±0.92	0.68 ±0.43	2.65 ± 1.4
AGM2	1.11 ±0.32	3.73 ±1.38	0.38 ±0.14	3.36 ± 0.6
GMA	1.26 ±0.56	7.96 ±2.2	0.53 ±0.39	6.32 ± 2.6
GMC	0.213 ±0.067	2.01 ±0.59	4.18 ±1.1	9.44 ± 0.44

Table 2-5 Statistical results for finewires samples.

2.3. Summary

Through this chapter, the different fabrication techniques, for *ZnO NWs* have been reported. It was also discussed the main reasons for using the hydrothermal method instead of other techniques and, subsequently, a brief summary of previous experiments done with this technique is presented, describing an initial experimental methodology,in order to find the optimal conditions for growth.

Afterwards, this research was focused in report the addition of a well-known *ZnO* seeds deposition method, to optimize previous issues on crystallization during *HTM*, like low density and low alignment on *ZnO* structures.

Later, a new experimental methodology was followed, looking for the optimal conditions, on which *ZnO* structures grow aligned perpendicular to substrate, and with density almost homogeneous overall the growth surface.

It has to be mentioned that after SEM observations, for the majority of the cases, when the crystallizations formed *"hexagonal rod"* or *"wires"* shape, their size were more at micro scale than nano scale, and that is why, the term *"fine wires" (fws)* will be used from now on for convenience.

Finally, in order to extend the study for the *ZnOfws*, a statistical analysis was described as a tool to measure *ZnOfws* dimensions and densities. Results from this analysis were summarized in Table 2-5. The selection on these samples was based on morphologies closest to perpendicular structures, which can be used as our *"spring-like"* material for the *MESS.*

In the next chapter, the statistical values will be used as input parameters to solve the theoretical and simulation models. Once each case of *finewire* is evaluated, the initial parameters for an experimental procedure will be defined and the selection of the best samples can be discussed.

Chapter 3.   MECHANICAL ANALYSIS OF ZnO FINEWIRES SAMPLES

After the statistical dimensions and densities for the best *ZnO* finewires (*ZnOfws*) samples were approximated previously. In this chapter, a theoretical model for analyze the mechanical behavior of a single *ZnO* finewire is explained. Firstly, a conceptual approach of the loading process on the Mechanical Energy Storage System (*MESS*) is described, defining the possible behaviors of deformation of the *ZnOfws*. These behaviors will depend on the boundary conditions on which a single finewire is submitted. Secondly, a review from the literature focused on nanoindentation works applied to *ZnO* nanowires (*ZnONWs)* is analyzed. From this review, experimental Young's modulus values were extracted for use in combination with our *ZnOfws* statistical dimensions.

Once the basic parameters for the *ZnOfws* are set, the finewires are classified by dimensions, in order to apply the correct theoretical model for the extraction of the critical values and strain energy. Afterwards, through the use of Finite Element Model software (COMSOL Multiphysics), all computed values are assessed to verify agreement.

These simulations will be done in three different studies. The first study calculates the critical values through a linear buckling study. The second study is devoted, to extract the spring constant of a single finewire. Finally, a third simulation was done in order to analyze the Von Mises stresses, in order to calculate the theoretical limit for the linear elastic region on the **"*spring-like*"**material.

3.1. Description of working principle for the MESS proposal

Previously the general proposal of the *MESS* was described on section 1.2.2.A. In this section, the loading process will be explained deeply describing three main behaviors (*free-fixed, guided-fixed, pinned-fixed),* for the *ZnOfws* defined as our "*spring-like"* material.

In order to describe the loading process, *ZnOfws* have to be taken as common springs (see Figure 3-1-A). A common linear spring which follows the *Hooke's law* and is submitted to a simple compression (see Figure 3-1-B), storing a potential energy called *"spring energy"*. The potential energy stored for a body (*ZnOfws*), submitted to an elastic deformation is called *"strain energy"*[87], and it follows the expression (.

$$U = \frac{1}{2} \int_V \sum_i \sum_j \sigma_{ij}\, \varepsilon_{ij}\, dV \qquad (3.1)$$

Where V is the volume of the body, σ is the stress tensor and ε is the strain tensor. For the *ZnONWs* it has been reported by *M.Riaz et al* [88]**,** that a single *ZnO* nano wire can show an almost linear behavior, up to reach its first inflection point.

This behavior is independent of its fabrication method and, is highly dependent on its verticality over the growth surface. It has been also reported that after reach the first critical inflection point, as it can be the point where the wire buckles, *ZnONWs* become flexible, showing an increase on internal dislocations and, unstable deformations [89],[90].

A single *ZnO* finewire, taken as a single *"slender body"*(*its length is larger than its cross-sectional area*) and submitted to a load, can present a failure mode called *"buckling"*[91]. Buckling can be either elastic or inelastic, depending on the way the buckling stresses are, compared to the proportionality limit σ_p, which consists in the point where material do not maintain the linear proportionality between strees and strain, this behavior can appear within the elastic region of the material. For *"slender bodies"* or *"slender columns"*, buckling appears at stress levels below the proportionality limit. Therefore, this buckling is elastic and is called *"linear buckling"*.

On the other hand, when buckling appears beyond σ_p,material do not follows the Hooke's linear relationship, and stress-strain becomes non-linear[87].

Therefore, for our *MESS* proposal, the *linear buckling* point will be used as a preliminar limit for storing energy (seeFigure 3-1-C). It is spected to be an initial limit, before *ZnOfws* enter into an unstable behavior region (see Figure 3-1-D), which can compromises the reliability of the *MESS,* reducing storing energy cycles, due to permanent deformations, fracture or non-linear behaviors on *ZnOfws*.

To analyze the *linear* or *elastic buckling*, is necessary to establish the minimum compressive force or "*critical load"* (F_c), which is capable to produce buckling. Therefore, one method to solve this problem is through solving the diferential equation for a column subjected to an axial load (described on equation 3.2) [87].
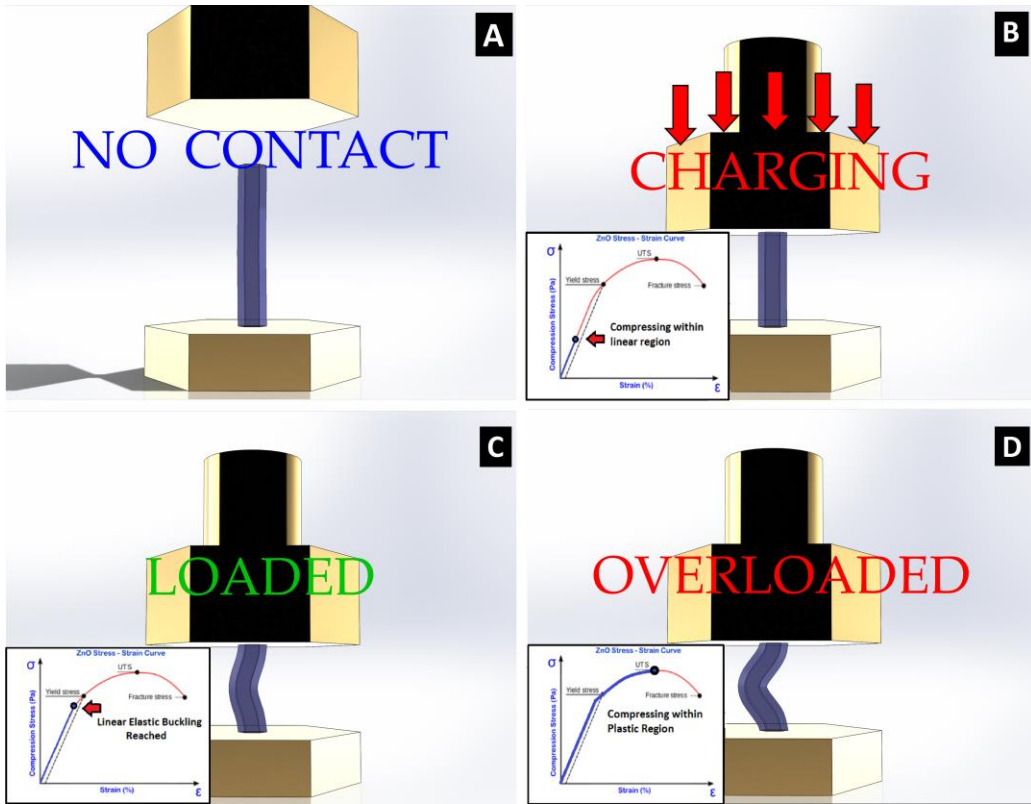
Figure 3-1: Loading phases for a single ZnOfw. (A) Unloaded. (B) Loading strain energy within linear elastic region. (C) Overloading ZnOfw beyond the linear buckling point.

From literature[87][92][93], is known that analysis can be done by using a pinned-pinned column as a generic example,which is buckled by a deflection of $u_y(x)$, provoked by applying an axial load F at the moving pinned end (see Figure 3-2).
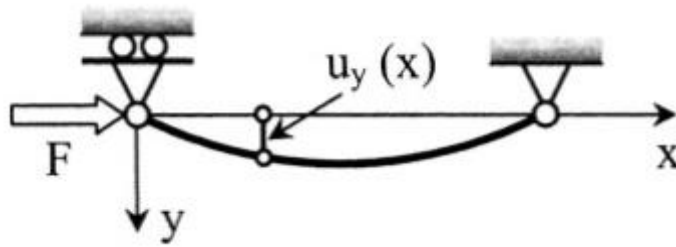
Figure 3-2: Pinned-pinned column in buckling.

The differential equation that governs this behavior is given by expression 3.2:

$$-M_z = EI_z \frac{d^2 u_y(x)}{dx^2}$$ (3.2)

Where E is the Young's Modulus and Iz is the moment of Inertia. The static moment M_z is given by equation.(3.3:

$$M_z = F\, u_y(x) \tag{3.3}$$

Substituing Eq.(3.3) on Eq. (3.2) gives the next equivalences:

$$\frac{d^2 u_y(x)}{dx^2} + k^2 u_y(x) = 0 \tag{3.4}$$

Where k^2 is equivalent to Eq.(3.5):

$$k^2 = F/EI_z \tag{3.5}$$

By solving Eq.(3.4) a generic expression for the force that produces buckling is given by Eq.(3.6):

$$F = \frac{n^2 \pi^2 EI_z}{l^2} \tag{3.6}$$

Where l is the length of the column, I_z is the inertia momentum and n is related with the interacting forces. For buckling $n=1$, because it involves the smallest force. Then, for all boundary conditions, besides the pinned-pinned mentioned, the *Euler*[94] equation for the linear buckling is given by Eq.(3.7):

$$F_c = \frac{\pi^2 EI_z}{leff^2} \tag{3.7}$$

Where F_c is the critical force, *leff* is the effective length and, is calculated through the effective length factor (*C*) by Eq.(3.8):

$$leff = C\, l \tag{3.8}$$

The effective length factor *C,* is dependent on the boundary conditions on which the column is involved. These boundary conditions are shown on Figure 3-3.
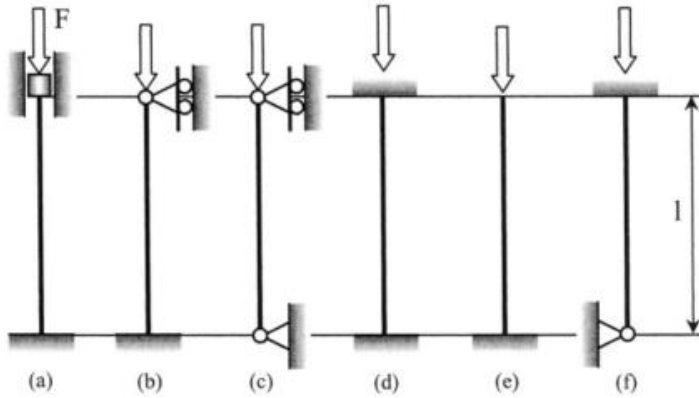
Figure 3-3: Combination of ideal boundary conditions on columns in buckling. (a) Guided-fixed (C=0.5), (b) Pinned-fixed (C=0.707), (c) Pinned-pinned (C=1), (d) fixed-fixed (C=1), (e) free-fixed (C=2) and (f) fixed-pinned (C=2) [87]*.*

Therefore, if a single *ZnOfw* is considered as a column submitted to compression, three boundary conditions can be selected, which are: *"free-fixed"*, *"guided-fixed"* and *"pinned-fixed"*. The reason for consider these behaviors, is given by the possible contact that may ocurr between the top substrate and the *ZnOfw* top face.

As it was mentioned before in section 1.2.2, the *MESS* proposal has an arquitecture conformed by a growth's substrate (*bottom*), a *"spring-like"* material (*ZnOfws array*) and, a second substrate (*top*) used for compress the *ZnOfws* (see Figure 3-4-1).

Therefore, during the *ZnOfws* compression, the top substrate makes contact with the top face of each *ZnOfw*. During this contact if there is no significant friction between them, a slippage may ocurr between contact faces (*Top substrate and ZnOfw*), giving the first boundary condition a *"free-fixed"* (see Figure 3-4-2A).

The second boundary condition, is given when it exists enough friction between contact faces, creating a temporary adhesion (*Top substrate-ZnOfw*) without separation during all the compression, giving the *"guided-fixed"* boundary condition (Figure 3-4-2B).

Finally, the third case is consider when the compression substrate, has a very rough surface or an enough sharpened surface (tip-shape), which makes contact with the *ZnOfw*, appling more a punctual force at the *ZnOfw* top face, instead of a distributed one. Therefore, the plausible behavior will be a *"pinned-fixed"* (see Figure 3-4-2C).
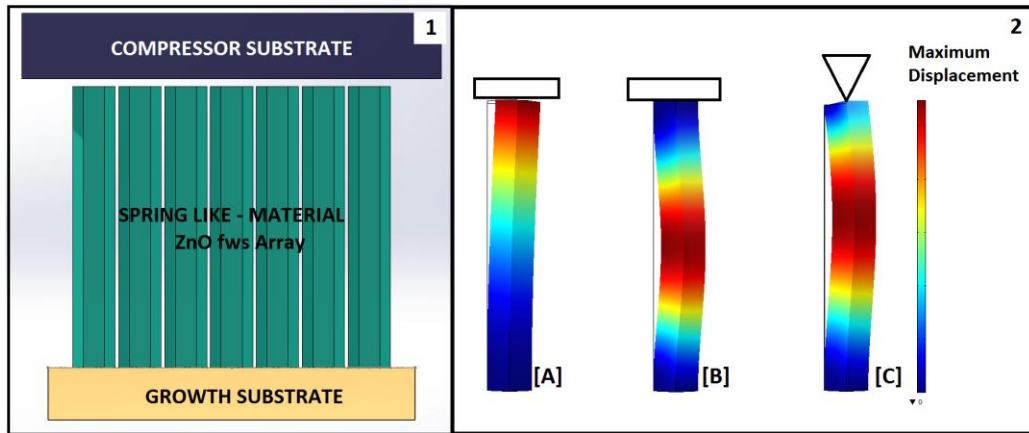
Figure 3-4: At left [1] the conceptual MESS with its basic compounds. At right [2] the ZnOFws boundary conditions [A] Free-fixed, [B] Guided-fixed and [C] Pinned-fixed at [2]. At extreme right, the color bar shows the ZnOfw's total displacement, been red the maximum and blue the minimum displacement using arbitrary units only for representation.

Another important parameter for the elastic buckling is the **"critical stress"**, at which buckling may occur, and is produced by the critical force (F_c), it can be calculated by Eq.(3.9:

$$\sigma_c = \frac{F_c}{A} = \frac{\pi^2 E I_z}{leff^2 A} \tag{3.9}$$

σc is the critical stress and A is the cross-section area of the column. The expression (3.9 can be rewritten in terms of critical strain ε_c as follow:

$$\sigma_c = E\varepsilon_c \tag{3.10}$$

Where ε_c is equivalent to Eq.3.11:

$$\varepsilon_c = (\pi^2 I)/(l_{eff}{}^2 A) \tag{3.11}$$

Therefore, the strain energy (**U**) from expression (can be rewritten as:

$$U = \frac{1}{2}\,\sigma_c \varepsilon_c V \tag{3.12}$$

where **V** is the volume of the column submitted to compression.

The relation between the critical stress and the column's slenderness ratio, is denoticed by the **radius of gyration**[3] that is expressed by equation 3.13:

$$r = \sqrt{I_z/A} \tag{3.13}$$

---

[3] **Radius of gyration:** it is the perpendicular distance from the axis of rotation to a point of mass, that gives an equivalent inertia to the original object [145].

And the *slenderness ratio*[4] can be defined by the expression (3.14:

$$\lambda = leff/r \tag{3.14}$$

Finally, the critical stress can be rewritten as expression 3.15:

$$\sigma_c = (\pi^2 E)/\lambda^2 \tag{3.15}$$

Once this relation is given, the σ_c critical stress can be plotted against the slenderness ratio λ (see Figure 3-5).
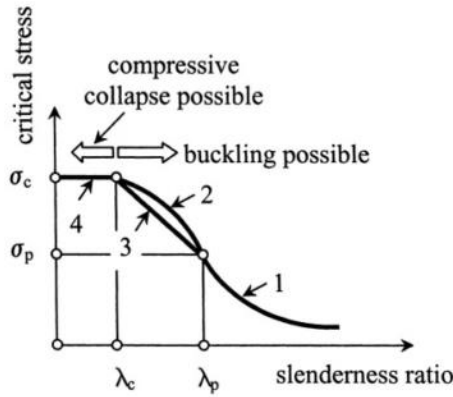
Figure 3-5: Critical stress vs. slenderness ratio. The slenderness ratio which occur at the propotional limit is represented by λp at a proportional limit of σp, the critical slenderness ratio on which columns instead of buckle may collapse is represented by λc at a critical stress of σc. Region 1 shows the region of an Euler's equation for large columns, for regions 2-4 inelastic buckling is expected and behavior may follow more accurate the Johnson's equation[87].

On Figure 3-5, the critical stress/slenderness ratio of Eq. (3.15) is represented. Then, the elastic buckling is only possible for values larger than the slenderness ratio at the proportionality limit of the material (λp), (see Figure 3-5 region 1) which corresponds to the material proportionality limit[5]. On the other hand for values smaller than λp, which apply to shorter columns defined by Eq. (3.14), columns might buckle inelastically (see Figure 3-5 regions 2 or 3).

Finally, for very short columns, buckling is not even possible, and columns may fail by collapse due to material failure[95] (see Figure 3-5 region 4). The curve 2 represents the *Engesser* model for inelastic buckling, which uses a similar expression that Eq. (3.15). The principal difference with this model is that Young's modulus is no longer constant, and is taken as either the tangent or secant value from the experimental stress- strain curve, or as an average combination of the two values. A different solution is given by *Tetmajer-*

---

[4] *Slenderness ratio:* is defined as the measure for prognostic if a column may failure by buckling, it relates the length, cross section area and the second moment of inertia of the column[95].

[5] *Proportionality limit:* it appears in the last value of stress, before stress/strain relation is no longer linear, and material do not follows Hooke's law. The stress-strain graph is a straight line up to this limit, and the slope defines the elastic modulus of the material.[146]

Jasinski model, which expresses a linear relationship between the critical stress/slenderness ratio.

In practice the Engesser model is used more for metallic components and the Tetmajer-Jasinski model is used instead for aluminum-type materials [87], [92].

For our particular case of study, it has been reported by *M.Riaz et al.*[88], [96]–[100] the use of the *J.B. Johnson's* model (explained on the next section), for characterize *ZnO Nanorods (ZnONRs)* that do not behave as long columns which follow *Euler* model.

This section has reported the bases of the linear elastic theory applied to columns that reach a linear buckling point. Then, by considering the *ZnOfws* as columns, it was described the three main boundary conditions that will govern their mechanical behavior on the *MESS.*

In the next section, the application of the linear elastic theory on *ZnONWs* will be reported. Therefore, a review on previous works done on mechanical characterization will be mentioned and summarized. Finally, the same analysis will be applied to the *ZnOfws* samples obtained and reported on Chapter 2.

3.2. Background of linear elastic theory applied to ZnO NWs

Previous works done on mechanical characterization for *ZnONWs* and *ZnONRs* reported by *M.Riaz et al* [88], [96]–[100], have explained the use of two models for approach the experimental results of nanoindentation tests. The first one is the *Euler's model* which has been described at previous section, is used more for *ZnONWs* and *ZnONRs* which have a value of *slenderness ratio* larger than the proportianilty limit and may failure by buckling. For the second model is used the *J.B.Johnson's model,* it consists in an extension of the *Euler* model fitting a parabola to the *Euler* stress/slenderness ratio curve [98](see Figure 3-6).
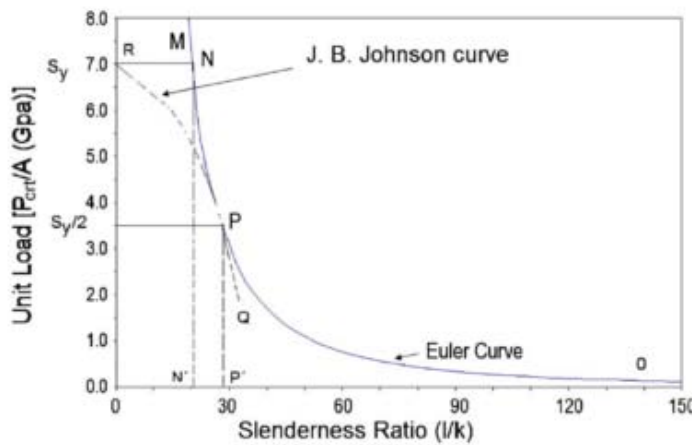
Figure 3-6: Euler and J.B.Johnson's curves for stress/slenderness ratio[98]*.*

The *J.B.Johnson's* model is valid for values of slenderness ratio between points P and R observed at Figure 3-6. At point *P* is located the *critical slenderness ratio* of the material λ_c , it is defined by Eq.3.16:

$$\lambda_c = \sqrt{(2\pi^2 CE)/S_y} \qquad\qquad (3.16)$$

Where S_y is the yield strength of the material, moreover for columns with slenderness ratio λ smaller than λ_c, the column is considered short and, **J.B.Johnson's** model have to be applied, is defined with Eq.3.17:

$$\sigma_c = S_y - \frac{1}{CE}\left(\frac{S_y}{2\pi}\frac{l}{r}\right)^2 \qquad\qquad (3.17)$$

Once this analysis was reported, **Euler** and **Johnson's** model were used by **M.Riaz et al** [2], to clasify the experimental results from several nanoindentation tests, performed on **ZnONWs** and **ZnONRs** arrays grown by two different techniques, **Aqueous Chemical Growth (ACG)** by Hydrothermal Method and a **Vapor Liquid Solid** mixing **ZnO** and **Graphite** powder. Both group of experiments used as growth substrates, **Silicon Carbide (SiC)** and **Silicion (Si)**.

To summarize the experiments done by **M.Riaz et al**, Table 3-1 shows the analysis results only for the **ACG ZnONWs** grown on **Silicon**, due to similiarity in synthesis and substrate material for our **ZnOfws** samples.

End condition of nanorods	C	$(l/k)_{p'}$	$(l/k)_{\text{actual}'}$	Strain energy $\times 10^{-15}$ (J)	Experimental critical stress σ_c (MPa)	Modulus of elasticity E (GPa)	Critical strain ε_c (%)	Analysis model
Fixed-free	0.25	9.93	13.43	0.025	221.3	16.2	0.013 66	Euler
Pinned-pinned	1.00	20.0	13.43	1.23	221.3	33.0	0.67	J.B. Johnson
Fixed-pinned	2.00	28.1	13.43	2.45	221.3	16.5	1.34	J.B. Johnson
Fixed-fixed	4.00	40.0	13.43	4.90	221.3	8.25	2.68	J.B. Johnson

Table 3-1: Slenderness ratio, critical stress, strain and strain energy for buckling on ZnONws grown by ACG on Si substrate. Their diameters, lengths and denisities of growth were 85.5±22 287±23 nm and 90 ZnONws contacted during nanoindentation. For ZnO modulus of elasticity, E=140.0 GPa and Yield strength Sy=7.0 GPa.

After this brief overview of previous work done to characterize **ZnONWs**, the next section will describe the methodology followed for the analysis of our **ZnOfws** samples**.**

3.3. Methodology to apply the linear elastic theory on the ZnOfws samples

The mechanical analysis followed for our **ZnOfws** samples can be summarized in the next steps: Classification of **ZnOfws** samples by **slenderness ratio,** application of Euler and Johnson's model to **ZnOfw** samples and a brief discussion of results.

3.3.1. Classification of ZnOfws samples by slenderness ratio

As a result from the statistical analysis done for the *ZnOfws* samples mentioned in Chapter 2 next table was obtained:

Sample	Diameter (μm)	Length(μm)	Density (fws/ μm²)	ZnOfws Aspect Ratio (L/D)
HC100	1.05 ± 0.059	5.7 ± 0.19	0.28 ± 0.054	5.43 ± 0.2
AGM1	0.63 ± 0.19	1.67 ± 0.92	0.68 ± 0.43	2.65 ± 1.4
AGM2	1.11 ± 0.32	3.73 ± 1.38	0.38 ± 0.14	3.36 ± 0.6
GMA	1.26 ± 0.56	7.96 ± 2.2	0.53 ± 0.39	6.32 ± 2.6
GMC	0.213 ± 0.067	2.01 ± 0.59	4.18 ± 1.1	9.44 ± 0.44

Table 3-2: Statistical results for ZnO finewires samples obtained from HTM process.

Firstly, the dimensions defined on Table 3-2, and two different geometries for the top-face of the *ZnOfw*, hexagonal and a circular cross section, will be considered. The reason is based in make the comparative with the FEM simulated results, and choose the geometry that gives the best agreement with the smaller error. To accomplish both studies of geometry, the expressions 3.18 to 3.21 have to be considered for the inertia momentum *I* on the *ZnOfws* samples.

For a circular cross-section area:

$$I = \frac{\pi r^4}{4} \tag{3.18}$$

With an area defined by:

$$A = \pi r^2 \tag{3.19}$$

For a hexagonal cross-section area:

$$I = \frac{5\sqrt{3}\, s^4}{16} \tag{3.20}$$

Where *s* is one side of the hexagonal face, with an area defined by:

$$A = \frac{3\sqrt{3}}{2} s^2 \tag{3.21}$$

By taking expressions (3.14 and (3.16, the slenderness ratio λ and the critical slenderness ratio $λ_c$ can be calculated for each sample and geometry. It is necessary to consider the values of Young's modulus for *ZnO* bulk. Following the same analysis as in previous works[88], [96]–[100], from Table 3-1, a bulk Young's Modulus *E=140 GPa* for *ZnO* and a yield strength *Sy=7 GPa*[41] were taken. The results from this first approach are shown on tables Table 3-3 and Table 3-4.

Circular Cross-section		Boundary Condition	Slenderness Ratio (λ)	Critical Slenderness Ratio (λc)	Model
HC100 (L/D) = 5.43 ± 0.2	Free-Fixed	2	43.43 ± 1.9	28.10	Euler
	Guided-Fixed	0.5	10.86 ± 0.5	14.05	Johnson
	Pinned-Fixed	0.707	15.35 ± 0.7	16.71	Johnson
AGM1 (L/D) = 2.65 ± 1.4	Free-Fixed	2	21.21 ± 11.6	28.10	Johnson
	Guided-Fixed	0.5	5.30 ± 2.9	14.05	Johnson
	Pinned-Fixed	0.707	7.50 ± 4.1	16.71	Johnson
AGM2 (L/D) = 3.36 ± 0.6	Free-Fixed	2	26.88 ± 4.7	28.10	Johnson
	Guided-Fixed	0.5	6.72 ± 1.2	14.05	Johnson
	Pinned-Fixed	0.707	9.50 ± 1.6	16.71	Johnson
GMA (L/D) = 6.32 ± 2.6	Free-Fixed	2	50.54 ± 21.1	28.10	Euler
	Guided-Fixed	0.5	12.63 ± 5.2	14.05	Johnson
	Pinned-Fixed	0.707	17.87 ± 7.4	16.71	Euler
GMC (L/D) = 9.44 ± 0.44	Free-Fixed	2	75.49 ± 3.5	28.10	Euler
	Guided-Fixed	0.5	18.87 ± 0.8	14.05	Euler
	Pinned-Fixed	0.707	26.69 ± 1.2	16.71	Euler

Table 3-3: Results of slenderness ratios (λ) and critical slenderness ratios (λc) calculations for ZnOfws samples, using a circular cross-section area.

Hexagonal cross-section		Boundary Condition	Slenderness Ratio(λ)	Critical Slenderness Ratio (λc)	Model
HC100 (L/D) = 5.43 ± 0.2	Free-Fixed	2	47.57 ± 2.1	28.10	Euler
	Guided-Fixed	0.5	11.89 ± 0.5	14.05	Johnson
	Pinned-Fixed	0.707	16.82 ± 0.7	16.71	Euler
AGM1 (L/D) = 2.65 ± 1.4	Free-Fixed	2	23.23 ± 12.7	28.10	Johnson
	Guided-Fixed	0.5	5.81 ± 3.1	14.05	Johnson
	Pinned-Fixed	0.707	8.21 ± 4.5	16.71	Johnson
AGM2 (L/D) = 3.36 ± 0.6	Free-Fixed	2	29.45 ± 5.2	28.10	Euler
	Guided-Fixed	0.5	7.36 ± 1.3	14.05	Johnson
	Pinned-Fixed	0.707	10.41 ± 1.8	16.71	Johnson
GMA (L/D) = 6.32 ± 2.6	Free-Fixed	2	55.36 ± 23.1	28.10	Euler
	Guided-Fixed	0.5	13.84 ± 5.8	14.05	Johnson
	Pinned-Fixed	0.707	19.57 ± 8.2	16.71	Euler
GMC (L/D) = 9.44 ± 0.44	Free-Fixed	2	82.70 ± 3.8	28.10	Euler
	Guided-Fixed	0.5	20.67 ± 0.9	14.05	Euler
	Pinned-Fixed	0.707	29.23 ± 1.3	16.71	Euler

Table 3-4: Results of slenderness ratios (λ) and critical slenderness ratios (λc) calculations for ZnOfws samples, using a hexagonal cross-section area.

This first classification observed on Table 3-3 and Table 3-4 prove that the variation of the intertia momentum *I* and the cross-section area *A,* affects with low significance the results. Nevertheless, it was found, for samples HC100 and AGM2, new cases Euler for the hexagonal cross-sectioncalculations that do not appear for the circular cross-section, for the boundary conditions *pinned-fixed* and *free-fixed*. On the other hand it was found that the *ZnOfws's* aspect ratio has more influence on the classification, showing a trend where as larger is the aspect ratio the more probable to buckle, and therefore, the Euler's model can be applied. For instance, samples AGM1 and AGM2, which are the smallest aspect ratios in comparison to the others, showed predominance for the Johson's model. This relation has been summarized only for the circular cross-section on Table 3-5.

Sample	ZnOfws Aspect Ratio (L/D)	Euler's Model Cases	Johnson's Model Cases
HC100	5.43 ± 0.2	1	2
AGM1	2.65 ± 1.4	0	3
AGM2	3.36 ± 0.6	0	3
GMA	6.32 ± 2.6	3	0
GMC	9.44 ± 0.44	3	0

Table 3-5: Results of ZnOfws classification considering a circular cross-section. It can be noticed that large aspect ratios follow more the Euler model, and therefore is more probable to buckle.

Once the classification has been reported, in the next section the application of the linear elastic theory will be done, with the purpose of extract the critical values for our ZnOfws samples.

3.3.2. Application of Euler and Johnson's model to ZnOfws samples

Once the *ZnOfws* samples have been classified by buckling model, in this section the critical force, critical stress, critical strain and strain energy were calculated using equations (3.9, (3.10 and (3.12.

As in previous section values of bulk Young's modulus *E=140 GPa* [41]*,* yield strength *Sy= 7 GPa* [101] for the *ZnO*, and the corresponding experimental Young's modulus for the *ZnOfw (E exp)* depending on the boundary condition were extracted fromTable 3-1. These values were approached from nanoindentation experiments done and reported by *M.Riaz*[42], [96], [98], [99]. As it was seen on the classification section, geometry will be varied by two different models, to verifiy the contribution of the volume for the strain energy calculation.

Therefore, a cylindrical and a hexagonal prism body were considered for every *ZnOfw* sample. The results from these calculations are shown in Table 3-6 and Table 3-7.

Cylindrical Volume		Boundary Condition	E exp (GPa)	Crt Strain (%)	Crt Stress (MPa)	Crt Force (μN)	U (pJ)	Model
HC100	Free-Fixed	2	16.2	0.52	84.77	73.40	1.09	Euler
	Guided-Fixed	0.5	8.25	8.37	690.7	598.1	142	Johnson
	Pinned-Fixed	0.707	16.5	4.18	690.90	598.30	71.40	Johnson
AGM1	Free-Fixed	2	16.2	2.19	355.54	110.83	2.03	Johnson
	Guided-Fixed	0.5	8.25	35.11	2897.00	903.06	264.78	Johnson
	Pinned-Fixed	0.707	16.5	17.56	2897.00	903.33	132.47	Johnson
AGM2	Free-Fixed	2	16.2	1.36	221.24	214.09	5.45	Johnson
	Guided-Fixed	0.5	8.25	21.85	1802.70	1744.00	710.90	Johnson
	Pinned-Fixed	0.707	16.5	10.92	1803.20	1745.00	355.60	Johnson
GMA	Free-Fixed	2	16.2	0.38	62.59	78.05	1.20	Euler
	Guided-Fixed	0.5	8.25	6.18	510.05	635.98	156.40	Johnson
	Pinned-Fixed	0.707	16.5	3.09	510.20	636.17	78.29	Euler
GMC	Free-Fixed	2	16.2	0.17	28.05	0.99	0.0017	Euler
	Guided-Fixed	0.5	8.25	2.77	228.59	8.14	0.23	Euler
	Pinned-Fixed	0.707	16.5	1.38	228.60	8.14	0.11	Euler

Table 3-6: Results from critical values calculations for a cylindrical volume.

Hexagonal Prysm		Boundary Condition	E exp (GPa)	Crt Strain (%)	Crt Stress (MPa)	Crt Force (μN)	U (pJ)	Model
HC100	Free-Fixed	2	16.2	0.436	70.64	50.58	0.628	Euler
	Guided-Fixed	0.5	8.25	6.97	575.63	412.2	81.96	Johnson
	Pinned-Fixed	0.707	16.5	3.48	575.8	412.3	41.09	Euler
AGM1	Free-Fixed	2	16.2	1.82	296.28	76.37	1.16	Johnson
	Guided-Fixed	0.5	8.25	29.26	2414.1	622.3	152.07	Johnson
	Pinned-Fixed	0.707	16.5	14.63	2414.9	622.5	76.07	Johnson
AGM2	Free-Fixed	2	16.2	1.13	184.37	147.5	3.13	Euler
	Guided-Fixed	0.5	8.25	18.2	1502.3	1202	408.2	Johnson
	Pinned-Fixed	0.707	16.5	9.1	1502.7	1202	204.23	Johnson
GMA	Free-Fixed	2	16.2	0.322	52.16	53.79	0.689	Euler
	Guided-Fixed	0.5	8.25	5.15	425.04	438.2	89.87	Johnson
	Pinned-Fixed	0.707	16.5	2.57	425.17	438.42	44.96	Euler
GMC	Free-Fixed	2	16.2	0.14	23.37	0.688	0.0009	Euler
	Guided-Fixed	0.5	8.25	2.3	190.4	5.61	0.13	Euler
	Pinned-Fixed	0.707	16.5	1.15	190.5	5.615	0.065	Euler

Table 3-7: Results from critical values calculations for a hexagonal prysm volume.

As it was observed from Table 3-6 and Table 3-7 for both volumes calculated, the highest levels of strain energy accumulated during theoretical compression, were for the Johnson's cases. As it was mentioned before, Johnson model is more accurate for short or intermediate columns, whereas Euler's model is no longer useful. It is important to state that a high level of energy on Johnson cases do not corresponds to a reliable energy storage behavior. Due to, its slenderness ratios have lower values than the critical slenderness ratio, meaning, that they may buckle inelastically or collapse directly [87].

Therefore, a cycle of energy storage with Johnson model behavior is a non reliable energy storage cycle behavior, at least theoretically. On the other hand, for samples correspondent to the Euler cases, samples *HC100* and *GMA* with aspect ratios of 5.4 and 6.3 were found with the highest levels of strain energy. Finally, the only sample on which Euler model was present for all the boundary conditions was *GMC*, showing a high buckling behavior for our three cases of study, but with the lowest levels of strain energy. As a first theoretical approach, it can be seen that aspect ratio influences in an amvibalent way the strain energy levels, especially if aspect ratio is low enough to follow a Johnson model in which the case, it can store high levels of energy but behaving on a non-linear buckling region (*AGM1,AGM2*). Secondly, if the aspect ratio of the *ZnOfw* is high enough for behave as an Euler model for the majority of the boundary conditions, they may buckle linearly and stable but its energy levels do not necessary be high enough (*GMC*), and then, density has to play an important role, to increase the energy that can be stored due to a big amount of *ZnOfws*, on a defined area. Finally, with an intermediate aspect ratio (*HC100, GMA*) a linear buckling and higher levels of strain energy can be achieved.

As it was mentioned in this section this is a first theoretical approach and no conclusive assumptions can be made. Therefore, in order to go deeply into the analysis the next section is dedicated to simulate every single case of boundary condition, found for each of our *ZnOfw* samples.

3.4. FEM Simulation model for a single ZnO finewire

In this section the mechanical analysis will be continued through the use of COMSOL Multiphysics as our Finite Element Simulation (FEM) software, to solve the theoretical mechanical behavior for a single *ZnOfw* by performing three diferent studies, for two different geometries Cylindrical body and Hexagonal Prysm.

Firstly, a study of linear buckling will be performed, with the objective of extract the same critical values observed in the previous section for the buckling point. Like in the theoretical section, the same values of *ZnO* Young's modulus according to its boundary condition will be taken from the literature showed on Table 3-1. The analysis gives us the critical stress σc, from which the buckling starts. From this main value all the other values, can be computed.

Secondly, a static study will be performed to analyze the spring constant of the *ZnOfw*. Similary to the first study, the finewire is submitted to compression, but in this case a force is applied with the same value of the critical load. Then, spring constant can be calculated through the evaluation of the displacement on the structure, in combination with the applied force.

Finally, the third study consists in the Von Misses Yield criterion, to analyze until which level of stress can be submitted the *ZnOfw* before it enters in a plastic region.

3.4.1. Study 1: Linear buckling simulation

For this study all *ZnOfws* were simulated in two different groups of simulations differenced by its geometry (cylindrical and hexagonal prysm body). These bodies were built, with the same dimensions observed on Table 3-2. As before, material properties for *ZnO* were taken from Table 3-1. For every *ZnOfw* sample, the same three boundary conditions were simulated: free-fixed, guided-fixed and pinned-fixed (see Figure 3-7 and Figure 3-8).

Cylindrical Volume		Boundary Condition	E exp (GPa)	Crt Strain εc(%)	Crt Stress σc(MPa)	Crt Force Fc(μN)	U (pJ)	MRE Th. Vs.Sim (%)	Model
HC100	Free-Fixed	2	16.2	0.51	84.18	72.89	1.07	1.29	Euler
	Guided-Fixed	0.5	8.25	6.51	537.26	465.22	86.34	26.46	Johnson
	Pinned-Fixed	0.707	16.5	3.60	595.29	515.40	53.00	16.84	Johnson
AGM1	Free-Fixed	2	16.2	2.07	335.68	104.64	1.81	6.87	Johnson
	Guided-Fixed	0.5	8.25	16.23	1339.31	417.49	56.59	59.98	Johnson
	Pinned-Fixed	0.707	16.5	10.46	1727.54	538.52	47.07	46.41	Johnson
AGM2	Free-Fixed	2	16.2	1.32	214.35	207.42	5.11	3.85	Johnson
	Guided-Fixed	0.5	8.25	12.58	1038.30	1004.70	235.84	48.51	Johnson
	Pinned-Fixed	0.707	16.5	7.65	1262.90	1222.14	174.46	35.20	Johnson
GMA	Free-Fixed	2	16.2	0.38	62.37	77.77	1.19	0.39	Euler
	Guided-Fixed	0.5	8.25	5.10	421.50	525.50	106.87	20.97	Johnson
	Pinned-Fixed	0.707	16.5	2.77	457.41	570.35	62.93	12.67	Euler
GMC	Free-Fixed	2	16.2	0.17	28.08	1.00	0.0017	0.42	Euler
	Guided-Fixed	0.5	8.25	2.54	209.57	7.46	0.1900	10.23	Euler
	Pinned-Fixed	0.707	16.5	1.32	219.30	7.81	0.1040	5.11	Euler

Table 3-8 Results from FEM simulation for Cylindrical body on ZnOfws.
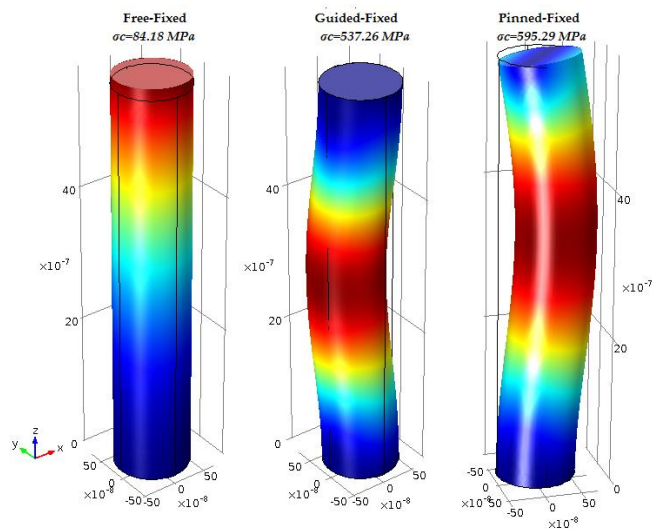
Figure 3-7: FEM Simulations results of critical stresses for sample HC100.

Hexagonal Prisma		C Lobontiu	E exp (GPa)	Crt Strain εc(%)	Crt Stress σc(MPa)	Crt Force Fc(µN)	U (pJ)	MRE Th.Vs.Sim (%)	Model
HC100	**Free-Fixed**	2	16.2	0.43	70.68	50.58	0.761	10.90	Euler
	Guided-Fixed	0.5	8.25	5.7	470.51	407.42	66.22	14.21	Johnson
	Pinned-Fixed	0.707	16.5	3.08	500	433.03	38.09	9.25	Euler
AGM1	**Free-Fixed**	2	16.2	1.74	282.74	88.13	1.28	8.68	Johnson
	Guided-Fixed	0.5	8.25	14.74	1216.57	379.23	46.69	51.90	Johnson
	Pinned-Fixed	0.707	16.5	9.3	1534.76	395.2	30.66	42.27	Johnson
AGM2	**Free-Fixed**	2	16.2	1.11	179.84	174.03	3.6	9.31	Euler
	Guided-Fixed	0.5	8.25	11.23	926.72	741.62	155.36	44.21	Johnson
	Pinned-Fixed	0.707	16.5	6.69	1104.74	884.09	110.39	31.34	Johnson
GMA	**Free-Fixed**	2	16.2	0.32	52.49	54.13	0.698	0.80	Euler
	Guided-Fixed	0.5	8.25	4.46	368.48	379.96	67.54	16.21	Johnson
	Pinned-Fixed	0.707	16.5	2.36	389.41	401.55	37.7	10.28	Euler
GMC	**Free-Fixed**	2	16.2	0.14	23.7	0.698	0.001	3.49	Euler
	Guided-Fixed	0.5	8.25	2.22	183.28	5.4	0.12	4.66	Euler
	Pinned-Fixed	0.707	16.5	1.11	184.7	5.44	0.061	3.95	Euler

Table 3-9 Results from FEM simulations for Hexagonal prysm body on ZnOfws.
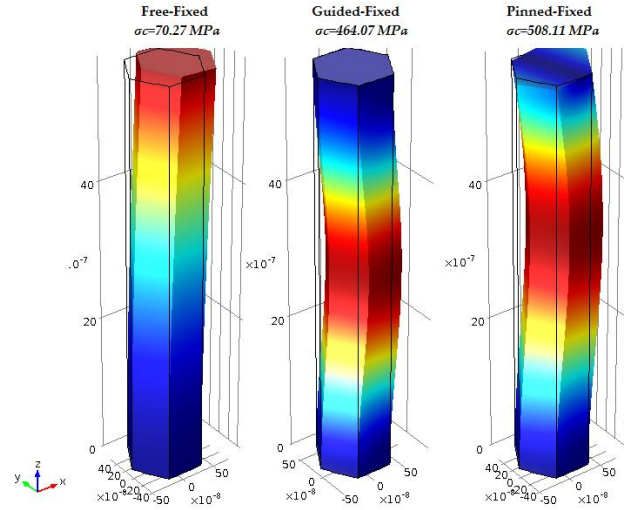
Figure 3-8: FEM Simulation critical stresses results for sample HC100.

Figure 3-7 and Figure 3-8 showed a good agreement between the simulated and analytical critical values,the larger relative error values was found on the Johnson cases, showing values larger than 20%. On the other hand for the Euler cases an average relative error of 5% was found. The displacement and the spring constant can not be computed by this study, therefore, a stationary study, which neglects the buckling point has to be performed to extract these values. In the next section the general details of this stationary study are described.

3.4.2. Study 2: Spring constant simulation

This study is dedicated to analyze the spring constant value, and the total displacement of the ***ZnOfw.*** Through the application of a compression force (***Fc***) at the top face of the ***ZnOfw***, the displacement of the finewire will be estimated. Afterwards, relating the ***ZnOfw*** original length (***L₀***) with the simulated displacement (***L***), the total displacement can be compute (***ΔL=L₀-L***), finally the spring constant (***k***) can be calculated using the ***Hooke's Law*** expression showed on equation 3.22:

$$F = k * \Delta L \qquad\qquad (3.22)$$

Expression (3.22 can be rewritten to extract the spring constant k as follow:

$$k = F/\Delta L \qquad\qquad (3.23)$$

As in the first study, simulations were grouped by two geometries cylindrical and hexagonal prysm. The results were compared with the analytical ones in order to calculate the relative error ***(Kerr.)*** on the last column, all results are summarized in Figure 3-9 and tables Table 3-10 , Table 3-11.

Cylindrical Volume		KTh (kN/m)	KSim (kN/m)	Kerr (%)
HC100 **(L/D)** = 5.43 ± 0.2	**Free-Fixed**	2.48	2.479	0.11
	Guided-Fixed	1.25	1.26	0.51
	Pinned-Fixed	2.51	2.52	0.35
AGM1 **(L/D)** = 2.65 ± 1.4	**Free-Fixed**	3.03	3.06	0.98
	Guided-Fixed	1.54	1.56	1.29
	Pinned-Fixed	3.08	3.12	1.29
AGM2 **(L/D)** = 3.36 ± 0.6	**Free-Fixed**	4.22	4.25	0.70
	Guided-Fixed	2.14	2.16	0.94
	Pinned-Fixed	4.28	4.33	1.07
GMA **(L/D)** = 6.32 ± 2.6	**Free-Fixed**	2.58	2.55	1.18
	Guided-Fixed	1.29	1.3	0.55
	Pinned-Fixed	2.59	2.6	0.52
GMC **(L/D)** = 9.44 ± 0.44	**Free-Fixed**	0.28	0.288	1.16
	Guided-Fixed	0.15	0.146	0.14
	Pinned-Fixed	0.29	0.293	0.16

Table 3-10: Theoretical vs. Simulated results for spring constant estimatation.

Hexagonal Prisma		KTh (kN/m)	KSim (kN/m)	Kerr (%)
HC100 **(L/D)** = 5.43 ± 0.2	**Free-Fixed**	2.04	2.052	0.82
	Guided-Fixed	1.04	1.045	0.72
	Pinned-Fixed	2.08	2.09	0.55
AGM1 **(L/D)** = 2.65 ± 1.4	**Free-Fixed**	2.51	2.57	2.28
	Guided-Fixed	1.27	1.28	0.51
	Pinned-Fixed	2.55	2.57	0.87
AGM2 **(L/D)** = 3.36 ± 0.6	**Free-Fixed**	3.50	3.51	0.30
	Guided-Fixed	1.77	1.78	0.53
	Pinned-Fixed	3.54	3.57	0.81
GMA **(L/D)** = 6.32 ± 2.6	**Free-Fixed**	2.10	2.11	0.54
	Guided-Fixed	1.07	1.076	0.66
	Pinned-Fixed	2.14	2.15	0.32
GMC **(L/D)** = 9.44 ± 0.44	**Free-Fixed**	0.24	0.239	2.25
	Guided-Fixed	0.12	0.121	0.29
	Pinned-Fixed	0.24	0.243	0.03

Table 3-11: Theoretical vs. Simulated results for spring constant estimation.
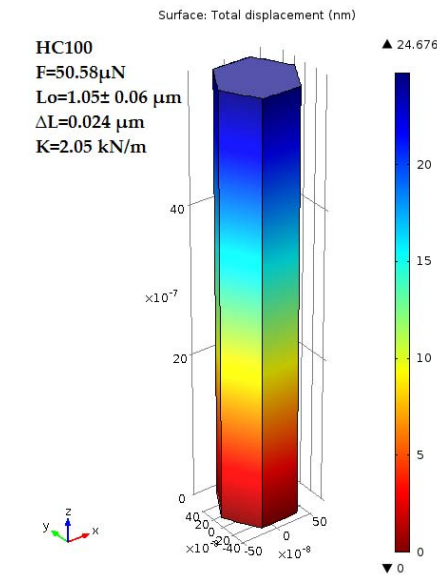
Figure 3-9: Results from spring constant simulation on sample HC100 with an hexagonal prism model.

For most of the spring constant simulated results, a good agreement between analytical and simulated was found, with an average relative error for the cylindrical model of **0.73%** and for the hexagonal prysm model of **0.77%**. Once it has been calculated for the linear region, the critical values and the spring constant, a final study dedicated to emulate behaviors at the limit of the elastic region will be performed. For this purpose, in next section the use of the Von Misses Yield criterion will be described.

3.4.3. Study 3: Von Misses Yield criterion

Once the linear elastic region have been discussed an analyzed for the mechanical analysis of our **"spring-like"** material (**ZnOfws**), the analysis will continue exploring the elastic region for our material. This study is dedicated to perform simulations taking the Von misses yield criterion, as a new parameter to locate up to which level of stress, the material can withstand before start yielding.

With COMSOL the values of the Von Mises stress can be approached by perform another stationary study and, by applying to the **ZnOfw** a force with the same value as the critical load computed in the first study, the corresponding Von Mises stress value can be extracted. Results from these simulations are showed on Figure 3-10 and Table 3-12 showing both models for cylindrical and hexagonal prysm.

Von Mises Simulations		Cylindrical Von Mises σv(MPa)	Hex.Prysgm Von Mises σv(MPa)
HC100	Free-Fixed	108.75	85.3
	Guided-Fixed	886.1	695.1
	Pinned-Fixed	886.37	695.3
AGM1	Free-Fixed	581.1	493.3
	Guided-Fixed	4734.6	4020.0
	Pinned-Fixed	4736.0	4021.5
AGM2	Free-Fixed	342.5	275.5
	Guided-Fixed	2790.5	2245.1
	Pinned-Fixed	2791.3	2245.8
GMA	Free-Fixed	84.6	58.0
	Guided-Fixed	689.5	472.9
	Pinned-Fixed	689.7	473.0
GMC	Free-Fixed	38.0	24.3
	Guided-Fixed	309.6	197.9
	Pinned-Fixed	309.7	197.9

Table 3-12: Results from Von Misses simulation for cylindrical and hexagonal geometries.
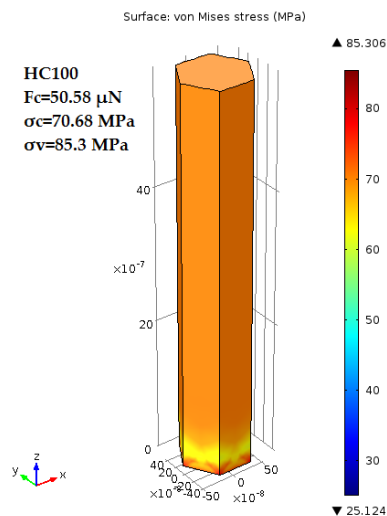
Figure 3-10: Results of Von Mises study on sample HC100.

From these simulations it was observed that Von Mises stresses occur above the critical stress. According to the Von Mises concept, larger stresses will reach the plastic region or directly a failure on the structure. This theoretical analysis is a preliminar approach, further experimental analysis for the *"spring-like"* material have to be performed and discussed on next chapters.

3.5. Summary

In this chapter a preliminar analysis was carried out with the linear elastic theory. The analytical process was carried out, firstly, by the classification of the *ZnOfws* considered as simple columns submitted to a simple compression. Following this approach, *ZnOfws* were classified by its slenderness ratio. From this analysis, two different mechanical models *Euler and J.B.Johnson* were used to calculate the critical values at the buckling point. As it was observed, the *ZnOfws* with small slenderness ratio were considered as short columns that normally do not show linear buckling behavior. On the other hand, samples with higher slenderness ratio were analyzed by the Euler model and have a major possibility to buckle linearly from a theoretical point of view.

Focusing on the theoretical energy amounts obtained, the next preliminar assumptions can be made. First, for small *ZnOfws* (*AGM1 and AGM2*), higher levels of strain energy were observed with values from *2 to 240 pJ*, but as it was mentioned before, small columns also may buckle non-linearly giving an unstable energy storage cycle that may not be practical for the *MESS*. Secondly, for *ZnOfws* with the highest aspect ratio (*GMC*), a high probability of buckle linearly is achieved, but the computed strain energy in the finewire was the lowest of all the samples analyzed, showing that to store big energy amounts, a high density of this finewires will be needed. Finally, for an intermediate value of aspect ratio *(HC100 and GMA)* the highest levels of strain energy with an Euler model behavior was observed.

In the next chapter, the methodology and strategies to follow, for the experimental characterization of the *ZnOfws* samples will be described.

Chapter 4. MECHANICAL CHARACTERIZATION SET UP

T his chapter is dedicated to explain the different strategies used for the mechanical characterization of the *ZnOfws* as our *"spring-like"*material and, as a new alternative the design of a compression set-up for analyze the macro-scale *MESS* proof of concept. Therefore, first the general methodology to follow is explained, describing two strategies proposed for the characterization. The first strategy consists in the *nanoindentation technique*, which is described referencing other works carried out for similar characterizations in *ZnO* nanowires and nanorods.Subsequently, a description of the available equipment for the nanoindentation will be done, explaining the different ways to indent a material, and analyzing which experiments can be carried out, to extract from the experimental results the mechanical properties of the *ZnO finewires*. The second strategy consists on looking forward in terms of scalability for a macro-scale *MESS* proof of concept for which, a compression set-up was designed and fabricated it is described here. Its fabrication is reported in four different sections, explaining the hardware and software modules. The next section is dedicated to explain the calibration process for the compression set-up.

Finally, in the last section, a summary of all the strategies taken to characterize the *MESS* proof of concept are mentioned.

4.1. Methodology proposed for ZnO finewires characterization

On previous chapter, it has been reported a first theoretical approach of the mechanical behavior on *ZnOfws*. This section will describe the methodology to analyze experimentally the *ZnOfws* mechanical properties and as an alternative a macro-scale *MESS* proof of concept.

Two strategies have been selected and are listed as follow:

1) *Nanoindentation technique*: based on previous works reported on the literature [42], [48], [96], [98], [99], [102]–[108]. Nanoindentation technique has been used as a succesfully nano-mechanical testing technique to characterize different nano-structures and materials. For *ZnONWs* and *ZnONRs* it has been used for the Young's modulus experimental approximation. Moreover, through this technique, the buckling behavior on *ZnONWs* has been reported[42], [96], [98], [102]. Therefore, it has been selected as a good alternative to analyze experimentally the individual mechanical behavior and properties on our *ZnOfws.*

2) *Compression set-up for a MESS proof of concept:* as an alterantive to characterize only mechanical properties of *ZnOfws*. The development of a compression set-up is described, in order to reproduce at a macro-scale the mechanical energy storage concept for a macroscopic *MESS*. Keeping this in mind, the design and fabrication of an automatic compression set-up will be explained from its design to its final fabrication. As part of this development, a calibration methodology will be also described.

In the next sections these strategies are explained deeply, in order to delimit the experimental tests to characterize our *"spring-like"* material, and define which results are spected to be obtained. Similarly, for the compression set-up, the conditions of operation will be described, in order to delimit the experiments that can be done with it, and which results can be obtained.

4.2. Nanoindentation technique

As it was mentioned before, nanoindentation technique has been used successfully as a nanomechanical testing technique. It is normally used to determine the hardness and elastic modulus on materials. Such as GaN, syngle cristal and polycrystalline copper wires, tantalum oxide nanowires, gold nanowires, carbon nanotubes, ZnO nanobelts and ZnO nanowire [107] [109]–[114] among others. The main drawback for the nanoindentation technique is due to the deformation, which can be influenced by the substrate and, namely, the substrate has to be taken into account for the measurements done for nanowires grown on it to perform a correct data interpretation.

Therefore, for our particular case, Nanoindentation is one of the most promising techniques to characterize the mechanical behavior of the *ZnOfws,* within the linear elastic region, up to a plastic or fracture region.

Nanoindentation technique has as a main goal the extraction of elastic modulus and hardness of a film on a specific material. It can be done through the indenter load and depth of penetration on the material. For a typical nanoindentation test, a certain load is applied to an indenter making contact with the surface of the sample. Once contact is ensured, the load and depth of penetration is recorded, increasing load from zero to a maximum load stablished, and then removing the load back to zero. During unloading, if a plastic deformation occurs, a residual impression is left in the surface of the sample. From the geometry of the indenter tip and the depth of penetration, the contact area at full load can be approached and then, the hardness may be estimated.

During unload, material attempts to regain its original shape, depending on the elasticity of the material the gradient of recovery that it will have. For materials that have been deformed plastically, is through the analysis of the initial portion of the elastic unloading response, where the elastic modulus can be estimated.

There exist different geometries for nanoindenter tips, the most popular are the *spherical*, the three-sided pyramidal also known as the *Berkovich indenter* and the four-sided *Vickers indenter*.

For the results validation of hardness and Young's modulus, there are different analysis procedures. For our particular case of nanoindenter, the *"Oliver and Pharr"* method will be described[115].

Oliver and Pharr method for indenters

Spherical indenter tip

Considering a spherical indenter tip load on a flat sample, after starting the load application on the sample, an elastic behavior is expected, followed by a plastic deformation, once higher loads are achieved. The depth of penetration is denoted by h_t at full load P_{max} (see Figure 4-1). Once load has been removed, if is assumed no reverse plasticity, the unloading is elastic and at the complete unload, there is a residual impression of depth expressed by h_T. Then, if load P_{max} is reapplied, this reloading is elastic through a distance defined by $h_e = h_t - h_T$ (see Figure 4-1-A), based on Hertz equation[116], [117] load can be expressed by

equation 4.1:

$$P = \frac{4}{3} E^* R^{1/2} h_e^{3/2}$$
(4.1)

Where P is the applied load, R is the relative radius of curvature and E^* is the composite modulus that is defined as follow:

$$\frac{1}{E^*} = \frac{1 - v^2}{E} + \frac{1 - v'^2}{E'}$$
(4.2)

Where the primed terms on (4.2) refer to the properties of the indenter tip and the other terms conform the sample's properties. It has to be mentioned, that since the elastic unloading/reloading involves the deformation of the preformed residual impression, R from equation (4.1) is the relative radius curvature of the residual impression R_r, and the indenter R_i, and is given by equation (4.3).

$$\frac{1}{R} = \frac{1}{R_i} - \frac{1}{R_r}$$
(4.3)

Two considerations have to be done for the analysis. Firstly, it has to be considered that the residual impression is assumed to be identical to the circle formed at contact on full load. Secondly, due to loading/unloading from h_r to h_t is elastic, according to the Hertz equations, the circle of contact beneath the samples free surface consists in the half of the elastic displacement h_e.
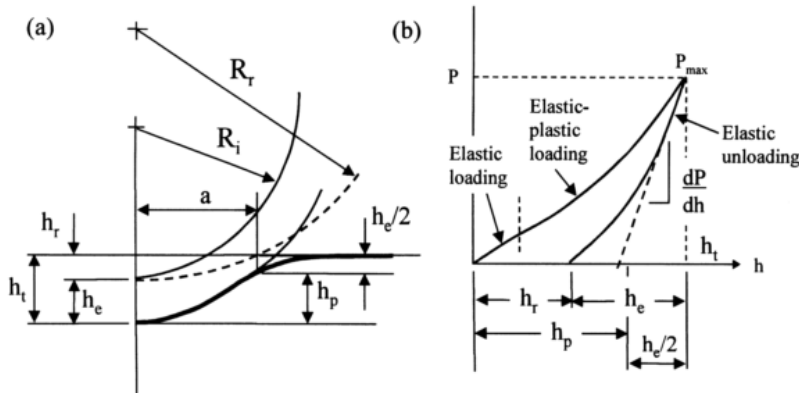
Figure 4-1. (a) Geometry of loading an impression of radius R_r with a rigid indenter radius R_i.(b) Compliance curve (load/displacement) for an elastic-plastic specimen loaded with a spherical indenter showing loading (elastic response) and unloading (elastic plastic response) [115].

The distance from the samples surface at full unload to the depth of the radius of the circle at full load (see Figure 4-1), is defined as:

$$hs = \frac{he}{2},\qquad(4.4)$$

$$ht = hp + hs,$$

$$hp = ht - \frac{he}{2}$$

Once **hp** is known, the resulting radius of circle of contact can be determined by simple geometry (see equation (4.9) from which the area of the contact is calculated and used to determine the mean contact pressure or hardness value **H** given by the expression:

$$H = \frac{P}{A}\qquad(4.5)$$

Where *A* is the area of contact defined by *A =πa²*, been *a* radius of the circle of contact and **P=Pmax**. To calculate the Elastic modulus is needed the Oliver & Pharr method described next.

The **Oliver and Pharr** method [118] is used to calculate **hp,** often referred to the **"plastic depth"**, and is defined by the distance from the circle of contact to the maximum penetration depth. This method uses the slope of the initial portion of the unloading curve to determine **hs** and **hp**. The slope of the unloading curve is defined by the derivative of equation (4.1 with respect to *h* giving expression (4.6:

$$\frac{dP}{dh} = 2\,E^*R^{1/2}\,h_e^{1/2}\qquad(4.6)$$

Then, by the substitution of equation (4.6 on (4.1 the next expression is obtained:

$$P = \frac{2}{3}\frac{dP}{dh}he,\qquad(4.7)$$

$$he = \frac{3}{2}P\frac{dh}{dP},$$

$$hs = \frac{he}{2} = \frac{3}{4}\frac{P_{max}}{dP/dh}$$

Where **hs** is the distance from the edge of the contact to the sample's surface at full load.Once **hs** is calculated **hp** can be calculated from equation (4.4.

From Hertz analysis [116], [117] it is known that elastic displacement is given by :

$$he = \frac{a^2}{R},\qquad(4.8)$$

Where *a* is the radius of the circled contact and is given by:

$$a = \sqrt{2R_i h_p - h_p{}^2} \tag{4.9}$$

Then, equation (4.6 can be rewritten as:

$$\frac{dP}{dh} = 2\, E^* R^{1/2}\, \frac{a}{R^{1/2}}, \tag{4.10}$$

$$\frac{dP}{dh} = 2\, E^* a$$

Finally, the combined modulus of the system can be determined from the slope of initial unloading, expressed by:

$$E^* = \frac{dP}{dh}\frac{1}{2a} = \frac{1}{2}\frac{dP}{dh}\frac{\sqrt{\pi}}{\sqrt{A}} \tag{4.11}$$

Where $A = \pi a^2$, and is the contact area, this relation applies to all axis symmetric indenters with a smooth profile.

Berkovich indenter tip

For a three-sided *Berkovich* indenter tip, similar treatments with the Oliver&Pharr method can be used. This indenter has an included half-angle of 65.3°, its relationship between the projected area *A* and the depth *hp* is given by:

$$A = 3\sqrt{3}\, hp^2 \tan^2 65.3 = 24.5 hp^2 \tag{4.12}$$

For this analysis *hp* can be calculated with the previous mentioned calculations. Moreover, for this geometry in particular it has to be considered as reference, an axis-simmetric cone, rather than the non-symetric pyramidal indenter. To summarize the analysis the general expression for the Elastic modulus is given by :

$$E^* = \frac{dP}{dh}\frac{1}{2hp}\frac{1}{\beta}\sqrt{\frac{\pi}{24.5}} \tag{4.13}$$

β is a yield correction factor equal to 1.034, appropiated for the Berkovich indenter.

Once it has been explained the Nanoindentation technique in detail, the commercial equipment provided by a collaboration with the Catalan Institute for Research and Advanced Studies (ICREA) and courtesy of Professor Jordi Sort[119], [120] will be described next:

A) **CSIRO Ultra Micro Indentation System (UMIS):** its load is given via leaf springs by expansion of a piezoelectric load actuator, the deflection is measured through a force linear variable differential transformer (LVDT) (see Figure 4-2a).. It has a force resolution less than 0.1 mN, determining depths of penetration with a resolution less than 1 nm, it was used with a flatten cone-shaped diamond indenter tip, with diameter of 14 μm. The measurement cycle of loading/unloading is followed under computer control, through factory software[121].

B) **Anton Paar Table Top Nanoindentation Tester (TTX-NHT2):** the NHT2 is designed to provide low loads with depth measurements in the nanometer scale for the measurement of hardness, elastic modulus, creep, between others(see Figure 4-2b).. The force is applied by an electromagnetic actuator, and its displacement is measured via a capacitive system. It has a maximum depth of penetration of 200 μm, a resolution of 0.01nm, load frame stiffness > 10^7 N/m[122]. A diamond four-sided Berckovich indenter tip rounded with a 60 to 90 nm radius, with angle of 60°, was used for all experimental procedure.
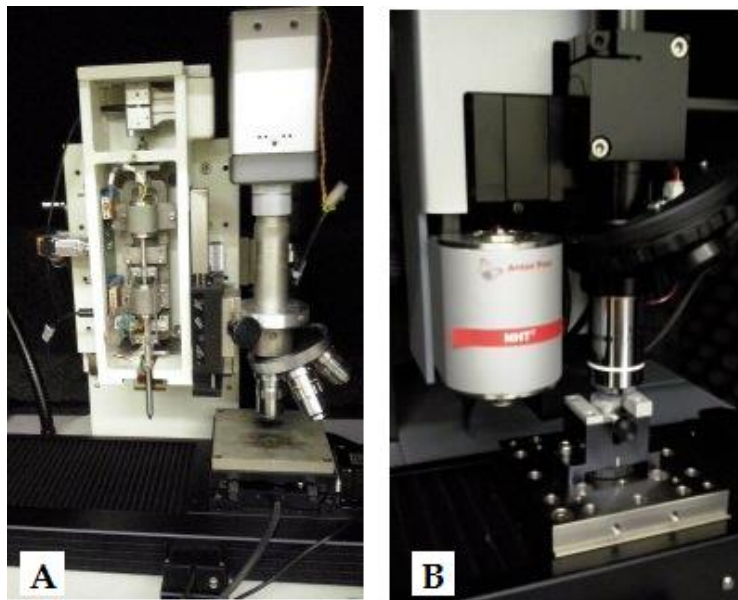
Figure 4-2: [A] UMIS 2000 Ultra Micro Indentation System. [B] Anton Para TTX-NHT2 Nano Hardness Tester.

Once the indenters and the nanoindentation technique were described, the next section is dedicated to explain an alternative compression set-up, with goals of proof of concept.

4.3. Compression set-up for a MESS proof of concept

Previously, the Nanoindentation technique and indenters equipment used were described. In this section, an alternative focused in analyze the conceptual *MESS* behavior will be done. Due to the Nanoindentation technique is more useful, to analize the mechanical properties of the *ZnOfws* as our *"spring-like"* material. It is necessary to have, a macro-scale point of view of how the *MESS* will perform to store mechanical energy. Therefore, as it was explained in Chapters 1 and 3, the energy storage cycle, is given by the multiple deformations that occur for each *ZnO* finewire during compression. Namely a larger contacted area, and larger forces than an indenter can cover, have to be achieved for this goal.

Motivated by this necessity to fulfil, a first approach for analize the gradient of compression for multiple *ZnOfws* was done. It consists in use the semiconductive properties of the *ZnO*, to measure the level of strain that the *ZnOfws* can have. Therefore, by using the interface naturally created on the Hydro Thermal Method (*HTM)* growth between *Si/Au* and *ZnO* from the finewires, and adding the compressor substrate conformed equally by *Si/Au*, an electrical interface was created. The proposal is to relate, as a preliminar study, the current level that can pass through a wide surface of *ZnOfws* over the sample, with the mechanical compression performed on different levels, in order to see if, the relation between compression distance and current level has any significant agreement, to use it as an indirect measurement of how loaded the *MESS* is.

For this preliminar test, the top substrate was fixed on a polycarbonate custom-designed arm, which was installed in a probe station. The bottom substrate with the *ZnOfws* sample was placed in a sample holder of the probe station, beneath the top substrate (see Figure 4-3). Once all hardware was set, the electrical connections were made, we connect the top substrate to the semiconductor analyzer, and the bottom substrate to ground (see Figure 4-4).
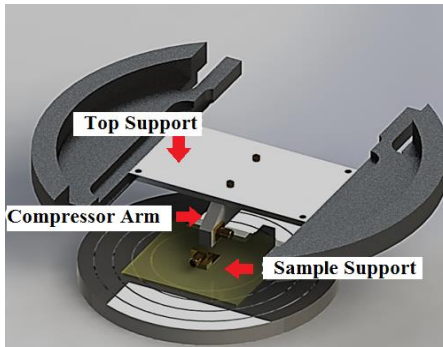
Figure 4-3: Experimental compressor
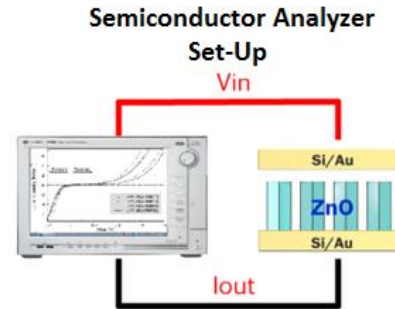
Figure 4-4: MESS preliminar proof of concept. Connections of the interface Si/Au/ZnO/Au/Si to the semiconductor analyzer for electromechanical test.

The main aim of the electro-mechanical test is to measure the IV characteristic of the *ZnOfws* when the compression of the sample is varied. Firstly, the top substrate has to be approached to the top of sample, close enough to make contact with the *ZnOfws*. Then, once the contact is ensured, a slope voltage is introduced and the output current response is measured. According to previous studies on characterization of ZnO nanowires [39], [123] the thermionic-emission is the main conduction mechanism, this behavior has been demonstrated through solving the thermionic-emission conduction equation, showing a qualitative predominance at reversely biased Schottky barrier. All the experimental procedure and results were reported by *O.G. Suchil et. al*[86].

The main trend observed from these experiments was, as more compressed and contacted are the *ZnOfws*, larger is the current density found on the interface (see Figure 4-5). Another aspect that has to be mentioned is a rectifier *Schottky* behavior, and for positive VBias during the compression tests, the peak of current has a proportional relation with the compression level.

As it was mentioned, this was a preliminary test for measure indirectly the *MESS* loading level. The main drawback on this experiment was given by the lack of accuracy on the compression distance measurement, besides the absence of the compression force measurement.
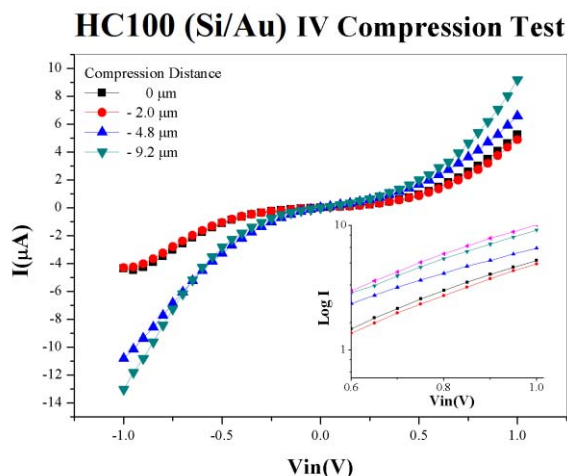
Figure 4-5: IV Characteristics for different compressions shows as larger is the compression larger is the current. Inset shows a clear increasing trend on the currents

Therefore, having a compression set-up, which can measure simultaneously, compression force/distances for a macro-scale contacted areas, can help us to achieve our goal, of analyze macro-scale *MESS* proof of concept. As an addition to this system, an electrical module is also beneficial to see the current behavior during different levels of compression on the *ZnOfws*. It has to be mentioned, that the use of an Indenter or an AFM with a conductive tip, is not available as part of our equipment of measure. Then, the design and fabrication of a compression set-up dedicated only to our *MESS* characterization was the most viable option to follow.The general description of all the design and fabrication process, for this costumized compression set-up (*CCS)* is reported on the next sections.

4.3.1.   General features of the costumized compression set-up (CCS)

With the main purpose to obtain accurate measures of displacement, force and current, as indirect compression measurement, the general tasks to full-fill for the Costumized Compression Set-Up (CCS) are listed below:

1) Compression displacement: to complete this task is necessary the use of an accurate displacement component. As it was mentioned before, indenters use piezoelectric or electromagnetic actuators, to provide an accurate displacement. Therefore, for our particular case and without reaching the same resolution of displacement due to our final application is more at macro-scale, an accurate piezoelectric actuator will be considered.

2) Compression force: to read Force/Displacement curves, is necessary to provide the CCS with a force sensor, which fulfils the range of compressions we plan to perform. This sensor will be limited by its minimum resolution and its maximum force to withstand have to be compatible with the displacement actuator, to avoid a malfunction on both.

3) I-V sweeps during compressions: during the compressions, as it was described in previous section, it is planned to read through an I-V sweep on the ZnOfws, how compressed they are and again look if the trend firstly observed with the arm of the compressor experiment is reproducible. Then, it is necessary to adapt on the CCS, a controlled I-V sweep current amplifier.

If the general features are fulfilled succesfully, it is necessary to consider two main aspects for the design and fabrication of the CCS. Firstly, it has been mentioned that testing the MESS at a macro-scale point of view consists in increase the contacted area for the ZnOfws, that a commercial indenter can cover, but also having a CCS will allow us to analyze different conceptual MESS with different "spring-like" materials, without been limited to our first "spring-like" material ZnOfws, giving a generic use for the CCS. The second aspect to consider is that the CCS needs a dedicated software that reads and controll its components. Therefore, to accomplish this task, dedicated software which provides control has to be designed and developed.

4.3.2. Selected compontents for the design of the CCS

The different selected components that conform the *CCS* are based in analyze the minimum equipment needed to built it, taking into account for the selection always the cheapest but functional components. The results for this selection are separated by the task to fulfil and listed below:

1.-Compression displacement: to provide the *CCS* with an accurate and controlled displacement, the piezoelectric picomotor *NewFocus 8302* was chosen. It has a minimum resolution of *30 nm* of displacement, with a total travel range of *25.4 mm,* it can withstand a maximum force of *22 N*. It has a long-term stability due to the fact that it can hold its position with no power applied[124]. It is controlled by factory software through *Model 8742 Picomotor Controller/Driver*, which is a 4 axis open-loop intelligent motion controller/driver. It can be controlled through Ethernet or USB port[125], compatible with LabView and Microsoft enviornment.

2.-Compression force: to read the compression force on the *CCS*, the *FSSeries FSG15N1A Force Sensor* was chosen. It is a piezoresistive micro-machined silicon sensing element configured as a wheatstone bridge. It has a minimum force resolution of *9.81 mN* and, its maximum force range is of *15 N*, which give us a good agreement with the piezoelectric picomotor (*22 N*), avoiding to reach the maximum force that the picomotor can resists. Its output is analogue, through a differential voltage with a minimum sensitivity of *0.24 mV/grF ≈ 9.81 mN*[126]. To the correct assemble of this component an amplification circuit is needed.

3.-IVSweep: for the *IV* curves sweep, it was used a commercial *Low-Noise Current Preamplifier Model SR570 from Standford Research Systems*, which amplifies the current that comes from the sample. This reading is given by converting the current to voltage and aplify it. This equipment allows an automatic control through a RS232 serial communication.

4.-Data acquisition and control Software: due to, the force sensor and the current amplifier output are analogue signals, it is convenient an accurate data acquisition. To accomplish this taks, a data acquisition unit (DAQ USB 6001), from the provider National Instruments is used[127]. The DAQ USB-6001 is a full speed USB device that provides eight single-ended analog input (AI) channels, 13 digital input/output (DIO) channels, and a 32-bit counter. It has a 14 bit resolution for analogue input/output ports, with a sample rate of 20kS/s. Its maximum input voltage is of ±10V, then, it has to be considered for the amplification gain on the force sensor and the current amplifier, avoiding overcome this limit. As in the case of the picomotor, it can be controlled through LabView and is compatible with Microsoft environment.

According to the factory software of the *New Focus Picomotor 8302* and the *DAQ USB 6001*, it was observed that having two different graphic user interface (GUI) softwares to perform a measurement, results unpractical and slow for the *CCS* performance. Therefore, taking advantage of the fact these systems are compatible with Microsoft environment, we decide to develop a single GUI to control the overall *CCS*. And for this purpose the software development was done in parallel to the *CCS* assembly.

4.3.3.   Conceptual assembly for the CCS

Once the basic components for the *CCS* have been selected and briefly described, the conceptual assembly has to be defined. Inspired by the commercial indenters, the piezoelectric motor is used as a reliable displacement component, which displacement drives an indenter tip which applies the compression force. For our particular case, the piezoelectric motor will drives a compression. The orientation on which the picomotor has to be installed depends on the force sensor location. Again, taking commercial indenters as reference, where the force sensor reads the compression reaction instead of read directly the compression force, we decide to do the same for the *CCS*. This simplifies the interaction with the sample, and increases the potential operation range in which our selected force sensor can operates. Namely, if force sensor is located beneath the sample to compress, and if the sample has a higher hardness than the force sensor, the force readed will not be other than the force sensor compliance. On the other hand, if the compliance and the hardness are known for the force sensor, when the compression reaction is measured, substracting the force sensor harness will give directly the compression force applied to the sample.

If the picomotor is installed on a vertical support, the weight of the support and the picomotor is a disadvantage, due to the fact the normal force conformed by the picomotor and the structure is already acting upon the sample. On commercial indenters this issue is solved with adjustments of springs increasing the complexity of the overall system.

Therefore, to keep a simple design and to avoid the effect of the weight, it was decided to place the picomotor with a horizontal orientation, reducing the weigth issue to the possible friction that could exist in a bearing plataform   (see Figure 4-6).
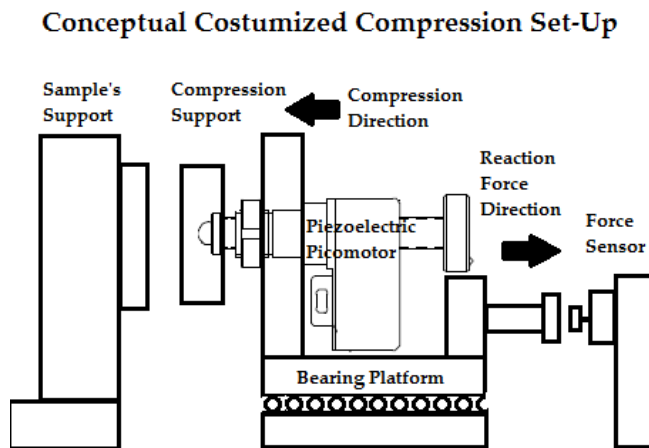
Figure 4-6: Conceptual Costumized Compression Set-Up. The compression direction, force sensor and piezoelectric picomotor location are shown.

Subsequently, to explain from a general view the complete control loop for the *CCS*, it was necessary to split the development in different modules. Each module includes Hardware and a dedicated rutine in the Software to control it. The block diagram is showed on Figure 4-7.

Costumized Compression Set-Up Modules
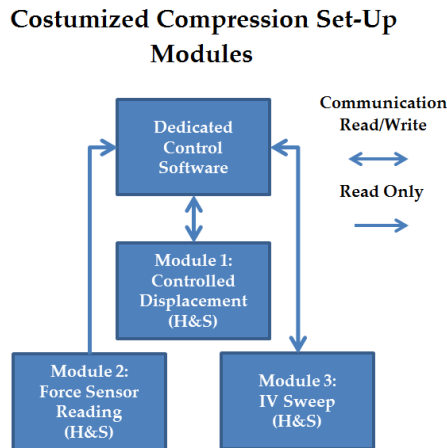
Figure 4-7: Modules of development of the CCS, including communication type.

Once the conceptual description of the **CCS** and the main modules of development has been described, in the next sections all the modules are described deeply dividing the Hardware and Software developments. At the end the dedicated software will be described in order to clarify the integration of all the modules.

4.3.4.   Module 1: Controlled Displacement

This module is dedicated to explain the development of a controlled displacement mechanicsm, performed by a piezoelectric picomotor actuator *New Focus 8302*, controlled initially by its factory software through driver *Model 8742 Picomotor Controller/Driver*. Its displacement is given by a piezoelectric actuator known as Stick/Slip or Inertia Drive which during excitation stage, depending on the polarity, it expands or contracts its structure, moving two jaws that turn a micrometric screw(see Figure 4-8-A). This displacement varies from ClockWise *(CW)* to Counter Clock Wise *(CCW)* due to expansion speed is opposite for each direction. Another aspect to consider during operation for this piezoelectric picomotor is the variation of its minimum displacement unit the *step ≈ 30nm*, this value varies according with the load applied on the actuator, this has to be taken in consideration if the picomotor will be the actuator that performs the sample's compression (see Figure 4-8-B).
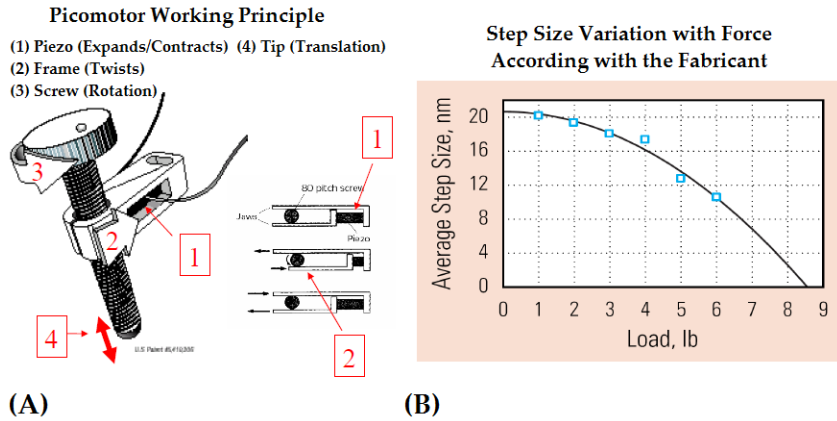
Figure 4-8: (A) Working principle of piezoelectric picomotor. (B) Manufacturer experimental curve for the step size variation as function of the force applied[124]*.*

The picomotor acts as our source of force and controlled displacement during the compression for the *MESS*. Therefore, different strategies were taken into account to solve the main issue of miss-calibration on displacement.

4.3.4.1. Optical Calibration System for correct picomotor's displacement

As a first approach, to solve the factory miss-calibration on displacement found on *CW* and *CCW* directions, an optical solution was considered. This solution was though for small displacements not largers than 10 μm, thinking in the largest *ZnOfws* which have a length ≈ 8 μm. Therefore, our solution consists in provide an analogue responose, from the rotation of the picomotor screw. Namely,a voltage that varies simultaneously to the picomotor's screw rotation, thus it will not matter if the displacement varies from *CW* to *CCW*, because the analogue signal is independent of the picomotor. This reference cannot make contact with the picomotor's screw, because it will add an extra resistance during the compression. Then, an optical solution which varies an analogue voltage output could help to accomplish this task.

For the optical detection, it was used a *BPW77NA* photo-transistor which has a wave-length detection range of *450 to 1080 nm*. It was chosen due to its high photo sensitivity, is suitable detection from visible to near infrared radiation, fast response and its low collector-emmiter saturation voltage from *0.15 to 0.3 V.* It was also a good option due to, in comparison with a photodiode, a phototransistor do not need an amplification signal circuit which is already integrated in its package simplifying its implementation for the approach. Because of *BPW77NA* can detect also visible light and it has to be mounted on the picomotor, to act as a static reference of movement, it was necessary to design and *3D* fabrication of a special housing (see Figure 4-9-B). The phototransistor housing isolates from envioronmental light, avoiding reading failure, and receives only the laser beam to saturate the base of the phototransistor. Complementary to the phototransistor housing, it was also necessary to design the "*Eclipse wheel*", which is installed in the screw head of the picomotor. This wheel has a through hole to graduate the intensity of the laser beamand

follows the rotational movement of the picomotor screw, which is read as a Voltage, which variates according to how saturated the phototransistor is (see Figure 4-9-B).
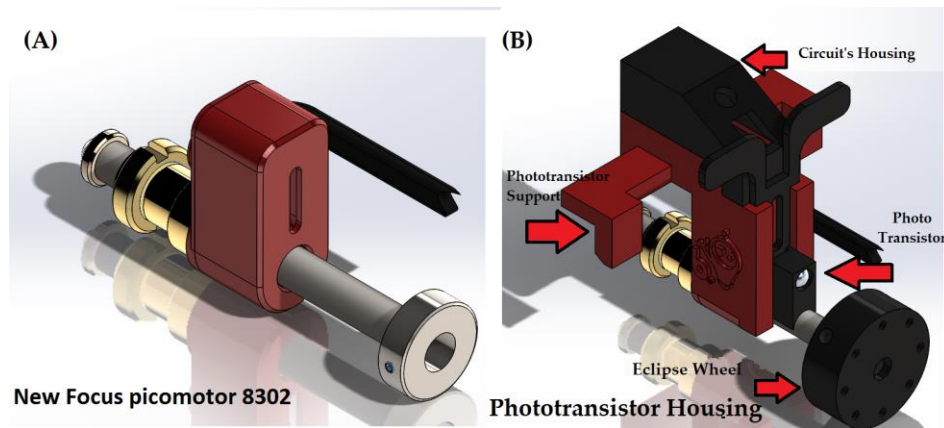
Figure 4-9:(A) Piezoelectric Picomotor New Focus 8302 without housing. (B) Phototransistor installed on Picomotor case.

It was used a comercial laser diode as a laser source which generates a beam with wavelength of *650 nm*, with a light power smaller than *5 mW*, an operating current of *< 40 mA*.A suppy voltage of *5V DC* is needed. Its current is regulated with commercial *LM317T* current regulator. As in the case of the phototransistora housing to protect the regulation circuit and laser diode was fabricated (see Figure 4-10-A and Figure 4-10-B).
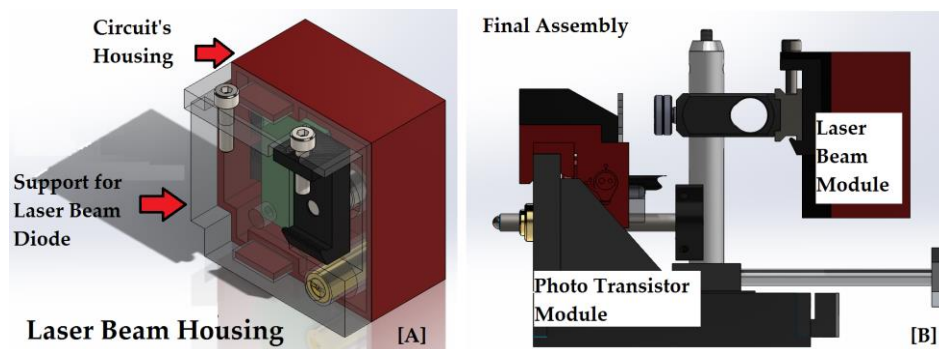
Figure 4-10:(A) Laser beam housing . (B) Final assembly of the laser emition module with the phototransistor module.

OCS Software development

Once all the modules for the Optical Calibration System (*OCS*) were assembled, it was necessary to control the picomotor's displacement and simultaneously read the analogue output from the phototransistor. Therefore, using the factory software from *Model 8742 Picomotor Controller/Driver,* and simultaneously the *DAQ USB 6001* software to make a measurement, results in an unpractical process, due to the fact the picomotor manufactured software is limited to some sequences of displacement, for our case it necessary create our own rutines, and for the DAQUSB manufactured software, the measurements of analogue

signals have to be done manually, slowing the process to obtain an experimental curve. Therefore, it is necessary the creation of specific routines that we plan to perform with the picomotor in response of the phototransistor output. Therefore, it was needed a the development of our costumized software solution for accomplish this task.

To integrate in single software both equipments it was necessary to take out the programmatically classes, that governs the rutines at code level for both equipments. In the case of the *Model 8742 Picomotor Controller/Driver*, the class useful for make costumized Application Programming Interfaces (API's) is named *CmdLib8742*[128]. For the *DAQ USB 6001* the class is called *NI-DAQmx*[129]. Both classes are compatible with a *.NET Framework*, and then any language compatible for this environment can be used. Based on previous experience all the *API* were programmed in *Visual Basic .NET*. The software structure is summarized in Figure 4-11.
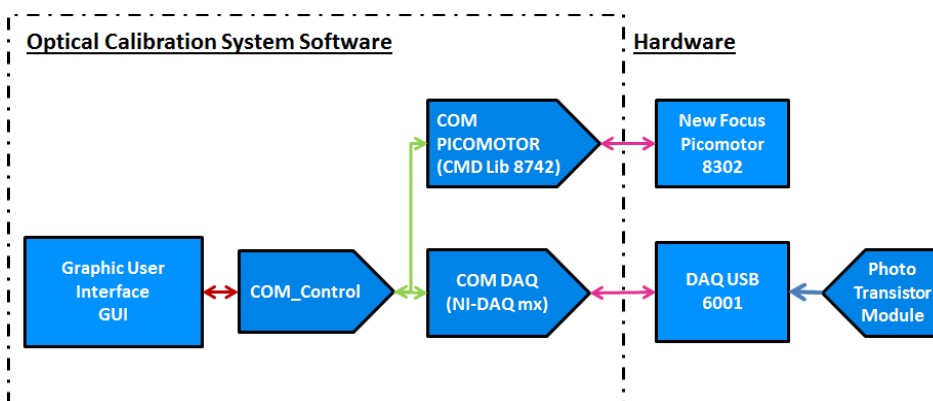
Figure 4-11: Optical Calibration System Software Structure. At left hand side, all modules developed for control the Picomotor and DAQ USB. At right hand side, the connected hardware is showed.

Once the communication classes were integrated to the OCS Software, the next rutines were designed:

1.-Photodetector output reading: this rutine reads the phototransistor output, which is connected to DAQUSB-6001 to an Analogue Port in RSE configuration. Reading can be made by a single measurement or by a multiple measurement, averaging the samples measured and calculating its standard deviation.

2.-Picomotor displacement control: this rutine allows the OCS Software to control the two main displacement types for the picomotor (*absolute, relative*), displacement can be set by varying the number of steps the picomotor can move in *CW* or *CCW* direction.

3.-Search for zero position: this rutine combines rutine 1 and 2, to find the point where the eclipse wheel is aligned with the laser beam, in such a way the maximum saturation occurs on the phototransistor, giving the highest saturation state.

After these rutines were set, it was necessary to obtain the characteristic curve, corresponding to the phototransistor output. To accomplish this task, it was also necessary make tests of the laser beam's alignment to search for the best experimental curve.

<u>*Laser beam alignment*</u>

After basic combined rutines designed for control the picomotor and read-out the phototransistor response, several experiments were done to analyze the characteristic curve of the phototransistor (see Figure 4-12).
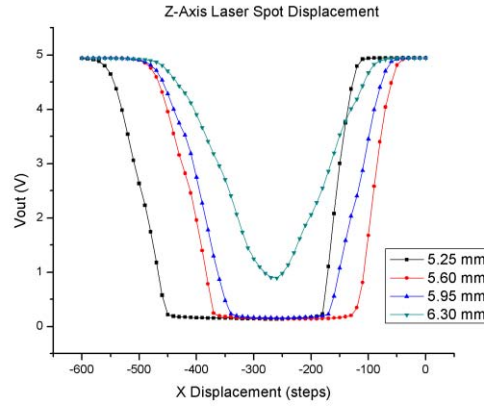
Figure 4-12: Phototransistor output response connected on collector common mode. The Z-Axis Laser spot displacement variation causes the positive offset from 5.25 mm (completely flat curve) to 6.30 mm (Sharpe inverted curve).

From these curves observed on Figure 4-12, it was revealed that the signal can be shaped to our most convenient behavior, through the aligment of the laser beam emitter, the best alligment was fount to be at 6.3 mm, far from the maximum saturation position for the phototransistor. It is the optimal curve, due to it is beneficial for measure an accurate rotation on the picomotor screw, if for each slightly variation of rotation a different output value from the phototransistor is obtained. Once this curve was selected as the optimal, equivalence between voltage and displacement was carried out. This analysis required several experimental tests, measuring a complete revolution on the picomotor first in *CW* and then in *CCW*, reading the response of the phototransistor simultaneously. The final results are shown on Figure 4-13.
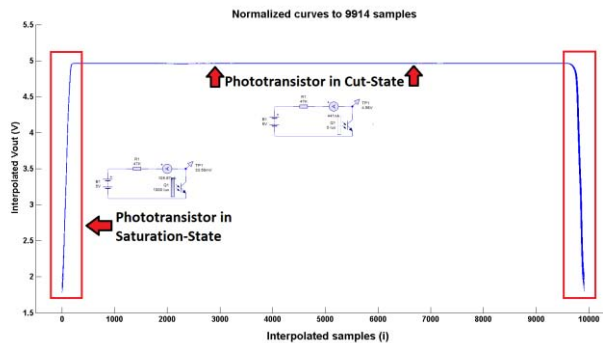
Figure 4-13: Normalized experimental curves for complete revolutions on the picomotor screw. Y – axis show the Phototransistor Output Voltage response, X-axis show the displacement of the picomotor in steps as the minimum unit, locating each sample as a step.

Several complete picomotor rotation tests were done and, the saturation-state sections of the curves were cropped and normalized, taking care of the steps scale to make a correct equivalence. Then, each cropped signal was reassembled, forming a single normalized curve which corresponds to the characteristic curve (see Figure 4-14).
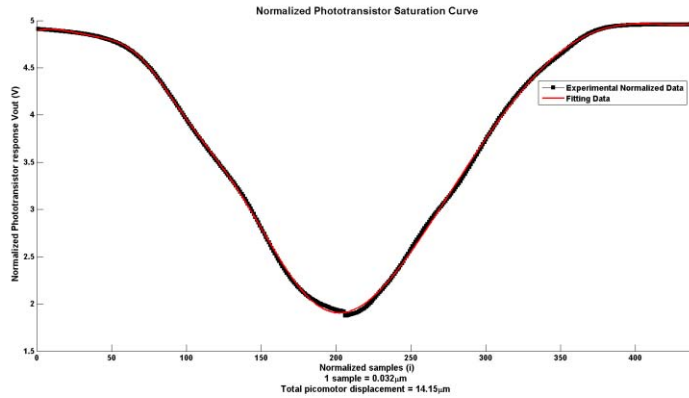
Figure 4-14: The normalized saturation curve for several rotation tests is plotted. The equivalence of samples to microns was given through the fabricant features for the picomotor screw, 80 revs.=22.5 mm ,then 1 rev=317.5 μm=10583 samples, 1 sample=0.032 μm.

Finally, for a designed through hole on the eclipse wheel of 2 mm, a maximum linear displacement of 14.15 μm can be done with the normalized curve of the phototransistor. This equivalence will directly convert the voltage output that comes from the phototransistor in linear distance for the picomotor, measuring an accurate displacement for the picomotor screw.

Operating the Optical calibration system

The calibration rutine to start an accurate displacement can be described as follow:

1) *Locate reference in Zero position:* it make rotate the picomotor in the *CCW* direction, before start an accurate displacement.

2) *Load normalized curve for analysis of phototransistor response:* after place the picomotor in the zero position, the normalized phototransistor curve is loaded with its approximated Gaussian equation.

3) *Set target for displacement:* using the characteristic equation for the normalized phototransistor curve, the target displacement can be converted into a voltage. Once the rotation is started, the program will search for this voltage as the limit of the displacement.

The general view of the GUI developed and the general performance of all rutines previously described are showed on Figure 4-15.
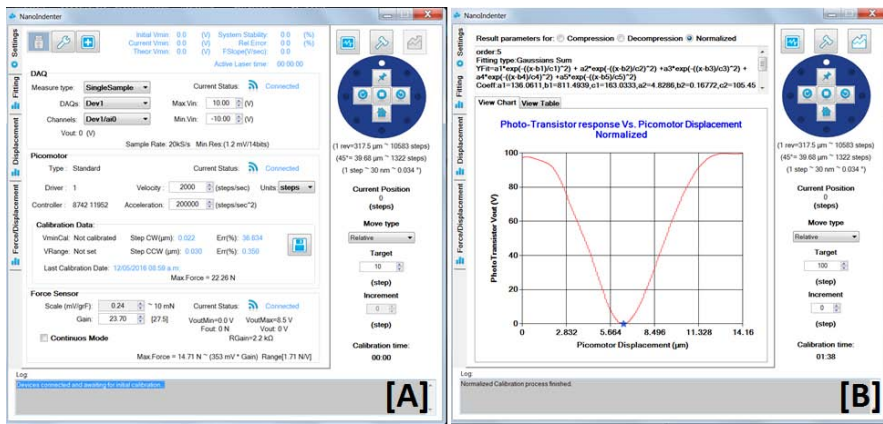
Figure 4-15 [A] GUI developed for CCS control. [B] The normalized curve of the phototransistor for the accurate displacement is shown.

Finally, with this optical calibration solution, the error between **CW** and **CCW** direction for the picomotor was reduced from 40% to 0.8%, for a small range of 5μm of linear displacement for the picomotor. The main drawback, for this solution was related with the small displacement performed in practice, due to the quick variation of the phototransistor between measurements in different periods of time, besides it varies widely with the environmental temperature. Further strategies were taken in to account to increase this displacement range for more macro-scale applications, these will be explained in section 4.3.5.1. The final assembly of the Optical Calibration System is showed on Figure 4-16.
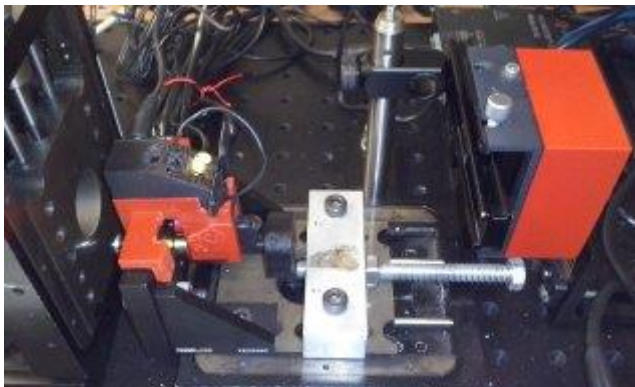
Figure 4-16: : Final assembly of the Optical Calibration System mounted on the CCS.

4.3.5. Module 2: Force Sensor Reading

The **FSG151N** force sensor is a piezoresistive micro-machined silicon sensing element configured as a wheatstone bridge. Its output is a differential signal, which correlates the readed Force with the resistance variation. It has as minimum resolution of **0.24 mV /gF** equivalent to **9.81 mN**. It is known also that for the acquisition equipment, the DAQ USB-6001 has a 14 bit resolution, then its Less Significant Bit (**LSB=1.22mV**) is higher than the minimum response of the force sensor. Then, it is necessary an amplification circuit which

gives the maximum resolution that the DAQ USB-6001 can measure, limited by its ±10V of analogue input. It is also known that the maximum force that the force sensor can withstand is of **15 N**. Then, with its operation rate, the minimum and maximum voltage gain for the amplification can be calculated. Fo the minimum gain on the amplification circuit, an estimated value of **14.11dB**, was calculated based in the less significant bit for the DAQUSB and the minimum resolution of the force sensor. On the other for the maximum gain was of **28.9dB**, calculated with the maximum resolution that the Force sensor can reach and the maximum input voltage that the DAQUSB can read.

Due to the fact that the differential output from the FS Sensor is lower than 1 mV, it is exposed to external noise and a high common mode voltage that affects the measurements. In order to reject the common mode voltage (CMR), it is need a circuit that reject as possible possible the external noise before the amplification and only amplifies the differential signal. Therefore, in order to accomplish this and due its high accuracy an instrumentation differential amplifier will be selected. This IC receives a differential voltage (Vd) conditioned in two main phases: the first one is the amplification of the differential input (Vd) and rejecting the noise or the common mode voltage (Vcm) and the second one is the differential amplification with unipolar output with a common mode gain (GCMR), leaving Vd with the highest gain. A circuit that accomplish with this requirements is the circuit **INA411**[130] which is a general purpose instrumentation amplifier that offers excellent accuracy, its versatile 3 op amp design and small size make it ideal for a wide range of applications. It allows a suitable gain range of 1 to 10000. Its general composition is described in figure Figure 4-17.
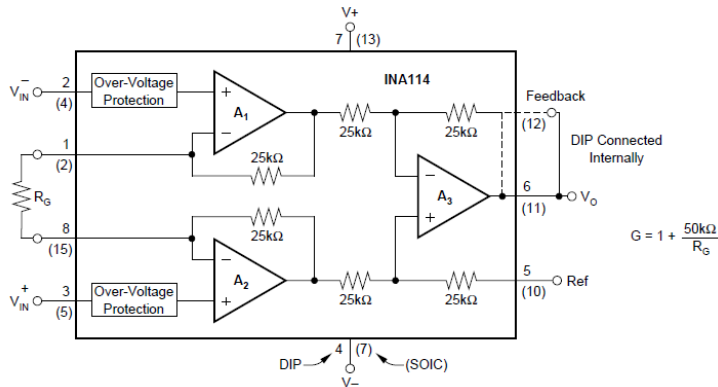
Figure 4-17: General composition of INA114 for its models 8-Pin Dip and SOL-16 Surface-Mount.

According to the gain equation expressed on Figure 4-17, and by using commercial resistor values to achieve a Gain Rate between **14.11** and **28.9 dBs**, the resultant Gain rate was updated to **14.25** and **27.5 dB**, using resistors with values from **12 kΩ** to **2.2 kΩ**.

Once these values were calculated, and considering the typical operating conditions needed for the **INA411**, the final circuit was implemented (see Figure 4-18).

Finally, once the differential output from the Force sensor **FSG151N** was amplified successfully, it was read in the same configuration as for the phototransistor described before. Therefore, an analogue port from the DAQ-USB6001 was used to read the analogue

output. To obtain the force measurement it was necessary to convert the voltage read, by the expression : F=(Vd*9.81mN)/0.24mV, where Vd is the differential voltage which is affected by the gain, thus Vd=Vout/Gain, where Vout is the amplified signal read by the DAQ-USB6001. After testing the circuit and validating the force reading, it was necessary to integrate on the *CCS GUI* , the rutines that allow to read force/displacement curves, in order to analyze the compressed material or for our case the macro-scale *MESS* proof of concept.
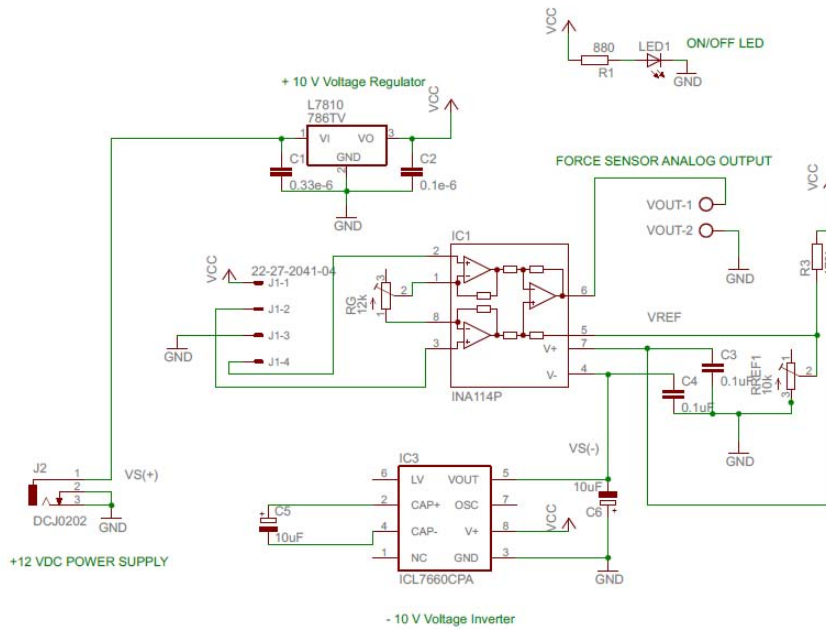
Figure 4-18: General Schematic of the Force Sensor Amplifying Circuit.

1.- General Force reading: from a selected analogue port on DAQ-USB6001, it was carried out the force reading in the RSE configuration. This measurement can be as in the case of the phototransistor, the output could be a single measurement or a multiple, calculating an average value of Force, and also the standard deviation obtained.

2.- Set Force target for displacement limit: independent of the displacement, this rutine allows to compress a structure without calculating the distance displaced, instead a force value is used, allowing for macro-scale compressions make the measurement simple.

Force Sensor Calibration

To make a measurement it is necessary to understand how forces operate in the mobile structure where the picomotor is placed on the *CCS*. In order to extract the minimum value for the spring constant of the material (K), which can be measured for the FS Sensor Series used in the compression set-up, is necessary to describe the system as follows:
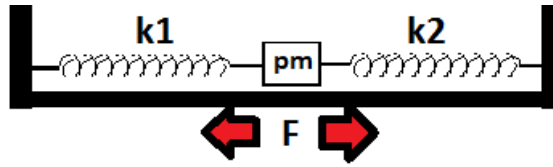
Figure 4-19: Representation of the compression set-up. k1 is the K constant for the FS Force Sensor, pm is the piezo-electric pico-motor and k2 is the K constant of the material that will be measured.

By following the system of Figure 4-19, the general equation for the equivalent K constant of the system, is given by the same equation used for two springs in series described as:

$$K_e = \frac{K_1 \, K_2}{K_1 + K_2} \tag{4.14}$$

Where K_e is the equivalent constant, K_1 is the elastic constant of the force sensor and K_2 is the material constant.

To approach the spring constant for the Force sensor (***compliance***), it is necessary to neglect any material to characterize. A wall with "infinite" spring constant, has to be taken into account (see Figure 4-20).
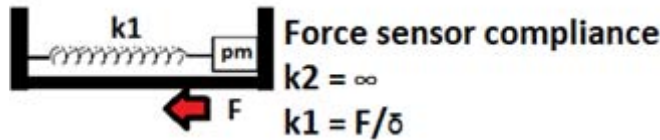
Figure 4-20: Infinite spring constant Wall to analyze the Force Sensor compliance.

Then, by performing several curves limited by a maximum displacement of 5.19 µm, the behavior for the Force/Displacement characteristic curve of the Force Sensor without a material to compress was obtained and is showed on Figure 4-21.
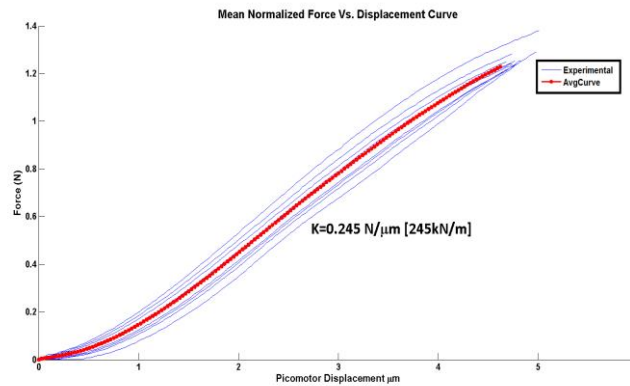
Figure 4-21: Results from compression tests normalized up to a distance of 5.19 µm with a maximum average force of 1.2758 N shown in blue. The average normalized curve is plotted in red giving a K = 245 kN/m for the sensor compliance.

In order to calculate the minimum K that can be measured for the *CCS,* it has to be taken into account the minimum resolution for the force sensor **(F₁min)** which is **1grF (9.81mN),** and the maximum distance that can be performed by the compressor which is δ_{max}= **5.19 μm** whit the actual phototransistor sensor.

If we consider a general equation for total values of force (F_{tot}) and an equivalent constant K_e for a maximum displacement $\delta_{max,}$ of the complete compression set-up is known that:

$$F_{min} = K_{e\ min}\ \delta_{max},\qquad(4.15)$$

$$K_{e\ min} = \frac{F_{min}}{\delta_{max}}$$

Once we have K_1 and K_{emin} it can be calculated K_{2min} from equation (4.14, extracting K_2 giving the next equation:

$$K_{2\ min} = \frac{K_1\ K_{e\ min}}{K_1 - K_{e\ min}}\qquad(4.16)$$

For calculate the maximum $K_{2\ max}$, is known that F_{1max} = 1.276 N, minus the minimum resolution of the sensor F_{1min} in order to do not overcome, the elastic constant of the force sensor for the maximum displacement δ_{max}, giving the next calculations:

$$F_{max} - F_{min} = K_{2\ max}\ \delta_{max},\qquad(4.17)$$

$$K_{2\ max} = \frac{F_{max} - F_{min}}{\delta_{max}},$$

$$K_{e\ max} = \frac{K_1\ K_{2\ max}}{K_1 + K_{2\ max}}$$

Once all the analysis was done, it was noticed that the current rate of displacement was not enough for characterize different materials or the *MESS* proof of concept. Also a small displacement given by a thermal variation on the phototransistor output (see Figure 4-22), has to be taken into account. Several measures to optimize the displacement control were taken into account. On the next section the final displacement adjustments are explained.
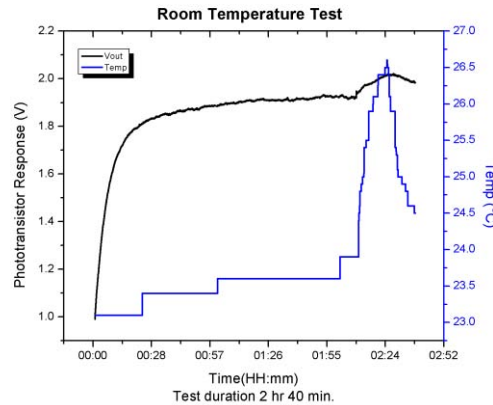
Figure 4-22: Phototransistor variation through time and temperature. At first half hour it is observed a transition behavior which decreases its variation along the next hours. The temperature peak at 02:24 hh:mm, shows a high sensitivity to temperature changes.

4.3.5.1. Final optimization for controlled displacement on CCS

Phototransistor presents temperature and time variations and that is why it was necessary to asses a new option to measure the displacement accurately. A solution which combines the accuracy at small displacements from the optical calibration system with the rotational measurement at large scale of the picomotor screw has been implemented. Our solution to combine both solutions it was to install on the *CCS* a contact-less rotational sensor *AMM20B Multiturn Magnetic Position Sensor*, from the fabricant *Bourns,* which has an analogic voltage outuput that varies accordingly with its rotational position[128]*.* The strategy to merge both solutions was, firstly take the best experimental measurement done with the Optical Calibration System (OCS), for the same displacement of 5 μm, but for different force levels, from 0 to 15N, secondly, the step size variation for compression *(CW)* and de-compression *(CCW)* with the applied force was extracted. Then, two experimental curves were generated based on the same factory step size variation graph showed on Figure 4-8-B. The dependency of the step size variation on the force applied for the *CCS* is observed on Figure 4-23.
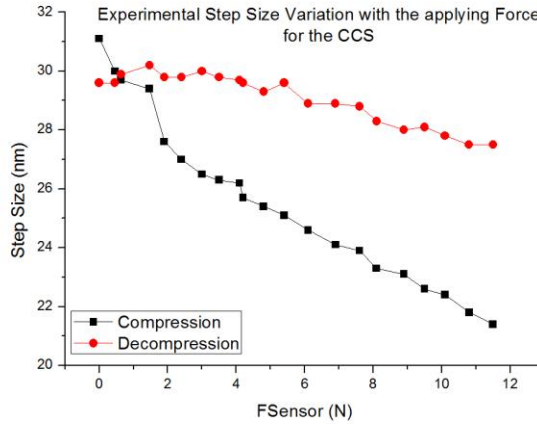
Figure 4-23: The compression (CW) and decompression (CCW) curves for the variation on step size observe don the CCS are shown.

Once these behaviors for compression and decompression direction were obtained, both curves were approximated by a polynomic function. These functions are a direct equivalence between linear displacement and the force applied on the force sensor, and it is independent of the use of the optical calibration system. Therefore, the mounting of the *AMM20B Multiturn Magnetic Position Sensor* can be done without the use of the optical sensor system simoultaneously.

Finally, there are two displacement measurement techniques: the first is based on the step variations functions at compression/decompression with high accuracy, giving a maximum resolution of ≈ 30 nm; the second technique uses directly the output signal from the *AMM20B Multiturn Position Sensor*. This sensor is placed fixed into the eclipse wheel on the *CCS*, to follow the rotational displacement of the picomotor screw which has a maximum displacement rate of 10 revolutions. Its resolution is of 12 bits for 3600° and its output is converted to an analogic signal that has a operation rate from 0 to 5V, then its less significant bit *LSB=1.22 mV*, from the optical calibration system it is known that 1 picomotor revolution (360°) = 317.5 μm then, then, the displacement equivalence for the *AMM20B* sensor is that *0.878° = 0.774 μm*, but once this sensor was used, in practice it was observed that a *0.878° =1.22 μm*, giving a smaller accuracy in compare with the optical calibration system (≈*30 nm*). Then, it was decided to keep both displacement measurements, for small displacements *step decrease equations technique* has higher accuracy, and for large dispalcements it is more realistic and accurate to have the rotational sensor measurement. Comparision of both distance measurement techniques are shown on Figure 4-24.
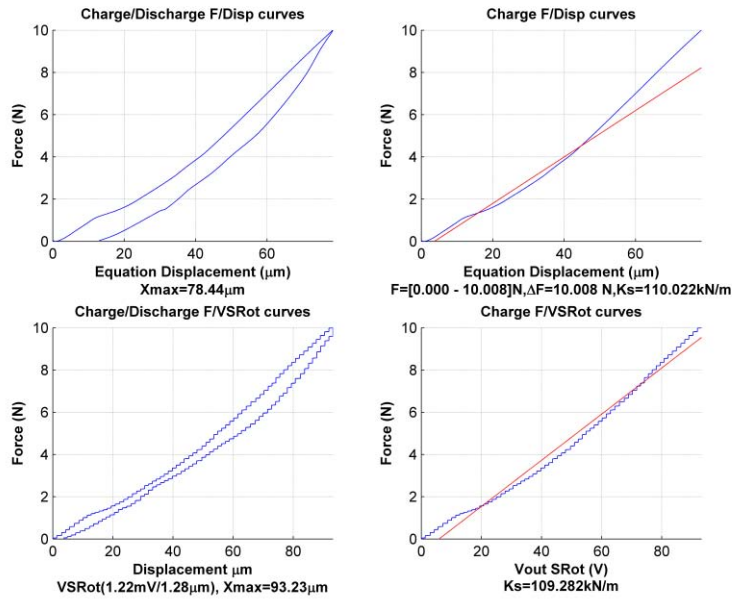
Figure 4-24: Results of Force/Displacement curve on CCS using two displacement techniques. At the top, the step decrease equations and is linear approximation is showed. At the bottom the AMM20B rotation sensor with its linear approximation are shown. The equivalent spring constant of the force sensor calculated is shown at the right hand plots.

Once both techniques were integrated in the *CCS* dedicated software, with this improvement the force sensor is totatlly exploited, to read large and small displacements. In the next section the *IV Sweep* module will be explained.

4.3.6. Moduel 3: IV Sweep

One of the main objectives for the *CCS,* is the integration of an indirect measurement of current during compression tests for the macro-scale *MESS* proof of concept (see Figure 4-4 and Figure 4-5). In order to accomplish this goal, it was necessary the use of a *Low Noise Current Preamplifier Model SR570* from Standfor Research Systems[131].

It is used as a current to tension converter (see Figure 4-25) where, the current (*Ie*) is generated during the voltage sweep as consequence of the internal resistance that the material (load) characterized has. Later, the output current is amplified by a selected factor (K). The output voltage is finally measured by an analogue port on the *DAQ USB-6001.*

$$\left(Ie = IR1; \quad IR1 = \frac{-Vo}{R1}; \quad Ie = \frac{-Vo}{R1} \right) \Rightarrow -Vo = Ie \cdot R1 \Rightarrow Vo = -(Ie \cdot R1) \Rightarrow Vo = Ie \cdot K$$
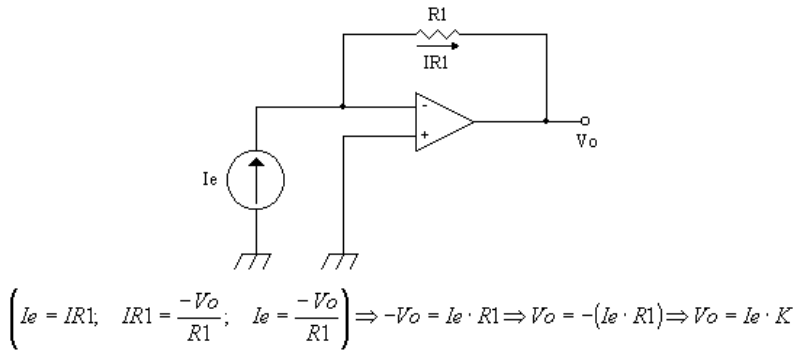
Figure 4-25: Schematic for Current to Tension converter with inverted output.

The current amplifier has a sensitivity of 1pA/V to 1mA/V in a 1-2-5 sequence. It can be controlled through an serial port protocole RS-232, this standard communication protocole, allows the output voltage reading for the dedicated software of the *CCS*.

Update to CCS Software

The rutines that involves the control for the current preamplifier equipment are listed below:

1) *Addhesion of serial port controller:* the curren preamplifier has to be controlled to perform current IV Sweeps during compression tests and, thus, current measurement is needed to be controlled programmatically. Therefore, it was integrated a communication module which reads the RS232 protocol for the equipment.

2) *IV Sweep slope:* once the communication was set, it was necessary to create cycles of VBias sweep variations, in order to create an IV slope, variating the VBias the current behavior can be observed.

3) *Setting the K factor for the Gain:* as part of the GUI it was necessary to control programmatically also the scale on which the *IV* sweeps will be performed.

Testing the IV Sweep

To validate the communication and rutines for the IV Sweep module, a simple IV sweep test was performed on a common resistor of 1 MΩ and, the VBias voltage was swept from -1 to 1 V respectievely. The test was done in 12 different sweeps and, the results from this test are shown on Figure 4-26. Results from this preliminar tests show a percentual deviation of 0.10% from the real value on the resistance. Therefore, the IV measurements have a good accuracy in its general performance to characterize Electro-Mechanical tests on the *MESS* proof of concept. The final *CCS* software platform structure was updated, in order to accomplish with all the tasks described on this chapter, and this final structure is shown on Figure 4-27. It has to be mentioned that, since the Optical Calibration System was characterized through a MATLAB[132] script, and further fittings were necessary to analyze in real time for the experimental behavior of the rotative sensor, it was decided to incorporate a module to communicate with MATLAB scripts saving time on processing data, to later plot results on the*CCS GUI*.
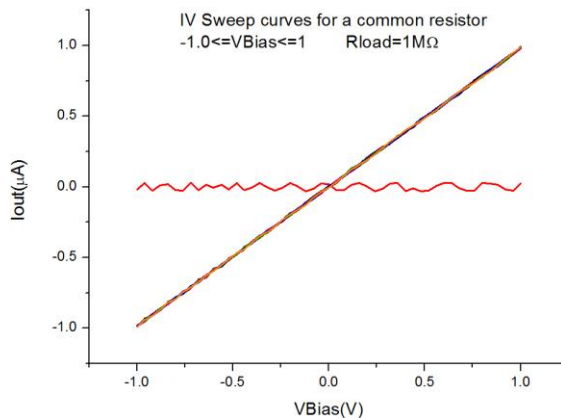
Figure 4-26: 12 IV Sweeps for a common resistor of 1 MΩ. The experimental obtained R=1.017 ±0.001 Ω showed a good agreement with the real value of the resistance.
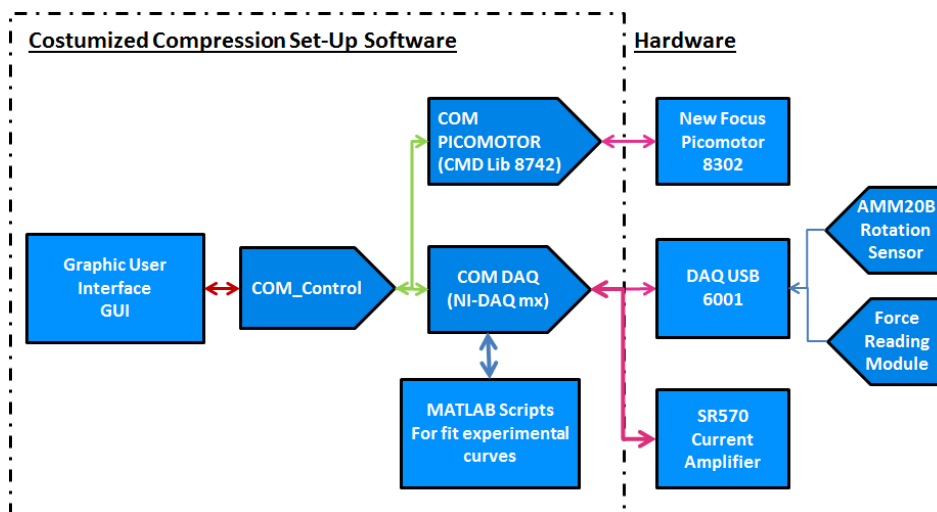
Figure 4-27: Final CCS Software platform showing the incorporation of MATLAB module and the current amplifier.

Technical features of the final CCS assembly

The CCS characteristics are listed as follow:

1) The maximum compression displacement that **CCS** can perform is from 0 to 2.25 cm, with an agreement between the step size equation and the rotative sensor techniques of 82%, with a minimum resolution of 28 ± 2 nm for the step size equation technique and a 1.22 µm for the rotative sensor technique.

2) The maximum compression force rate that the *CCS* can apply is from 0 to 14 N with a minimum resolution of 9.81 mN. The final spring constant for the force sensor, obtained from experimental tests shows a value of ks=174.6 ±14.8 kN/m. It was reduced from the initial spring constant obtained with the OCS due to the fact that the initial maximum compression displacement was of only 5μm.

3) The IV sweeps made by the *CCS* showed a global error on measurements given by the SR570 current amplifier of 0.10 %, with a resolution from 1pA/V to 1mA/V in a 1-2-5 sequence for the amplification, and, finally, the maximum output voltage obtained is of ± 5V, with a slew rate limit of 1 MHz, giving a maximum sample measurement time of 1μsec. per sample that can be measured programmatically from the *CCS* software.

4.4. Summary

In this chapter, it has been described the techniques and equipment that will be used for characterize our *"spring-like"* material. Firstly it was explained the reason to use the Nanoindentation technique, and then the available equipment to perform indentations for the *ZnOfws* was described.

As part of this description it was included a brief description of the most used analysis methods, as is the case of the Oliver and Pharr for a spherical and for a Bercovick indenter's tip.

Later, as a second technique to analyze from a macro-scale point of view the *MESS* behavior, a Costumized Compression Set-Up (*CCS*) was implemented and described in all its fabrication phases.

It was mentioned the main features of the *CCS*, focusing its performance in characterize *MESS* proof of concept which can involves *ZnOfws* or alternative materials. Some issues as the miss-calibration performance for the piezo-electric picomotor used for displacement, has been solved through two different strategies: the first strategy was an *optical calibration system,* and the second one consists in adaptat a *rotation posicion sensor*. These strategies were also described and its combination gave a final implemented *CCS* assemble to perform compressions on different materiales besides *ZnOfws*.

In parallel to the hardware assembly of the *CCS*, it was necessary to develop a software dedicated platform, in order to control and communicate all modules of measurement. The main rutines for operating conditions of each module were explained separately. The final *CCS* platform observed on Figure 4-27, showed the resultant design of all the modules integrated in hardware and software.

In the next chapter the experimental procedure followed to characterize the *"spring-like"* material is described, as a second approach the use of the *CCS* for characterize a *MESS* proof of concept is also described. Results from this characterization are summarized and discussed.

Chapter 5. EXPERIMENTAL RESULTS

I n this chapter the experimental results from characterization techniques are reported. Then, take into account two techniques selected and described on the previous chapter, an experimental methodology was first designed. In this methodology, a description of which properties can be extracted from the material is explained. After define the initial goals from the experimental procedure, each group of results are described separately.

Firstly, the Nanoindentation technique experimental procedure is described, adding observations during the practice for the selected samples. Then, an analysis of the results based on previous characterizations for *ZnOfws* reported on the literature is done.

Secondly, the experimental procedure using the Costumized Compression Set-Up (*CCS*) is described. Due to, the *CCS* is a costumized set-up, the first experimental group of tests, presents a proper validation of the *CCS* measurements with alternative materials, which properties are known. After analyze the validation tests results, a new set of experiments focused on the *MESS* proof of concept is reported.

Finally, results are summarized and discussed for each technique. Once the validation of results is done, the theoretical model described on Chapter 3 is updated and simulated with the experimental results. Afterwards, discussion will be made in the comparison of analytic, simulated and experimental models. Later, taking into account the statistical values of density for each sample characterized, a theoretical analysis of a macro-scale *MESS* is estimated. The results obtained from the scalability approach are compared with the *CCS* experimental results for a *MESS* proof of concept and are discussed deeply.

5.1. Experimental Methodology

This section is dedicated to explain the experimental procedure followed, to perform the different characterizations techniques previously described, which are: Nanoindentation and Compressions tests with a Costumized Compression Set-Up (*CCS).*

Nanoindentation experimental procedure

On the previous chapter at section 4.2, the available equipment for Nanoindentation was described. Then, focused on the geometry of the indenter tip, two groups of experiments were designed. These two groups are described as follow:

Experimental Group 1: Nanoindentation tests with CSIRO UMIS Indenter

This group uses the indenter Ultra Micro Indentation System (UMIS). It has an indenter's tip with flatted cone-shape geometry, with diameter of 14 μm. Based on previous works reported by *M.Riaz et.al* [42], [96], [100], where Nanoindentation technique is used to approach the experimental value for the Young's modulus of *ZnONWs* and *ZnONRs,* and is done based on analyze the last point (see Figure 5-1-Point 1) of the linear behavior on a Load Vs. Displacement curve, resultant of compress simultaneously a certain amount of *ZnONWs* (see Figure 5-1).
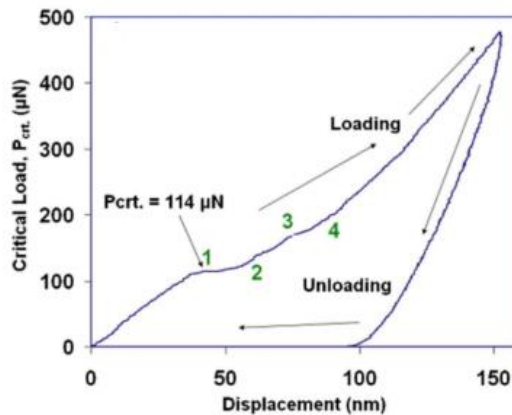
Figure 5-1: Load displacement curve for Nanoindentation applied on ZnONRs/NWs, grown by ACG on Si substrate reported on [96]*.*

Later, this critical load *(Pcrt)* is divided by the number of *ZnONWs* contacted, extracting the individual load for each *ZnONW (Pcrt_unit).* According with the assumption that the region before point 1 at Figure 5-1 is linear, it was reported that by solving the linear elastic theory equations (see Chapter section 3.1) , the critical stress can be calculated as the *ZnONWs* diameters are known. Finally, as the length is also known for the *ZnONWs,* the critical strain, elastic modulus and strain energy can be estimated.

By following the same analysis reported by *M.Riaz et.al* [42], [96], [100], the nanoindentation tests will be performed using the flatten cone-shape tip's indenter. The expected values to obtain are the critical stress, strain, and the Young's Modulus.

Experimental Group 2: Nanoindentation tests with Anton Paar Nanoindentation Tester (TTX-NHT2)

This experimental group uses a diamond four-sided Berckovich indenter tip, rounded with 60 to 90 nm radius, due to the sharp tip, in this experimental group it is expected to obtain the Young's Modulus value of single **ZnONW** tests.

This indenter uses the Oliver&Pharr approach to estimate the material's Young's Modulus. The equations to compute this analysis are a simplification of those expressed on previous chapter at section 4.2, and are summarized in the next equations.

Firstly the experimental reduced Modulus **(Er)** obtained from the Nanoindenter, is defined by equation (5.1):

$$Er = \frac{\sqrt{\pi}S}{2\beta\sqrt{Ap(hp)}} \tag{5.1}$$

β is a yield correction factor equal to **1.034**, appropriated for a Berkovich indenter, **Ap(hp)** is the projected area of the indentation at the contact depth **hp**, and **S** is the stiffness of the contact. This reduced Modulus is related with the plain strain modulus through equation (5.2):

$$E^* = \frac{1}{\frac{1}{Er} - \frac{1 - v_i^2}{Ei}} \tag{5.2}$$

Where **E*** consists in the composite modulus of the system, been **Ei** the Young's Modulus of the indenter equal to **1.41 TPa,** and **vi** is the Poisson's ratio equal to 0.07 for diamond. Finally, the approximation of the estimated Young's modulus of the material is given by the E_{IT} also known as de Indentation Modulus [133],[134] described on equation :

$$E_{IT} = E^*(1 - v_s^2) \tag{5.3}$$

Where v_s the Poisson's ratio of the sample equal to **0.3** in our case as reported on previous works [48], [52], [135].

Finally, all tests performed in this experimental group have as a main goal to indent single **ZnOfws,** obtaining an approach of its Young's Modulus (E_{IT}). As a second approach for those samples where an individual indentation can not be performed, the Young's modulus extraction as a porous bulk will be done.

Costumized Compression Set-Up experimental procedure

For this set of experiments, it has to be mentioned that the **Costumized Compression Set-Up** needs to make validation tests, before using it to measure the macro-scale **MESS** proof of concept. Therefore, the first set of experiments is dedicated to replicate a common **three point flexural test** for different known materials. The parameter that is expected to be extracted from these experiments is the Young's Modulus for the material. Depending on the general deviation from the real values of Young's Modulus, different operating considerations will be taken into account for the second set of experiments. For the second group of experiments, a Silicon bulk will be characterized first, in order to measure, the spring constant of the substrate on which **ZnOfws** are grown, once obtained the

disassociation of the spring constant from **ZnOfws** can be done, extracting only the spring constant for our **ZnOfws**. Finally, the **CCS** will be used to test a macro-scale **MESS** built of SiO$_2$/Polymer optical fiber wires, with the objective of emulate through a material mechanically similar to **ZnOfws**, the linear buckling behavior for different aspect.

On the next section the results from experimental groups will be reported and analyzed.

5.2. Nanoindentation tests

5.2.1. Results from experimental Group 1:

For this set of experiments, it was selected the sample HC100, mentioned on previous chapters. The sample's selection criterion was based on emulate or reach an experimental curve as reported by *M.Riaz.et.al*[42], [96], [100], and also characterize the best aligned perpendicular array found for all the samples. HC 100 accomplish this criterion. First tests of Nanoindentation on sample HC100 were done appling 300 and 500 mN, making an array of indentations. Results are plotted in figures Figure 5-2 and Figure 5-3.
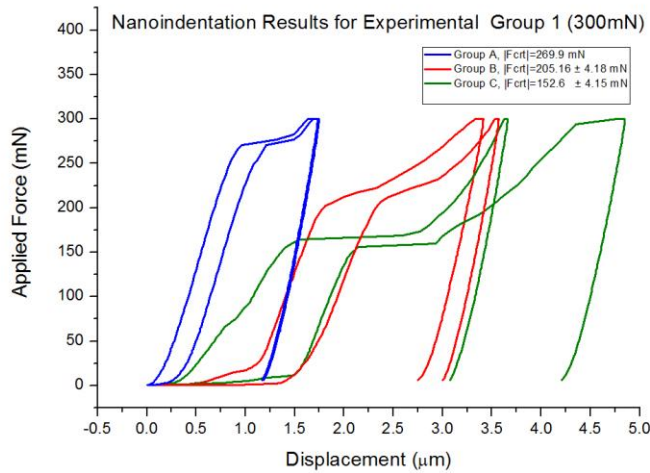
Figure 5-2:Nanoindentation results of Group 1 done on sample HC100 at 300 mN. Indentations were separated in three different groups which match in critical force Fcrt.
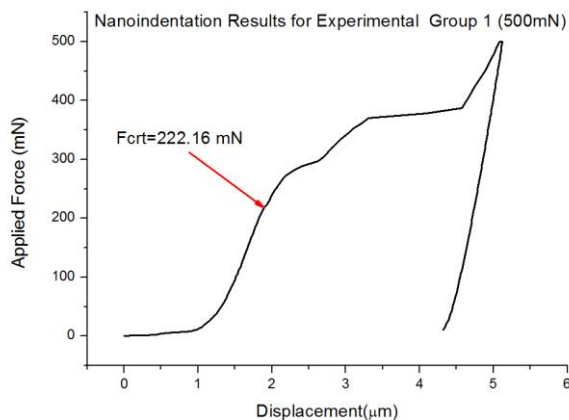
Figure 5-3: Best result from Nanoindentation Group 1 at 500mN on sample HC100. The critical force found is equal to 222.16 mN.

From tests done at *300 mN* three main groups had a good repetitively for a same critical force (see Figure 5-2).The criteria to select the point of the critical load was to take the final point of the linearity observed in the initial behavior. For Groups B and C it was observed a low deviation for the critical force measurement of about *2.37 %,* and for Group A it was less than *1%.*

On the other hand, for tests done at *500 mN* the characteristic curves followed the same response showed on Figure 5-3. Its critical force was found for *Fcrt=221.16 mN* , showing a similar value than that obtained for groups A and B. These results and those obtained on Experimental Group 2 will be discussed on section 5.3 deeply.

5.2.2. Results from Experimental Group 2:

For this set of experiments, two new different characterizations were made. Firstly, for all samples neglected from Group 1, which have the highest growth densities of *ZnOfws (the finewires are very close to each other)*, were characterized as a porous bulk material. The second group of characterizations was based on indent those finewires which aspect/ratio allows performing an individual indentation, with the main goal of extract the Young's Modulus value for a single *ZnOfw*, and update the theoretical model. The selected characterization for each sample is described on Table 5-1.

Sample	Diameter (μm)	Length (μm)	Density (fws/ μm²)	ZnOfws Aspect Ratio (L/D)	Characterization Type
AGM1	0.63 ± 0.19	1.67 ± 0.92	0.68 ± 0.43	2.65 ± 1.4	Individual
AGM2	1.11 ± 0.32	3.73 ± 1.38	0.38 ± 0.14	3.36 ± 0.6	Porous Bulk
GMA	1.26 ± 0.56	7.96 ± 2.2	0.53 ± 0.39	6.32 ± 2.6	Porous Bulk
GMC	0.213 ± 0.067	2.01 ± 0.59	4.18 ± 1.1	9.44 ± 0.44	Porous Bulk

Table 5-1: Characterization Type according with ZnOfw samples.

Previous to all indentations tests, the indentation on a Silicon substrate with the same properties as the growth substrate for the *ZnOfws* samples was done.To verify the accuracy of the equipment, knowing for this material its Young's modulus previously. The second reason for this test, was to have a reference for analyze the contribution of the substrate on the *ZnOfws* measurements. Results from this preliminar tests are shown on Figure 5-4.
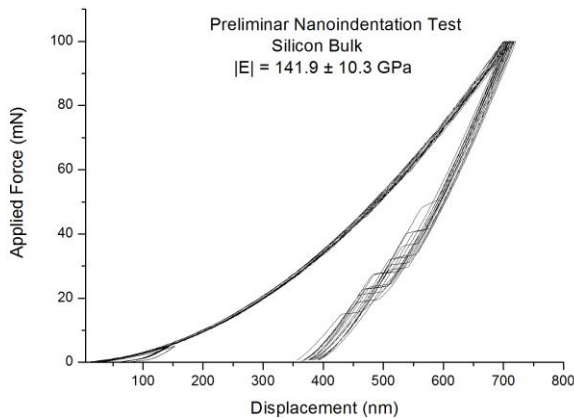
Figure 5-4: Results from preliminar indentation done on Silicon bulk, showing the resultant Young's Modulus estimated by Oliver&Pharr method for the material.

From the results shown on Figure 5-4, it was observed that the corresponding Young's Modulus extracted for Silicon was of ***141.09±10.3 GPa***, which shows a good agreement with the values found on literature for Silicon which varies from ***130.2 to 187.5 GPa*** [136].

The best indentation results for the selected samples shown on Table 5-1 are reported on figures Figure 5-5 to Figure 5-7. It has to be mentioned, that the sample *GMA* was neglected due to, no consistent results were obtained from indentation tests. On the other hand, it was found on sample *AGM1*, three single *ZnOfws*, indented separately. The main observation on these tests, it is the aspect ratio, which is higher than previous reported: for these three *ZnOfws* the diameters and lengths were of 4.3±0.13 and 20.65±0.77 μm respectievely, with a resultant aspect ratio of (L/D)=4.8±0.067 μm. It was also observed a high elastic behavior, showing a good recovery at all tests (see Figure 5-5) .
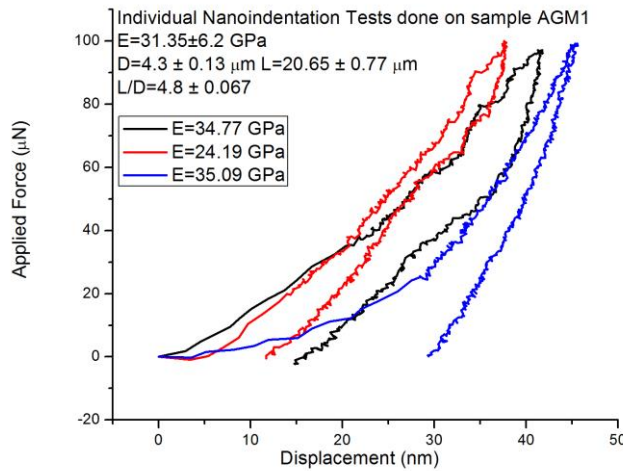
Figure 5-5: Results from individual nanoindentations performed on 3 single ZnOfws, found on sample AGM1.

From sample GMC (see Figure 5-6), it was found a repetitive response once a compression force of ***5mN*** was applied. Then, an average Young's modulus for multiple *ZnOfws* contacted of ***36.1 ± 7.44 GPa*** was obtained. For this sample no merge between *ZnOfws* was observed, instead it was found a homogenous array of *ZnOfws* distributed overall samples's substrate. Therefore, this sample has to be considered as an array instead of a porous bulk on the analysis.

On the other hand for sample *AGM2* it was observed, that *ZnOfws* have a high density and a merging between structures. That is why it was taken as a bulk behavior, rather than an Array. An individual indentation also cannot be performed. For this sample a resultant Young's Modulus of ***65.15±4.8 GPa*** was obtained (see Figure 5-7).
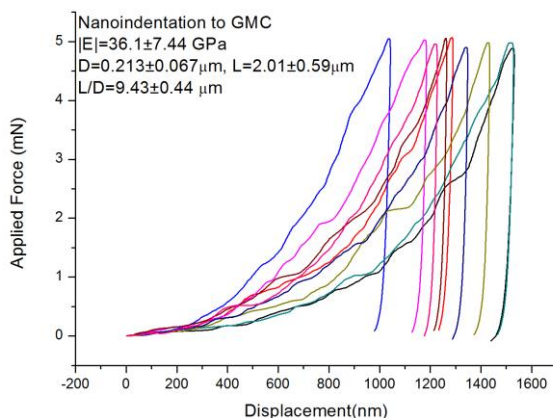
Figure 5-6: Results from indent multiple ZnOfws on sample GMC.
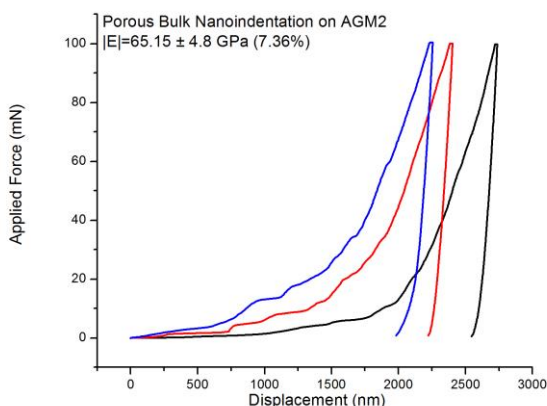
Figure 5-7: Results from nanoindentation made on sample AGM2 treated as a porous bulk material.

From these results it has been observed that samples that were considered as porous bulks a high *ZnO* Young's modulus is obtained, for instance AGM2. For the individivual indentations done at sample AGM1, it was observed an agreement with sample GMC in Young's Modulus values. On the other hand, for this sample in particular it was observed not only the highest aspect ratio (L/D), but also the smallest diameter to been indented individually. Therefore, their mechanical behavior was more closest to a nanowires array (see Figure 5-8).
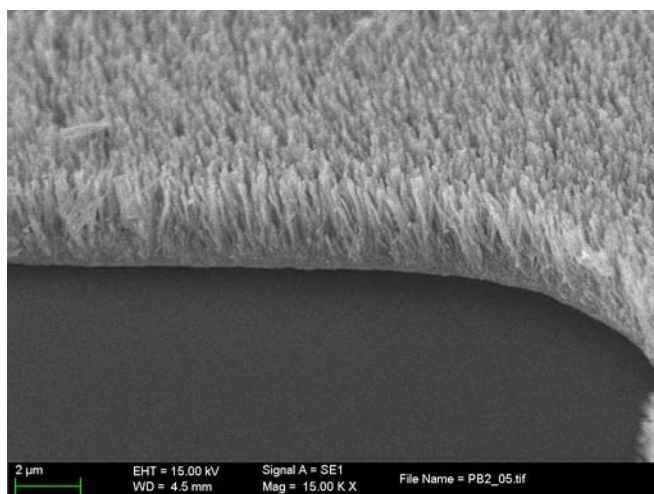
Figure 5-8: SEM 45° tilted image of sample GMC, showing a high perpendicular ZnONWs array.

A deep analysis and discussion of these results is reported on section 5.3.2, taking into account the theoretical model previously reported, FEM simulations and the aspect ratios.

5.3. Discussion of results from Nanoindentation tests

5.3.1.   Experimental Group 1

Firstly, to perform the same analysis planned on section 5.1, SEM observations were done on sample *HC100* (see Figure 5-9), locating the footprints from indentation tip (see Figure 5-10). Once they were located, an update on diameters and the density (fws/μm^2) was done, giving diameters of *1.35±0.33 μm* and a density of *0.21 ± 0.005 fws/μm^2* (see Figure 5-11).
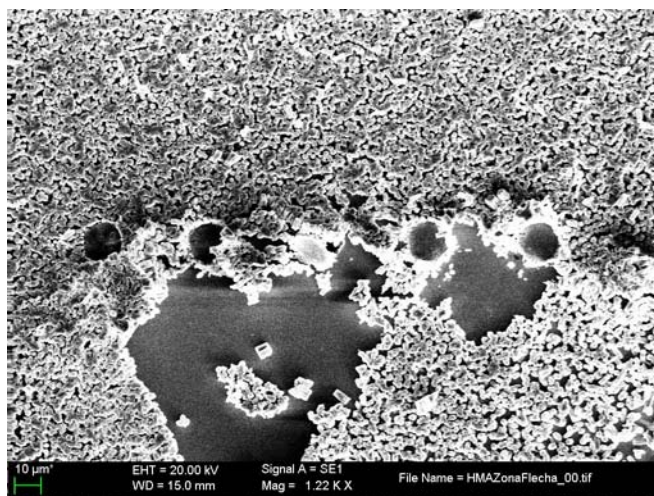
Figure 5-9: SEM image of Nanoindentation footprints for sample HC100.

Once the statistical values were updated through the SEM images analysis, it was estimated a tip's area of **160.38 μm^2** , thus **34.48 ZnOfws** were contacted, during nanoindentation tests. Then, by using this local **ZnOfws** density and the crititcal forces located for each Force vs.Displacement curve, the experimental critical values can be estimated (see Table 5-2).
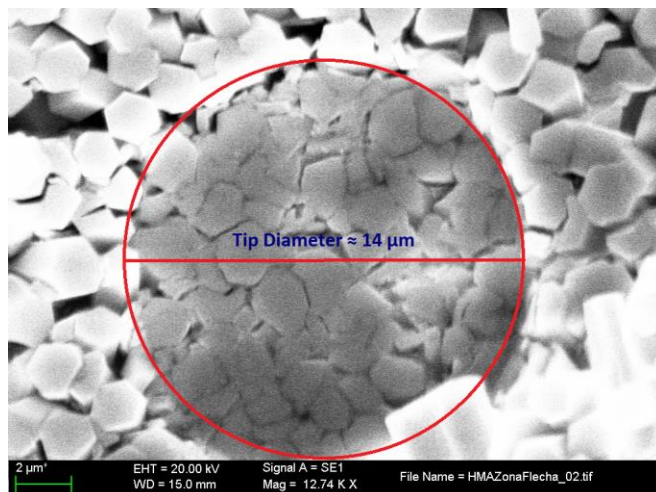
Figure 5-10: SEM close view on a Nanoindentation footprint showing a diameter of 14 µm.
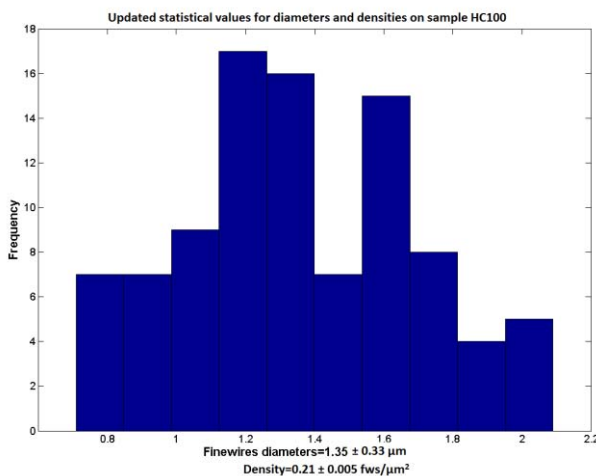
Figure 5-11: Statistical results for ZnOfws diameters and densities on sample HC100.

HC100 D=1.35±0.33 μm L=5.7 ± 0.19 μm 0.21±0.005 fws/μm²	Total Critical Force (mN)	Critical Unitary Force (mN)	Circular Cross-Section Critical Unitary Stress (GPa) A=1.43 μm²	Hexagonal Cross-Section Critical Unitary Stress (GPa) A=1.18 μm²
Group A (300 mN)	269.9	7.82	5.46	6.6
Group B (300 mN)	205.16 ± 4.18	5.95 ± 0.24	4.15 ± 0.33	5.02 ± 1.71
Group C (300 mN)	152.6 ± 4.15	4.42 ± 0.24	3.08 ± 0.33	3.73 ± 1.7
500 mN	222.16	6.44	4.49	5.43

Table 5-2: Experimental estimated critical values for sample HC100, taking updated diameters, densities and experimental critical forces.

It is observed from Table 5-2, that the unitary critical values are higher than expected from the preliminar analysis reported on Chapter 3, with critical stresses from *3.08 to 5.46 GPa*, and critical forces from *4.42 to 7.82 mN*. Moreover, at Figure 5-10, it can be noticed that every indentation footprint left collapsed *ZnOfws*, deforming permanently their structure. Therefore, by taking into account the three original boundary conditions for the *ZnOfws* reported on Chapter 3, their corresponding Young's modulus can be approached.

Results from this analysis showed the best agreement between between analytical and simulated values for the boundary condition of *guided-fixed* (C=0.5), these results are reported on Table 5-3. The general deviation on results can be done by the statistical values approached for the *ZnOfws* dimensions, and also by the error on the measurements.

Circular Cross-Section HC100 D=1.35±0.33 μm L=5.7 ± 0.19 μm 0.21±0.005 fws/μm2	Boundary Condition Constant	Experimental Critical Stress σc(GPa)	FEM Critical Stress σc(GPa)	Exp.Vs.Sim Rel.Err. (%)	Estimated ZnOFws Young's Modulus E(GPa)	Model
Group B (300 mN)	Guided-Fixed	0.5	4.15 ± 0.33	5.8	39.76	62.04 ± 3.79	Johnson
Group C (300 mN)	Guided-Fixed	0.5	3.08 ± 0.33	4.27	38.64	45.1 ± 3.78	Johnson
500 mN	Guided-Fixed	0.5	4.49	6.68	32.78	70.44	Johnson

Table 5-3: Results from estimated Young's Modulus for ZnOfws, showed an average value of E=53.5±11.9 GPa for indentations done at 300 mN, and E=70.44 GPa for 500 mN.

Hexagonal Cross-Section HC100 D=1.35±0.33 μm L=5.7 ± 0.19 μm 0.21±0.005 fws/μm2	Boundary Condition Constant	Experimental Critical Stress σc(GPa)	FEM Critical Stress σc(GPa)	Exp.Vs.Sim Rel.Err. (%)	Estimated ZnOFws Young's Modulus E(GPa)	Model
Group C (300 mN)	Guided-Fixed	0.5	3.73 ± 1.7	5.36	43.69	65.09	Johnson

Table 5-4: Results from estimated Young's Modulus for ZnOfws.

Results obtained at Table 5-3 and Table 5-4, showed that for most of the cases *ZnOfws* appear to behave more as a Johnson column, than an Euler one. It also can be mentioned that the lowest relative error between experimental and simulated values was observed for the *guided-fixed* boundary condition, indicating that *ZnOfws* may not have enough lateral space to move as a *free-fixed* case, this is consistent with SEM observations at Figure 5-10.

Because of the tip's diameter of **14 μm**, covers a flat surface of contacted **ZnOfws**, and donot allow them to have rotational degree of freedom at their top face, a **pinned-fixed** case may not occured. Leaving more **ZnOfws,** which displacement is dependent on the guided displacement that the tip's indenter provides, its deformation can be done through collapse of the **ZnOfws** structure.

FEM simulation and the resolution of the analytical model were done to evaluate agreement between them. Results from this analysis are shown on Table 5-5 and Table 5-6.

Cilyndrical Volume HC100 D=1.35±0.33 μm L=5.7 ± 0.19 μm 0.21±0.005 fws/μm2	Boundary Condition C	Estimated ZnOFws E(GPa)	Critical Stress σc(GPa)	Critical Strain εc(%)	Critical Force Fc(mN)	U (nJ)	MRE Th. Vs. Sim (%)
300 mN	Guided-Fixed	0.5	53.5 ± 11.9	5.02	9.38	7.18	1.92	32.1
500 mN	Guided-Fixed	0.5	70.44	6.61	9.38	9.46	2.53	32.1

Table 5-5: Theoretical vs. FEM simulated results are summarized for a ZnOfw with a cylindrical volume.

Hexagonal Prism HC100 D=1.35±0.33 μm L=5.7 ± 0.19 μm 0.21±0.005 fws/μm2	Boundary Condition C	Estimated ZnOFws E(GPa)	Critical Stress σc(GPa)	Critical Strain εc(%)	Critical Force Fc(mN)	U (nJ)	MRE Th. Vs. Sim (%)
300 mN	Guided-Fixed	0.5	65.09	5.36	8.24	6.35	1.49	28.54

Table 5-6: Theoretical vs. FEM simulated results are summarized for a ZnOfw with a hexagonal volume.

From this experimental group, it was observed a high dispertion between values. This dispertion on results was higher for the boundary conditions of *free-fixed* and *pinned-fixed*. It seems that the **ZnOfws** as an array during indentations tests behave more as a **guided-fixed** structure. Considering the **ZnOfws** with a cylindrical shape, it was observed a smaller dispertion between calculations and experimental Young's Modulus values from **53.15** to **70.44 GPa**. From hexagonal volume approach, it was observed the highest dispersion between values, neglecting the majority of results. Obtaining only for Gorup C a value of **65.09 GPa** for the experimental Young's Modulus, which shows also agreement with the cylindrical volume approach.

In the next section a different analysis will be done, for the experimental group 2, at the end it will be summarized and contrasted the entire experimental **ZnOfws** Young's Modulus approach.

5.3.2.   Experimental Group 2

Results from this group can be organized by aspect ratio, as it is shown on Table 5-7.

Sample	Density (fws/ μm²)	ZnOfws Aspect Ratio (L/D)	Experimental Young's Modulus E(GPa)	Characterization Type
AGM2	0.38 ± 0.14	3.36 ± 0.6	65.15 ± 4.8	Porous Bulk
AGM1	0.051	10.24 ± 0.54	31.35 ± 6.2	Individual
GMC	4.18 ± 1.1	9.44 ± 0.44	36.1 ± 7.44	Porous Bulk

Table 5-7: Summary of Experimental Young's Modulus results for group 2.

From Table 5-7 it can be observed, firstly, that sample AGM1 has changed in aspect ratio, since it was only considered the dimensions found for the ***ZnOfws*** indented, which have diameters of 4.3 ± 0.13 μm and lengths of 20.65 ± 0.77 μm, giving twice the original value on aspect ratio (L/D). A second observation to do, for sample AGM2, is that it was indented more as a porous bulk, due to the high density, without finding ZnOfws with enough lateral space to perform individual indentations. Therefore, a similar behavior of bulk than observed on HC100 is expected.

 Finally, for sample GMC with the highest aspect ratio, it was obtained a similar value of Young's modulus than AGM1, by solving the linear elastic theory according with its slenderness ratio classification, and by simulate its three main boundary conditions. Their mechanical behavior will be updated and studied. The results from this classification are reported from Table 5-8 to Table 5-11.

Circular Cross-section		Boundary Condition C [87]	E Exp. (GPa)	Crt.Strain εc(%)	Crt.Stress (GPa)	Crt.Force (mN)	U (nJ)	Model
AGM2 (L/D) = 3.36 ± 0.6	Free-Fixed	2	65.15 ± 4.8	1.36	0.88	0.86	0.021	Johnson
	Guided-Fixed	0.5	65.15 ± 4.8	8.10	5.27	5.10	0.77	Johnson
	Pinned-Fixed	0.707	65.15 ± 4.8	7	4.56	4.41	0.57	Johnson
AGM1 (L/D) = 10.24 ± 0.54	Free-Fixed	2	31.35 ± 6.2	0.14	0.046	0.14	0.002	Euler
	Guided-Fixed	0.5	31.35 ± 6.2	2.34	0.736	2.33	0.565	Euler
	Pinned-Fixed	0.707	31.35 ± 6.2	1.17	0.368	1.16	0.141	Euler
GMC (L/D) = 9.44 ± 0.44	Free-Fixed	2	36.1 ± 7.44	0.17	0.062	0.002	3.87e-6	Euler
	Guided-Fixed	0.5	36.1 ± 7.44	2.77	1	0.035	9.9e-4	Euler
	Pinned-Fixed	0.707	36.1 ± 7.44	1.38	0.5	0.001	2.4e-4	Euler

Table 5-8: Results from analytical model for circular cross-section on samples from experimental group 2.

Cylindrical Volume Cross-section		Boundary Condition C [87]	E Exp. (GPa)	Crt.Strain εc(%)	Crt.Stress (GPa)	Crt.Force (mN)	U (nJ)	MRE Th.Vs.FEM (%)	Model
AGM2	Free-Fixed	2	65.15 ± 4.8	1.32	0.86	0.83	0.02	3.29	Johnson
	Guided-Fixed	0.5	65.15 ± 4.8	12.52	8.17	7.90	1.84	54.76	Johnson
	Pinned-Fixed	0.707	65.15 ± 4.8	7.6	4.98	4.82	0.68	9.18	Johnson
AGM1	Free-Fixed	2	31.35 ± 6.2	0.14	0.046	0.146	0.002	0.09	Euler
	Guided-Fixed	0.5	31.35 ± 6.2	2.18	0.683	2.16	0.487	7.16	Euler
	Pinned-Fixed	0.707	31.35 ± 6.2	1.13	0.356	1.13	0.132	3.21	Euler
GMC	Free-Fixed	2	36.1 ± 7.44	0.17	0.062	0.002	3.88e-6	0.05	Euler
	Guided-Fixed	0.5	36.1 ± 7.44	2.53	0.915	0.032	8.32e-4	8.42	Euler
	Pinned-Fixed	0.707	36.1 ± 7.44	1.32	0.478	0.017	2.28e-4	4.07	Euler

Table 5-9: Results from FEM simulation compared with analytical for a single ZnOfws with cylindrical volume.

Hexagonal Cross-section		Boundary Condition C [87]	E Exp. (GPa)	Crt.Strain εc(%)	Crt.Stress (GPa)	Crt.Force (mN)	U (nJ)	Model
AGM2 **(L/D) = 3.36 ± 0.6**	**Free-Fixed**	2	65.15 ± 4.8	1.13	0.741	0.59	0.012	Johnson
	Guided-Fixed	0.5	65.15 ± 4.8	18.2	11.86	9.49	3.22	Johnson
	Pinned-Fixed	0.707	65.15 ± 4.8	6.26	4.07	3.26	0.38	Johnson
AGM1 **(L/D) = 10.24 ± 0.54**	**Free-Fixed**	2	31.35 ± 6.2	0.14	0.046	0.14	0.002	Euler
	Guided-Fixed	0.5	31.35 ± 6.2	2.3	0.736	2.33	0.565	Euler
	Pinned-Fixed	0.707	31.35 ± 6.2	1.17	0.368	1.16	0.141	Euler
GMC **(L/D) = 9.44 ± 0.44**	**Free-Fixed**	2	36.1 ± 7.44	0.14	0.052	0.001	2.22e-6	Euler
	Guided-Fixed	0.5	36.1 ± 7.44	2.3	0.833	0.024	5.7e-4	Euler
	Pinned-Fixed	0.707	36.1 ± 7.44	1.15	0.416	0.012	1.42e-4	Euler

Table 5-10: Results from analytical model for hexagonal cross-section on samples from experimental group 2.

Hexagonal Prism Volume Cross-section		Boundary Condition C [87]	E Exp. (GPa)	Crt.Strain εc(%)	Crt.Stress (GPa)	Crt.Force (mN)	U (nJ)	MRE Th.Vs.FEM (%)	Model
AGM2	**Free-Fixed**	2	65.15 ± 4.8	1.10	0.721	0.57	0.011	2.65	Johnson
	Guided-Fixed	0.5	65.15 ± 4.8	11.18	7.28	5.82	1.21	38.59	Johnson
	Pinned-Fixed	0.707	65.15 ± 4.8	6.69	4.35	3.48	0.43	6.83	Johnson
AGM1	**Free-Fixed**	2	31.35 ± 6.2	0.12	0.038	0.122	0.001	16.3	Euler
	Guided-Fixed	0.5	31.35 ± 6.2	1.85	0.580	1.84	0.35	21.2	Euler
	Pinned-Fixed	0.707	31.35 ± 6.2	0.95	0.299	0.95	0.093	18.6	Euler
GMC	**Free-Fixed**	2	36.1 ± 7.44	0.14	0.052	0.001	2.24e-6	0.33	Euler
	Guided-Fixed	0.5	36.1 ± 7.44	2.15	0.779	0.022	4.97e-4	6.53	Euler
	Pinned-Fixed	0.707	36.1 ± 7.44	1.11	0.403	0.011	1.33e-4	3.13	Euler

Table 5-11: Results from FEM simulation compared with analytical for a single ZnOfws with hexagonal prism volume.

From all results obtained on experimental group 2, it can be inferred that the lowest relative discrepancy between theoretical and simulated values was observed for cases of *free-fixed* and *pinned-fixed* boundary conditions. This result was consistent regardless which geometry was simulated (hexagonal or cylindrical).

Taking into account only these two boundary conditions, the lowest relative discrepancy with the highest strain energy value, was observed for the *pinned-fixed* boundary condition, once again for both geometries. This behavior can be explained since the indenter's tip is a four-sided Berckovich indenter tip rounded with a 60 to 90 nm radius, which results in a smaller contact area than the diameters for the *ZnOfws* samples, allowing with this, more a punctual force on the *ZnOfws*, instead of a flat tip surface, as in the case of experimental group 1. Therefore, as it was expected this sharp shape on the tip may allows a rotational degree of freedom that characterizes more a *pinned-fixed* behavior than any other.

Finally, to summarize results from groups 1 and 2, Table 5-12 shows results organized by aspect ratio, with the most probable boundary conditions during indentation tests, the critical force, strain energy and relative error obtained, between theoretical and simulated results, only taken for the hexagonal volume to approach more to real samples.

Sample	ZnOfws Aspect Ratio (L/D)	Exp. YModulus E(GPa)	Most Probable Behavior	Crt.Force Fc(mN)	Strain Energy U(nJ)	MRE Th.vs.FEM (%)	Characterization Type	Model
AGM2	3.36 ± 0.6	65.15 ± 4.8	Pinned-Fixed	3.48	0.43	6.83	Porous Bulk	Johnson
AGM1	10.24 ± 0.54	31.35 ± 6.2	Pinned-Fixed	0.95	0.093	18.6	Individual	Euler
HC100	5.43 ± 0.2	65.09	Guided-Fixed	6.35	1.49	28.54	Array	Johnson
GMC	9.44 ± 0.44	36.1 ± 7.44	Pinned-Fixed	0.011	1.33e-4	3.13	Porous Bulk	Euler

Table 5-12: Summary of best results on experimental groups 1 and 2 for ZnOfws samples with a hexagonal volume.

5.4. Costumized Compression Set-Up tests

Taking into account results obtained from Nanoindentation experiments showed on Table 5-12, the analysis of scalability for a macro-scale *MESS* will be done in this section. Firstly, a preliminar statistical approach will be carried out to analyze which is the required area and force for the *ZnOfws*, for been able to characterize them, more as a macro-scale *MESS* than single finewires.

This approach can be done, by knowing the limits of force that the *CCS* can apply. It has been mentioned that the maximum force applied by the *CCS* is of *14 N*, with a maximum displacement of *2.25 cm.* Then, by using the statistical density calculated for each sample, in combination with the maximum force that can be applied by the *CCS*, the maximum size of the contact area can be approached. Results from this preliminar estimation are reported on Table 5-13.

Sample	Density (fws/ μm2)	Exp. YModulus E(GPa)	Crt.Force Fc(mN)	Strain Energy U(nJ)	Estimated Contacted Finewires (x10³)	Max.Contact Area X10³(μm²)	Estimated Strain Energy U(μJ)
GMC	4.18 ± 1.1	36.1 ± 7.44	0.011	1.33e-4	1272.7	304.47	0.16
AGM1	0.051	31.35 ± 6.2	0.95	0.093	14.73	288.82	1.36
AGM2	0.38 ± 0.14	65.15 ± 4.8	3.48	0.43	4.02	10.58	1.72
HC100	0.28 ± 0.054	65.09	6.35	1.49	2.20	7.87	3.28

Table 5-13: Results from statistical approach of the maximum size of the contacted area, for characterize a macro-scale MESS with the CCS, ordered by their strain energy.

Iit has been observed that the contacted area has micrometric dimensions. It has to be considered two main aspects for the *CCS* tests. The first is to reduce the compression area of the *CCS*, to achieve with the maximum force's resolution a macro-scale measurement of the *MESS*. The second one, is focused on asses the proof of concept for the energy storage principle that we proposed, but evaluating it at macro-scale. In oder to accomplish this, is necessary to find an alternative material, which can behave mechanically similar to the *ZnO*, taking into account also its shape as a fiber or a wire, to make a test of a *MESS* proof of concept.

5.4.1. CCS tests for ZnOfws samples

As it was observed on Table 5-13, the contact area needed for characterize with the *CCS* the *ZnOfws* samples is in the micrometric scale, therefore as a strategy to reduce the current compression area of *3.14 mm²* for the *CCS*, the spherical picomotor head will be used as the compression surface. The main reason is, that as it was observed from Chapter 4, an spherical compression contact area is dependent of the depth or for our case the compression distance h_p and the tip radius R_i. Therefore, the contacted area can vary gradually as a function of the compression distance performed by the *CCS*, this contacted area can be defined by the next equation:

$$A = \pi \, a^2, \tag{5.4}$$

$$a = \sqrt{2R_i h_p - h_p{}^2}$$

Been *a* the radius of the circled contact [116], [117]. Giving these equations, the operating rate for a spherical contacted area provide by the *CCS* can be estimated, giving a maximum

contact area of **19.95 mm²** with a maximum compression distance of **2.52 mm**, and a minimum contact area of **950 μm²** for a minimum compression distance of **60 nm**. Then, using the spherical picomotor tip can be useful to have a wide contact area operation rate, covering all required contact area for all **ZnOfws** samples.

5.4.1.1. Results of CCS validation tests

Once the contact area was approached, before characterize the **ZnOfws** samples, it is necessary to first characterize known materials, in order to asses the **CCS** accuracy, to accomplish this task, the first set of experiments will be done following a regular **3 point flexure test**[137], this test is commonly used to determine the Young's modulus of a material, which has a shape of a beam. The material characterized has to be placed in a two pin supports, later a punctual force is applied in the centre of the beam (see Figure 5-12).

The deflection that is caused by the compression force is defined by the next equation:

$$w_o = \frac{FL^3}{48\,EI} \tag{5.5}$$

Where F is the applied force, L is the length of the material in form of a beam, E is the corresponding Young's Modulus of the material, and I is the second moment of area, which is defined for a rectangular cross-section, with the next expression:

$$I = \frac{wt^3}{12} \tag{5.6}$$

Where w is the width and t the thickness of the beam's cross-section area. By knowing the dimensions and geometry of the beam, and measuring the compression force and displacement, the experimental Young's modulus for the material can be extracted.

3 Point flexure test
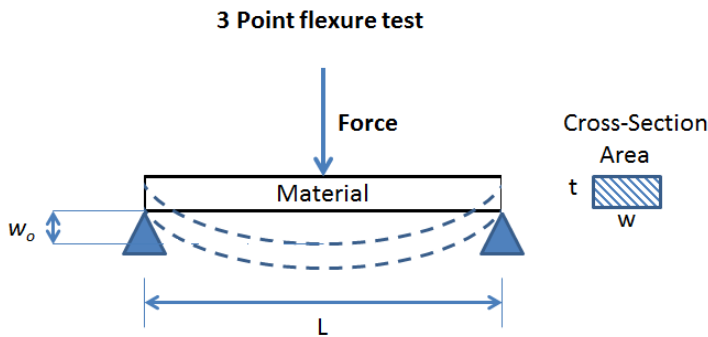
Figure 5-12: General view of a 3 point flexure test.

By substituting equation (5.6 in (5.5, and taking into account the spring constant for the material as Ke=F/w$_o$, the expression for the spring constant on a 3 point flexure test can be defined as follow:

$$Ke = \frac{F}{w_o} = \frac{4Ewt^3}{L^3}$$
(5.7)

Where **Ke** is the equivalent spring constant of the system, which involves the material and force sensor spring constants. Therefore, as it was mentioned in Chapter 4, the material's spring constant (**k2**) has to be disassociated from **Ke**, and this can be done through analyze the **CCS** as a double spring serial system (see Figure 5-13).
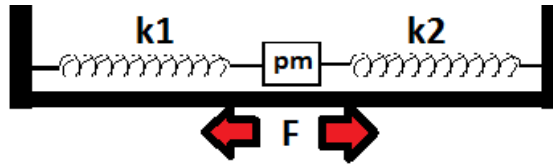
Figure 5-13: Representation of the CCS working principle, where k1 represents the force sensor's spring constant, pm represents the piezo-electric pico-motor, and k2 represents the material's spring constant.

Having in mind, the system described in Figure 5-13 the corresponding equation for the equivalent spring constant is described as follow:

$$K_e = \frac{K_1 \, K_2}{K_1 + K_2}$$
(5.8)

By extracting the material's spring constant (**K$_2$**) from equation (4.14 and substituting on expression (5.7, the Young's modulus for the material (**E$_m$**) can be defined by the next expression:

$$E_m = \frac{K_2 L^3}{4wt^3}$$
(5.9)

Based on this analysis, the characterization of different plastics was done. The results are shown in Table 5-14. All materials has a rectangular beam shape, with **L=28 mm, w= 7 mm**, and thickness of **1** and **3 mm**. For all 3 point flexure tests, the samples were placed on the support, and later were compressed with the spherical picomotor tip (see Figure 5-14). The measurement was carried out first manually, using a micropositioner to control the displacement during the force measurement. Later, the test was repeated, but controlling the displacement automatically with the piezoelectric picomotor (see Figure 5-15).

Material	Ke (kN/m)	Km (kN/m)	Exp. YModulus E(GPa)	YModulus E(GPa)	Rel.Err. (%)
Methacrylate [138]	50.15	69.51	2.01	1.9	5.4
Polycarbonate [139]	3.22	3.27	2.5	2.39	4.4
Acrylic[140]	7.64	7.97	6.2	6	3.2

Table 5-14: Results from 3 point flexure tests on plastics, showing an average relative error 6.5%.
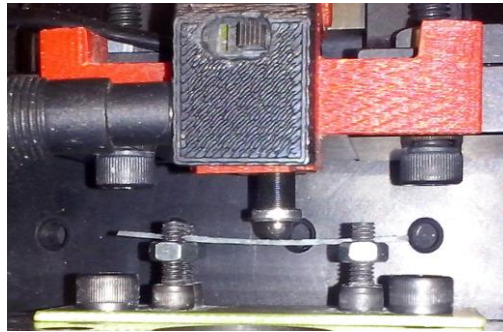
Figure 5-14: Polycarbonate beam placed on CCS for 3 point flexure test. The beam has width of 7 mm, thickness of 1 mm and length of 28 mm.
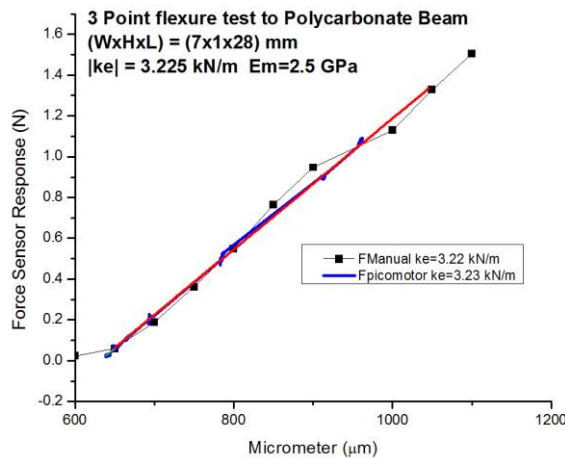
Figure 5-15: Results from 3 point flexure test on a Polycarbonate beam, measuring displacement manually and automatically.

From these results, it was noticed that a deviation of about **5.3%** between results on the same material was observed. This has to be taken into account for the measurements done on the **ZnOfws** samples. Afterwards measure some soft materials, the **CCS** was used to characterize stiffer materials similar to **ZnOfws**, for instance use the same Silicon substrate nanoindented and reported on section 5.2.2, with the main objective of asses the accuracy

that the *CCS* has for small displacement curves, and see if its resolution will be enough for measure the *ZnOfws* samples, with the spherical tip.

Therefore, to continue with the validation of the *CCS* accuracy, a set of compression tests were done on the Silicon substrate, and by knowing on all the tests the compliance of the force sensor denoted by *k1* from equation (5.8), the corresponding material Force Vs. Displacement curve was extracted (see Figure 5-16). In order to validate results, it was used the results from the second experimental group of the Nanoindentation set (see section 5.2.2). From them, the spring constant was approached, by analizing the unload curve in range of 70 to 90% of the maximum Force, as it was mentioned on analysis at Chpater 4 and literature [133],[115], from the selected range of force, a linear fitting can be made to extract the corresponding spring constant as is shown on Figure 5-17.
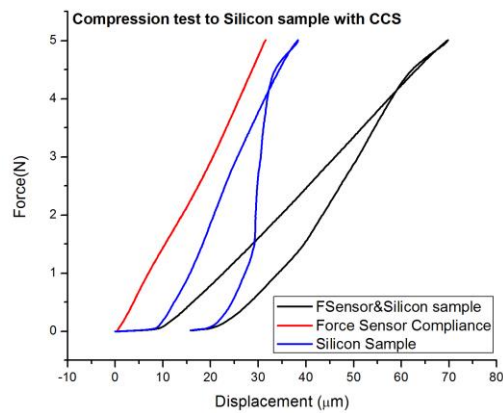
Figure 5-16: Compression test on Silicon substrate, showing the extraction of the material behavior on the blue curve.
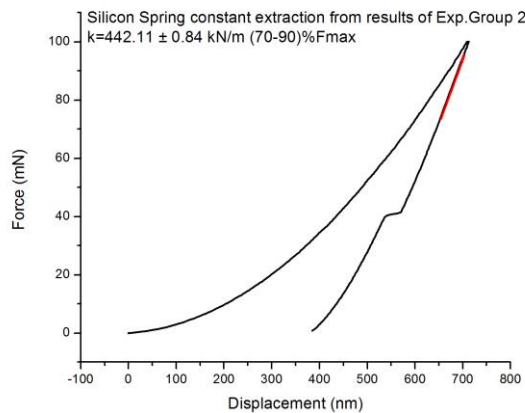
Figure 5-17: Spring constant calculation from Nanoindentation results for Silicon substrate.

Once this analysis was carried out, the corresponding spring constant for the Silicon sample, measured with the **CCS** was approached (see Figure 5-18), from results on Nanoindentation and **CCS** compression tests, it was observed a relative error of **13.24 %** for the best results.
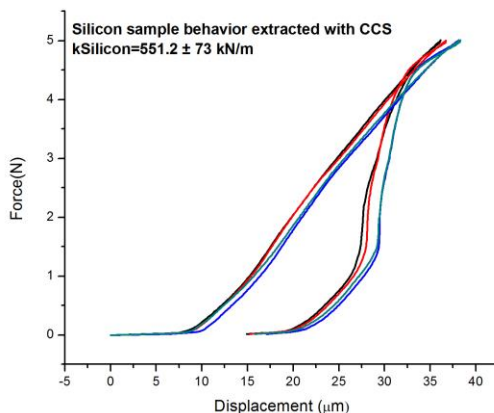
Figure 5-18: Spring constant results for Silicon compression tests with CCS.

From these last validation results, it was clear to observe that the **CCS** showed a higher deviation on compression measurements in compare to those obtained from the **3 point flexure tests**. This can be caused, due to the force sensor's resolution, that works better on larger displacements and relatively softer materials,namely as lower is the spring constant of the material in compare with the force sensor compliance, the better is the measurement obtained.

Another aspect to consider is the variation that keeps appearing on the spring constant compliance of the force sensor, a new calibration was done previous to each measurement, to increase accuracy during materials characterization, nevertheless the variation continues.

Afterwards, taking in consideration the previous observations, the selected samples of **ZnOfws** were measured, one of the best results for sample HC100 is shown in Figure 5-18.
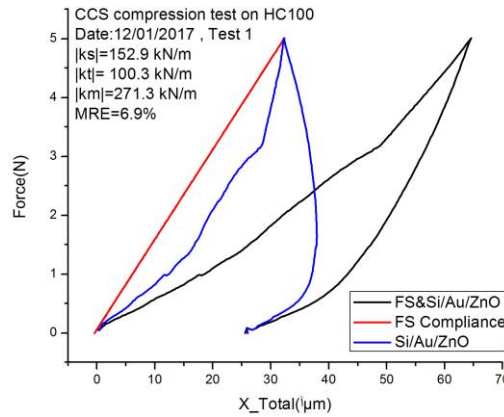
Figure 5-19: Best results from compression tests done with the CCS applied on sample HC100. It is observed a spring constant for the Si/Au/ZnO material, of 271.3 kN/m for an estimated contact area of 0.47 mm².

From all measurements, it was observed for some samples as **HC100** shown in Figure 5-19, that the spring constant obtained for the material, gave a lower value than when Silicon was measured separately, indicating that a different material is involved in the substrate, for our case the **ZnOFws**, for other samples as is the case of **AGM1** and **AGM2**, results showed a spring constant of about **418.7 kN/m**, similar to the Silicon substrate which is of **442.11 kN/m** (see Figure 5-17), indicating that the compressed areas may not include a high density of grown. On the other hand, it has to be mentioned that the **CCS** showed along all the compression tests a high variation on the force sensor compliance, complicating the measurement, for these small distances range.

Finally, it was decided to test a macro-scale material which allow us to characterize buckling from a macroscopic point of view, in the next section the design and objectives to characterize it are explained.

5.4.2.   CCS tests for a macro-scale MESS proof of concept

In this section the approach of a macroscopic proof of concept deomonstrator of a **MESS** will be explained. In order to accomplish this, it has to be considered a material that can be characterized with the **CCS** and at the same time, behave similar to **ZnOfws**. Therefore, special interest was focused on silica optical fibers, specifically the model **SMF-28e** standard optical communication fiber from **Corning** fabricant. The main reason of select this fiber is the similarity that has its Young's Modulus with the **ZnONWs** reported by *M.Riaz et.al*[96], which is of **16.5 ± 0.39 GPa** according to experimental tests reported by *P.Antunes et.al*[141]. A second reason of select optical fibers is due to its flexibility, given due to an acrylate coating. Its average fracture force for these fibers is of **24.60 ± 2.38 N**, also beneficial for our purpose due to these values cannot be reached by the **CCS**. As a third reason to use it, is the

commercial dimensions on which is fabricated, allowing us to costumize the macro-scale *MESS* to the slenderness ratio needed. The diameter for this optical fiber is of *245±5 μm*, the length for each wire can be easily tailored.

Using a similar analysis as the mentioned for calculate values of Table 5-13, an array of Silice fiber wires will be calculated, as the demostrative *"spring-like"* material for characterize the macro-scale *MESS* proof of concept. The calculations were made, taking into account materials *ZnONWs* reported in the literature and *Optical fiber SMF-28e*, with yield strengths of *7GPa* for *ZnONws* [101] and *3.5 GPa* for the optical fiber[142]. Firstly the critical slenderness ratio *λc* was calculated for each material, considering a boundary condition of *guided-fixed*, due to for a macro-scale *MESS* it will be simpler to fabricate and characterize it. Then, once obtained the critical value on which the wires may behave as a Johnson's model column, the slenderness ratio range for fabricate Euler's wires can be obtained (see Table 5-15).

Spring Like Material	Young's Modulus E(GPa)	Critical Slenderness Ratio λc	Min. Wire Length for Euler Model (μm)	Min.Aspect Ratio (L/D)
ZnONW Ref.[96], [100]	16.5	4.82	590	3.41
SMF-28e Ref. [141]	16.5 ± 0.39	6.82	835	2.41

Table 5-15: Analytical results for minimum lengths on wires for a macro-scale MESS.

Once the calculations for the minimum lengths have been done, it can be estimate that the optical fiber wires *(OFWs)* may behave as Euler columns, for lengths larger than *835 μm*, or aspect ratios with larger values than *2.41*.

Later, for the *OFWs* optimal length, it was taken into account the strain energy that can be stored in a single *OFW*, to asses strain energy at different scales, it was proposed *1nJ, 1μJ* and *1mJ*, namely how large does the *OFW* need to be to store these values of energy, and simultaneously it was calculated the critical force needed to achieve these values, the results from this approach is showed on Table 5-16.

Strain Energy U	Critical Force for Buckling Fc(N)	Required OFWs Length L(mm)	Compression distance D(μm)	Maximum OFWs compressed by CCS
1nJ	0.002	200	0.74	4861
1μJ	0.28	20	7.4	48.6
1mJ	28.8	2	74	0

Table 5-16: Analytical estimations for the optimal length of the OFWs array.

From Table 5-16, it can be observed that a length with value of *2 mm*, can reach a critical force of *28.8 N*, higher than the maximum resolution for the *CCS (14 N)*, besides this value of force is larger than the one reported for the fracture of the optical fiber, meaning use a length with this values could be of high risk for the material. For a length of *200 mm*, the

installation of a *MESS*, fabricated with these wires will be a problem. Due to, the limit of space that the *CCS* has for characterize materials is no longer than *100 mm.* Therefore, characterize a *MESS* with this dimensions will be not possible with the *CCS*. Finally the best length for the *OFWs* is of *20 mm*, which has a compression force for buckling of *280 mN*, allowing the compression of *48.6 OFWs* simultaneously, within the force resolution of the *CCS*. The compression distance for buckle the *OFWs*, is estimated at *7.4 μm* which is a value also in the operating displacement tolerances of the *CCS*.

Finally for the *OFWs* array size, it is known that the limit of *OFWs* that can be characterized by the *CCS* is of *48.6* for a maximum force measurement of *14 N*, and then by taking a symmetrical square array, the maximum size will be of *7 x 7*. On the other hand, evenethough the macro-scale *MESS proof of concept* has as a main goal the experimental analysis of the linear buckling, the *CCS* allow us to also analyze the pre and post buckling too, for this purpose if the original calculated array is reduced from *7x7* to *6x6 OFWs* the estimated maximum force to reach the linear buckling point will be of *10.08 N*, leaving a *4N* rank to analyze any postbuckling behavior on the *OFWs.* Finally, the *6x6 OFWs MESS proof of concept* assembled, is shown on Figure 5-20.

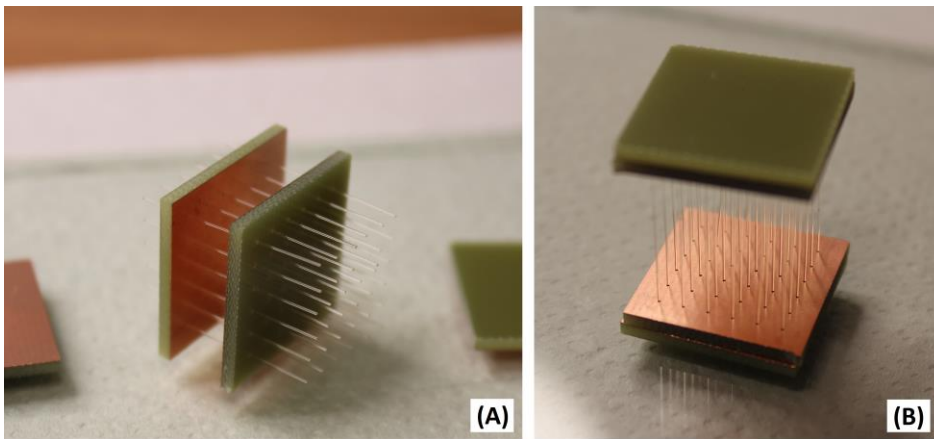*Figure 5-20: Macro scale MESS proof of concept. (A) Optical fibers wires 6x6 array. (B) Final assembly of the OFWs MESS proof of concept.*

For the final assembly of the *MESS proof of concept* observed on Figure 5-20 ,it was used as a support material pcb layers, with the purpose of keep aligned and stable the *OFWs*. Later, the macro-scale *MESS proof of concept* was placed on a support for been characterized by the *CCS*.

5.5. Summary

In this chapter all the experimental methodology was described in detail. The mechanical characterization for the **"spring-like"** material was the main objective for all the set of compression tests. Mechanical characterization was carried out by two main strategies. The first strategy was based in the Nanoindentation technique, by taking previous works done to characterize **ZnONWs**. Thus, it was carried out the same analysis looking for the Young's Modulus of the **ZnOFWs**, in order to update with more realistic values our analytical model.

From this analysis, it was observed that the boundary conditions selected appear for different circumstances. Namely for the experimental group 1, where the **ZnOFWs** were indented as an array of finewires for sample **HC100**, a less value of the relative error was observed for the boundary condition **guided-fixed**. One reason for these results is related with the compression contact area, given by a flat conycal diamond tip, which was considered flat and wide with a diameter of **14 μm**, by having this flat surface for the compression, the **ZnOFWs** do not have freedom to rotate as is the case of the **pinned-fixed** boundary condition, another reason is the high densitiy found for this sample, which also affect a **free-fixed** behavior due to the small space between each **ZnOFW**. Results from this first experimental group showed values of Young's Modulus for the **ZnOFWs** of **53.15 to 70.44 GPa**. The second set of experiments for the Nanoindentation technique was dedicated in find, the porous bulk or single **ZnOFw** Young's Modulus. Therefore, to accomplish this objective it was used a four-sided Berckovich indenter tip, rounded with 60 to 90 nm radius. In this nanoindentantion experiments, it was observed a smaller relative error between calculations for the **pinned-fixed** boundary condition. The main reason inferred for these results, was once again the indenter tip, which for one case was sharped enough to make individual indentations, for instance on the sample **AGM1**. This was only possible if the tip diameter was smaller than the **ZnOFW** diameter. For the rest of samples **AGM2, GMC** the analysis was done, by taking them as a porous bulk, due to their diameters and densities were not suitable for individual or array characterization.

From the second set of Nanoindentation experiments values of Young's Modulus of **31.35, 36.1 and 65.1 GPa**, with an average relative error of **13.3%**, were obtained.

Finally, for the last characterization it was used the **Compresssion Costumized Set-up**, which had as a main goal the mechanical characterization of a larger **ZnOFws** contacted area. Namely, instead of evaluate invidually or by a small compression areas the **"spring-like"** material, it was observed more as a **MESS**, compressing a higher rate of **ZnOFws.** In order to accomplish this, the first set of experiments was dedicated to evaluate at macro-scale the **CCS** accuracy. Therefore, it was purposed a set of experiments based on the **3 point flexure test**, for characterize known materials as soft plastics (Methacrylate,

Polycarbonate and Acrylic). Results from characterize these selected materials gave an average relative error of *5%*. After this first approach the *CCS* accuracy was put in test for small displacements, and harder materials, this time more related with the *MESS* behavior, therefore the same Silicon sample characterized by the nanoindentation technique was used. The first observation from this test was the consistent deviation of the compliance Force Sensor during the compressions. This causes a clear increase of the relative error between measurements. Nevertheless, the spring constant for the Silicon sample obtained was of *551.2 ± 73 kN/m.* The relative error found was of *13.24%* in comparison with the Nanoindenter results.

After these previous results, the same selected *ZnOFws* were characterized with the *CCS*, it was observed the same issue for the force sensor compliance, giving poor accuracy during compressions in general for small distance compresions. From the best results obtained, the sample *HC100* showed a smaller spring constant of about *273.1 kN/m*, which represents the interface of Silicon,Gold and ZnO.

Once it has been described the experimental procedure, to asses the viability of fabricate a *MESS* that uses *ZnOFws* as its *spring-like* material, in the next chapter a global summary of the results obtained and future works will be done.

Chapter 6.   CONCLUSIONS AND FUTURE WORKS

I n this chapter the global summary of this thesis is reported, listing the different objectives accomplished as part of each phase of development for analyze the viability of fabrication, for a *Mechanical Energy Storage System (MESS)*. Afterwards, the general conclusion of the viability for use the *ZnOfws* as *"spring-like"* material to store strain energy is explained. Later, as part of this summary, the future works on which the research can be continued are listed.

6.1. Conclusions

The main objective of this thesis consists in the characterization of *ZnO* as a potential material to store mechanical energy, for the conceptual design of a *MESS*. In order to asses this material, the research was separated in 4 different phases of development. The most important results from each phase are described by the following conclusions:

Phase 1: Synthesis and optimization of HTM fabrication process for ZnOfws

After the HTM was optimized with a *ZnO* layer deposition method, perpendicular arrays of hexagonal *ZnOfws* were obtained, with different densities and dimensions. The main advantage of the layer deposition observed, was the high perpendicularity of the structures, and also it was observed that the use of a gold surface as catalyst was not anymore needed. From the best results, 5 samples were selected for further characterization (*HC100, AGM1, AGM2, GMA, GMC*), based on its observed perpendicularity, hexagonal shape and high density.

Phase 2: Statistical analysis of the best results

Once the samples were selected, a statistical model to estimate the dimensions of the *ZnOfws* was used through the analysis of SEM images. From this statistical model the estimated dimensions for these *ZnOfws* samples, were from *0.213 to 1.26 µm* for diameters and *1.67 to 7.96 µm* for lengths. On the other hand the estimated densities oscilates from *0.28 to 4.18 ZnOfws/µm²*.

Phase 3: Theoretical model and FEM simulations for Mechancial Analysis on ZnOfws

Afterwards the statistical dimensions were obtained for the selected samples. The linear elastic theory was used, to estimate the mechanical behavior of a single *ZnOfw*, analyzing it as a simple column submitted to axial compression. The analysisis was carried out first by the classification of the *ZnOfws* by its slenderness ratio. Obtaining its theoretical model that will be more accurate between *Johnson's* or *Euler's* model. Then, the critical values were calculated for its linear buckling point, considering experimental values of Young's

modulus found on the literature from nanoindentation tests done for **ZnONWs**. From the analytical results it was observed that the samples **AGM1** and **AGM2**, showed the highest trend to behave as short columns which follow more the Johnson's model, and can reach a stain energy rates from **152 to 408.2 pJ**, for a hexagonal shape on the **ZnOfw**. On the other hand, for long columns which follow the Euler's model, the best results were found for the sample **GMC**, with maximum strain energy of **0.13 pJ**. And finally for intermediate columns as sample **HC100**, the maximum strain energy reach a value of **81.96 pJ.**

Phase 4: Mechanical characterization for the best samples of ZnOfws

The mechanical characterization was carried out by two different strategies which are: *Nanoindentation technique and the Costumized Compression Set-Up (CCS) compression tests.*

Conclusions for Nanoindentation technique

For the first strategy the nanoindentation technique was used, for characterize mechanically the **ZnOfws**, extracting as a main parameter the Young's Modulus of the material. The results from this strategy were separated in two different experimental groups. The first group has as main objective the extraction of the Young's Modulus for a **ZnOfws** array, which is compressed by tip's area of **160.38 μm^2** that contact **34.48 ZnOfws** for the selected sample **HC100**. From the results, it was found the lowest relative error between experimental and theoretical calculations for the **guided-fixed** boundary condition, showing values of Young's Modulus from **53.15 to 70.44 GPa**.

The second group has as main objective, extract the Young's Modulus for individual **ZnOfws**, and for those samples where individual indentation was not possible, the Young's Modulus value was extracted considering the samples as a porous bulk material. The individual indentations can be done due to the second equipment of nanoindentation used, which had a **30 to 60 nm** radius Bercovich sharp tip, allowing indentations for a single **ZnOfw**, as it was the case of the sample **AGM1,** where the structures had diameters of **4.3 ± 0.13 μm.** The results of individual indentations showed an average Young's Modulus of **31.35 ± 6.2 GPa**. For other samples as the case of **GMC**, due to the **ZnOfws** were the smallest in diameters, no individual indentations could be done, leaving the analysis more as a porous bulk, obtaining a Young's Modulus of **36.1 ± 7.44 GPa**.

The results obtained for the second experimental group, showed the lowest relative error between experimental and theoretical values, for the boundary condition **pinned-fixed** and **free-fixed**. From these, the highest level of strain energy reported was for the **pinned-fixed** boundary condition. This behavior was inferred to have a relation with the tip's surface, which is sharp enough for allow a rotation freedom degree and also with the density for some samples, where the lateral space was large enough for allow on the **ZnOfws** lateral displacement. This behavior would not occur on a flat surface indentation on a sample with high growth density, like observed on the firs experimental group for sample **HC100**.

For all nanoindentation tests, the analytical and FEM simulation process were updated using the experimental values of Young's modulus obtained. Later, the extraction of the realistic critical values for the linear buckling on the **ZnOfws** was done. From the best results, the highest strain energy was found for the sample **AGM1** with a value of **5.61 ± 0.82 nJ**, and the lowest strain energy for the sample **GMC** with **1.33 e-4 ± 3e-6 nJ**.

Both strain energy levels were found for a *pinned-fixed* boundary condition, and taking into account a hexagonal prism volume for the *ZnOfws.*

Conclusions for Costumized Compression Set-up compression tests

This set of compression experiments, were focused in the characterization of the material at a larger scale, taking into account a larger contact area for the compression of multiple *ZnOfws* simultaneously, emulating more the behavior expected for a Mechanical Energy Storage System *(MESS)*. This characterization was carried out first by analyzing the accuracy for the *CCS.* Therefore, a set of experiments based on a *3 point flexure test* was firstly done. The characterization was done for macro-scale beams made of relatively soft plastics (Methacrylate, Polycarbonate and Acrylic). Results from these experiments extract the Young's Modulus for the materials. They showed an average error between experimental values and literature values of about *5%*. Later, once it was observed that the *CCS* has a good accuracy for large displacements, a second set of validation experiments were done for compress a *Silicon* sample, this time the relative error was increased up to a *13.24 %*. It was also observed that the force sensor shows a variation on its compliance, for small displacments. Giving at the end a high variation between each measured, forcing to calibrate its resolution every time before any measurement.

Eventhough this lack of accuracy was observed for small displacements, the compression tests for the selected samples (*HC100, AGM1, AGM2, GMA, GMC*) were done. From results it was observed two main behaviors. Firstly for samples *AGM1* and *AGM2*, the spring constant extracted appear to be similar to Silicon substrate, without showing any change caused by the *ZnOfws* grown on the surface. Secondly, for the sample *HC100* it was observed a clear reduction in the spring constant showing a value of *273.1 kN/m* in compare with the Silicon substrate which has a spring constant of *551.2 ±73 kN/m*, it was inferred that the cause for this spring constant reduction, is given by the stiffness of the *ZnOfws* measured, which is behaving as a spring in serie with the Silicon. It has to be mentioned that for this set of experiments, the variation on the compliance for the force sensor was repetitive, and complicates the interpretation of the measurements in general. Therefore, consistent conclusions from these set of experiments can not be done accurately. New strategies have to be considered in the future to measure with the *CCS* equipment under small scales of displacement.

From the mechanical characterization it was observed that the aspect ratio has a relation with the amount of strain energy stored, namely for the lowest values of aspect ratio which corresponds to samples *AGM2* and *HC100* the highest levels of strain energy were found for a boundary condition of *pinned-fixed* with values between *0.43 to 1.49 nJ*. On the other hand for samples with the highest values of aspect ratios, which is the case of samples *AGM1* and *GMC* the strain energy reaches values from *1.33 e-4 to 0.093 nJ,* then it was shown that as higher is the aspect ratio the less strain energy can be stored. It was also observed that the highest levels of energy correspond more to those *ZnOfws* whose follow the *Johnson's model,* than the slender *ZnOfws* which follow the *Euler's model,* the main drawback of this is that the buckling that occurs for these columns, will not be necessary linear as it was explained on Chapter 3, and this may become unstable the load/unload cycles for a *MESS.*

On the other hand, for those samples which follow the *Euler's model,* eventhough the smallest amount of strain energy were obtained, its main advantages are that they can reach its buckling point with a smaller amount of required compression force, and their behavior on the buckling point may be more linear and stable during the load/unload cycle. Then, a balance between the required force to buckle the *ZnOfws,* and the growth density has to be done, in order to develop an efficient *MESS*.

It was concluded, that the main advantage of use a *"spring-like"* material as the *ZnOfws*, instead of an alterantive, is the tailoring that can be done for a specific amount of available energy to harvest. It is clear that control the *ZnOfws* dimensions and density is hard by using the HTM, but it has been demonstrated that through this simple method an by varing parameters during the aqueous bath, give a variability that if is well controlled can be useful to produce *ZnOfws* of specific dimensions and densities.

Once all these observations were done, it has to be mentioned that to asses properly the viability of design and fabricate a *MESS* that uses as *"spring-like"* material an array of *ZnOfws*, it is still necessary to extend the study for analyze more *ZnOfws* properties that still unknown for this thesis. Therefore, in the next section some of these activities are described.

6.2. Future works

Different works can be done to continue with the characterization of the *ZnOfws*, for instance it was briefly mentioned on chapter 4, the use of the semiconductive properties from the *ZnO*, to measure undirectly the quantity of deformation that the *ZnOfws* are having during a compression. This experimental procedure can be also extended to analyze the piezoelectric behavior for the *ZnOfws*, which was not exploited for this thesis. In order to verify if is viable the conversion from mechanical to electrical energy on a *MESS*, analyzing the energy losses that may occur during the conversion.

Another activity that could be done is the study of the dissipation factor for the *ZnOfws,* the main objective for this study is to analyze the energy losses that are dissipated in form of heat during the compression. Therefore, if the dissipation factor is known, the efficiency estimation can be done for the *MESS* performance.

Looking forward for the mechanical limits of the *ZnOfws* as columns, studies of nanoindentation can be done focused on study the fracture limit for the *ZnOfws,* and also extend this study to analyze the fatigue strength, these studies can be useful to analyze the *MESS* performance as a mechanical battery that can be submitted to a finite number of charge/discharge cycles, and also estimate the reliability for the overall system.

Finally, thinking at a macro-scale the study on fibers can be continued to analyze different materials that behave similar to *ZnOfws*, besides the Optical Fiber, and searching to match also with the *ZnO* piezo-electric property, in order to asses the *MESS* performance deeply in the macro-scale.

Author contributions

6.2.1. Publications

- **O.G.Súchil**, G.Abadal, F.Torres, "Effect of temperature and pH level on the hydrothermal growth of ZnO finewires", Nanoenergy Letters, no.5, pp.12-14, 2013.

- **O.G.Súchil**, G.Abadal, F.Torres, "Storing Deformation Energy of ZnO finewires in a Mechanical Battery", Journal of Physics: Conference Series 557 (2014) 012043, Power MEMS 2014.

- **O.G.Súchil**, G.Abadal, F.Torres, "Storing Energy in the Mechanical Domain", Conference Manuscript for the Mechanical Research Society (MRS), Spring Meeting & Exhibit, 2014.

- **O.G.Súchil,** G.Abadal,F.Torres, "A mechanical battery based on an array of ZnO finewires grown vertically by hydrothermal method", submission Applied Physics Letters, APL17-AR-02993,2017.

6.2.2. Conference Contributions

- **O.G.Súchil**, G.Abadal and F.Torres,"Storing Deformation Energy of ZnO finewires in a Mechanical Battery", Power MEMS, November 18,2014, Awaji Island, Hyogo, Japan.(Poster)

- **O.G.Súchil**, G.Abadal and F.Torres, "Storing Deformation Energy of ZnO finewires in a Mechanical Battery",Energy Challenges and Mechanics (ECM), August 11,2015, Aberdeen, Scotland, UK.

References

[1]   H. Ibrahim, A. Ilinca, and J. Perron, "Energy storage systems-Characteristics and comparisons," *Renew. Sustain. Energy Rev.*, vol. 12, pp. 1221–1250, 2008.

[2]   A. Dekka, R. Ghaffari, B. Venkatesh, and Bin Wu, "A survey on energy storage technologies in power systems," *2015 IEEE Electr. Power Energy Conf.*, pp. 105–111, 2015.

[3]   V. Das, S. Padmanaban, K. Venkitusamy, R. Selvamuthukumaran, F. Blaabjerg, and P. Siano, "Recent advances and challenges of fuel cell based power system architectures and control – A review," *Renew. Sustain. Energy Rev.*, vol. 73, no. November 2016, pp. 10–18, 2017.

[4]   A. Leo, "Stationary Fuel Cell Power Systems with Direct FuelCell Technology Tackle Growing Distributed Baseload Power Challenge."

[5]   J. I. San Martin, I. Zamora, J. J. San Martín, V. Aperribay, and P. Eguía, "Energy storage technologies for electric applications," *Int. Conf. Renew. Energies Power Qual.*, no. 2, pp. 1–6, 2013.

[6]   A. Kundu, J. H. Jang, J. H. Gil, C. R. Jung, H. R. Lee, S. H. Kim, B. Ku, and Y. S. Oh, "Micro-fuel cells-Current development and applications," *J. Power Sources*, vol. 170, no. 1, pp. 67–78, 2007.

[7]   "Ultracell." [Online]. Available: www.ultracellpower.com.

[8]   "Angstrompower." [Online]. Available: http://www.angstrompower.com.

[9]   "Commsdesign." [Online]. Available: http://www.commsdesign.com.

[10]   "Neasia." [Online]. Available: http://neasia.nikkeibp.com.

[11]   A. Tyagi, K. M. Tripathi, and R. K. Gupta, "Recent progress in micro-scale energy storage devices and future aspects," *J. Mater. Chem. A*, vol. 3, no. 45, pp. 22507–22541, 2015.

[12]   E. Zhang and Y. Ni, "3D reticulate $Co_x Ni_{3-x} S_2$ nanostructure on nickel foam as a new type of electroactive material for high-performance supercapacitors," *RSC Adv.*, vol. 6, no. 108, pp. 106465–106472, 2016.

[13]   A. S. . b Westover, D. . Freudiger, Z. S. . Gani, K. . b Share, L. . b Oakes, R. E. . Carter, and C. L. . b Pint, "On-chip high power porous silicon lithium ion batteries with stable capacity over 10000 cycles," *Nanoscale*, vol. 7, no. 1, pp. 98–103, 2015.

[14]   P. E. Delannoy, B. Riou, T. Brousse, J. Le Bideau, D. Guyomard, and B. Lestriez, "Ink-jet printed porous composite LiFePO<inf>4</inf> electrode from aqueous suspension for microbatteries," *J. Power Sources*, vol. 287, pp. 261–268, 2015.

[15]   H. Ji, Y. Mei, and O. G. Schmidt, "Swiss roll nanomembranes with controlled proton diffusion as redox micro-supercapacitors," *Chem. Commun.*, vol. 46, no. 22, p. 3881,

2010.

[16]   K. Wang, W. Zou, B. Quan, A. Yu, H. Wu, P. Jiang, and Z. Wei, "An all-solid-state flexible micro-supercapacitor on a chip," *Adv. Energy Mater.*, vol. 1, no. 6, pp. 1068–1072, 2011.

[17]   S. Wang, N. Liu, J. Tao, C. Yang, W. Liu, Y. Shi, Y. Wang, J. Su, L. Li, and Y. Gao, "Inkjet printing of conductive patterns and supercapacitors using a multi-walled carbon nanotube/Ag nanoparticle based ink," *J. Mater. Chem. A*, vol. 3, no. 5, pp. 2407–2413, 2015.

[18]   S. Liu, J. Xie, H. Li, Y. Wang, H. Y. Yang, T. Zhu, S. Zhang, G. Cao, and X. Zhao, "Nitrogen-doped reduced graphene oxide for high-performance flexible all-solid-state micro-supercapacitors," *J. Mater. Chem. A*, vol. 2, no. 42, pp. 18125–18131, 2014.

[19]   X.-F. Tang, Z.-G. Yang, and J.-H. Liang, "Synthesis of a ternary FeNi $_2$ S $_4$ /CNT/graphene nanocomposite with improved electrochemical properties," *RSC Adv.*, vol. 6, no. 91, pp. 88168–88173, 2016.

[20]   S. R. Gowda, A. Leela Mohana Reddy, X. Zhan, and P. M. Ajayan, "Building energy storage device on a single nanowire," *Nano Lett.*, vol. 11, no. 8, pp. 3329–3333, 2011.

[21]   K. Wan, Z.-P. Yu, and Z.-X. Liang, "Polyaniline-Derived Ordered Mesoporous Carbon as an Efficient Electrocatalyst for Oxygen Reduction Reaction," *Catalysts*, vol. 5, no. 3, pp. 1034–1045, 2015.

[22]   "Energy harvesting basic concepts." [Online]. Available: http://www.iop.org/resources/energy/.

[23]   J. P. Thomas, M. A. Qidwai, and J. C. Kellogg, "Energy scavenging for small-scale unmanned systems," *J. Power Sources*, vol. 159, no. 2, pp. 1494–1509, 2006.

[24]   F. a Hill, T. F. Havel, and C. Livermore, "Modeling mechanical energy storage in springs based on carbon nanotubes.," *Nanotechnology*, vol. 20, no. 25, p. 255704, Jun. 2009.

[25]   M. S. Rodgers, J. J. Allen, K. D. Meeks, B. D. Jensen, and S. L. Miller, "A micromechanical high-density energy storage / rapid release system," vol. 3876, p. 212-222, 1999.

[26]   M. S. Rodgers and J. J. Sniegowski, "5 Level Polysilicon Surface Micromachining Technology: Application To Complex Mechanical Systems," *Proceeding Solid State Sens. Actuator Work. Hilt. Head, S.C.*, pp. 144–149, 1998.

[27]   S. Bergbreiter, D. Mahajan, and K. S. J. Pister, "A reusable micromechanical energy storage/quick release system with assembled elastomers," *J. Micromechanics Microengineering*, vol. 19, p. 55009, 2009.

[28]   S. Shmulevich, A. Joffe, I. H. Grinberg, and D. Elata, "On the Notion of a Mechanical Battery," *J. Microelectromechanical Syst.*, vol. 24, no. 4, pp. 1085–1091, 2015.

[29]   B. Rivlin, S. Shmulevich, A. Joffe, and D. Elata, "Ben Rivlin, Shai Shmulevich, Aharon Joffe and David Elata Technion - Israel Institute of Technology Haifa 32000, Israel," no. 1, pp. 1–6, 2015.

[30] T. Chang and J. Hou, "Molecular dynamics simulations on buckling of multiwalled carbon nanotubes under bending," *J. Appl. Phys.*, vol. 100, no. 11, 2006.

[31] S. Chesnokov, V. Nalimova, a. Rinzler, R. Smalley, and J. Fischer, "Mechanical Energy Storage in Carbon Nanotube Springs," *Phys. Rev. Lett.*, vol. 82, pp. 343–346, 1999.

[32] F. A. Hill, "Energy Storage in Carbon Nanotube Super-Springs by," 2008.

[33] F. a Hill, T. F. Havel, a J. Hart, and C. Livermore, "Storing elastic energy in carbon nanotubes," *J. Micromechanics Microengineering*, vol. 19, no. 9, p. 94015, Sep. 2009.

[34] A. M. and B. T, "Continuum mechanics modeling and simulation of Carbon nanotubes Meccanica," vol. 40, no. 455, p. 69, 2005.

[35] R. Zhang, Q. Wen, W. Qian, D. S. Su, Q. Zhang, and F. Wei, "Superstrong ultralong carbon nanotubes for mechanical energy storage," *Adv. Mater.*, vol. 23, pp. 3387–3391, 2011.

[36] Z. L. Wang and J. Song, "Piezoelectric Nanogenerators Based on Zinc Oxide Nanowire Arrays," *Science (80-.).*, vol. 312, no. 5771, pp. 242–246, 2006.

[37] G. Zhu, R. Yang, S. Wang, and Z. L. Wang, "Flexible high-output nanogenerator based on lateral ZnO nanowire array," *Nano Lett.*, vol. 10, no. 8, pp. 3151–3155, 2010.

[38] H. E., "Ferroelectronics," vol. 60, no. 277–282, 1984.

[39] X. Wang, "Piezoelectric nanogenerators-Harvesting ambient mechanical energy at the nanometer scale," *Nano Energy*, vol. 1, no. 1, pp. 13–24, 2012.

[40] T. C. M.S. Majdoub, P. Sharma, "No Title," *Phys. Rev. B*, vol. 77, 2008.

[41] Z. J. and Y. Y. J. Chen C Q, Shi Y, Zhang Y S, "Phys. Rev. Lett.," vol. 96, no. 75505, 2006.

[42] M. Riaz, A. Fulati, Q. X. Zhao, O. Nur, M. Willander, and P. Klason, "Buckling and Mechanical Instability of ZnO Nanorods Grown on Different Substrates under Uniaxial Compression.," *Nanotechnology*, vol. 19, no. 41, pp. 1–9, 2008.

[43] L. Vayssieres, "Growth of arrayed nanorods and nanowires of ZnO from aqueous solutions," *Adv. Mater.*, 2003.

[44] W.-J. Lee, J.-G. Chang, S.-P. Ju, M.-H. Weng, and C.-H. Lee, "Structure-dependent mechanical properties of ultrathin zinc oxide nanowires.," *Nanoscale Res. Lett.*, vol. 6, no. 1, p. 352, 2011.

[45] U. Hill, N.A. and Waghmare, *Zinc Oxide: Fundamentals, Materials and Device Technology, Physical Review B: Condensed Matter, 62, 8802*. 2000.

[46] L. Schmidt-Mende and J. L. MacManus-Driscoll, "ZnO - nanostructures, defects, and devices," *Mater. Today*, vol. 10, no. 5, pp. 40–48, 2007.

[47] D. Chen, X. Jiao, and G. Cheng, "Hydrothermal synthesis of zinc oxide powders with different morphologies," *Solid State Commun.*, vol. 113, no. 6, pp. 363–366, 1999.

[48] H. Morkoc and U. Ozgur, *General Properties of ZnO*. 2009.

[49] R. R. F. and D. J. Baruah S, "Nano at press," 2008.

[50] H. Y. P. Yang S. Mao, R. Russo, J. Johnson, R. Saykally, N. Morris, J. Pham, R. He, H.-J. Choi, "Controlled Growth of ZnO Nanowires and Their Optical Properties," *Adv. Funct. Mater.*, vol. 12, no. 5, pp. 323–331, 2002.

[51] S. Gadag and M. Gupta, "Laser Synthesis of ZnO Nanostructures.," *Lasers Eng. Old City Publ.*, vol. 17, no. 3/4, pp. 239–250, 2007.

[52] W. N. Lee, M. C. Jeong, and J. M. Myoung, "Fabrication and application potential of ZnO nanowires grown on GaAs(002) substrates by metal-organic chemical vapour deposition," *Nanotechnology*, vol. 15, no. 3, pp. 254–259, 2004.

[53] C. G. Kuo, H. Chang, and J. H. Wang, "Fabrication of ZnO nanowires arrays by anodization and high-vacuum die casting technique, and their piezoelectric properties," *Sensors (Switzerland)*, vol. 16, no. 4, pp. 1–10, 2016.

[54] B. Weintraub, Y. Deng, and Z. Wang, "Position-Controlled Seedless Growth of ZnO Nanorod Arrays on a Polymer Substrate via Wet Chemical Synthesis," *J. Phys. Chem. C*, vol. 111, no. 28, pp. 10162–10165, 2007.

[55] A. Tsukazaki, A. Ohtomo, S. Yoshida, M. Kawasaki, C. H. Chia, T. Makino, Y. Segawa, T. Koida, S. F. Chichibu, and H. Koinuma, "Layer-by-layer growth of high-optical-quality ZnO film on atomically smooth and lattice relaxed ZnO buffer layer," *Appl. Phys. Lett.*, vol. 83, no. 14, pp. 2784–2786, 2003.

[56] P. R. Chalker, *Chemical Vapour Deposition of Metal Oxides for Microelectronics Applications*. 2009.

[57] H. Yu, Z. Zhang, M. Han, X. Hao, F. Zhu, O. Zno, and N. Nanotube, "Communication A General Low-Temperature Route for Large-Scale Fabrication of Highly Oriented ZnO Nanorod / Nanotube Arrays A General Low-Temperature Route for Large-Scale Fabrication of Highly," no. 2, pp. 2378–2379, 2005.

[58] C. . Choy, N. Wang, H. L. . Chan, X. . Zhang, H. . Ong, and J. . Dai, "Hydrothermal synthesis of oriented ZnO nanobelts and their temperature dependent photoluminescence," *Chem. Phys. Lett.*, vol. 393, no. 1–3, pp. 17–21, Jul. 2004.

[59] P. M. Aneesh, K. a. Vanaja, and M. K. Jayaraj, "Synthesis of ZnO nanoparticles by hydrothermal method," *Nanosci. …*, vol. 6639, no. 2007, p. 66390J–66390J–9, 2007.

[60] B. Baruwati, D. K. Kumar, and S. V. Manorama, "Hydrothermal synthesis of highly crystalline ZnO nanoparticles: A competitive sensor for LPG and EtOH," *Sensors Actuators, B Chem.*, vol. 119, pp. 676–682, 2006.

[61] S. Baruah and J. Dutta, "Hydrothermal growth of ZnO nanostructures," *Sci. Technol. Adv. Mater.*, vol. 10, p. 13001, 2009.

[62] L. Tang, X.-B. Bao, H. Zhou, and A.-H. Yuan, "Synthesis and characterization of ZnO nanorods by a simple single-source hydrothermal method," *Phys. E Low-dimensional Syst. Nanostructures*, vol. 40, no. 4, pp. 924–928, Feb. 2008.

[63] K. Sun, W. Wei, Y. Ding, Y. Jing, Z. L. Wang, and D. Wang, "Crystalline ZnO thin film by hydrothermal growth.," *Chem. Commun. (Camb).*, vol. 47, pp. 7776–7778,

2011.

[64] H. Wei, Y. Wu, N. Lun, and C. Hu, "Hydrothermal synthesis and characterization of ZnO nanorods," *Mater. Sci. Eng. A*, vol. 393, no. September 2004, pp. 80–82, 2005.

[65] Z. Zhang, G. Sun, F. Qi, N. Wu, J. Cao, and H. Bala, "Hydrothermal synthesis and photocatalytic property of flower-like ZnO hierarchical microstructures," vol. 523, pp. 740–745, 2012.

[66] U. Pal and P. Santiago, "Controlling the Morphology of ZnO Nanostructures in a Low-Temperature Hydrothermal Process," pp. 15317–15321, 2010.

[67] W. J. Li, E. W. Shi, Y. Q. Zheng, and Z. W. Yin, "Hydrothermal preparation of nanometer ZnO powders," *J. Mater. Sci. Lett.*, vol. 20, pp. 1381–1383, 2001.

[68] T. H. Meen, W. Water, Y. S. Chen, W. R. Chen, L. W. Ji, and C. J. Huang, "Growth Of ZnO Nanorods by Hydrothermal Method Under Different Temperatures," *2007 IEEE Conf. Electron Devices SolidState Circuits*, pp. 617–620, 2007.

[69] L. R. Goossens O, Dekempeneer E, Vangeneugden D, "Leys C. Surf Coat Technol," vol. 142–144, no. 474–81, 2001.

[70] X. Ma, H. Zhang, Y. Ji, J. Xu, and D. Yang, "Sequential occurrence of ZnO nanopaticles, nanorods, and nanotips during hydrothermal process in a dilute aqueous solution," *Mater. Lett.*, vol. 59, pp. 3393–3397, 2005.

[71] X. Ma, H. Zhang, Y. Ji, J. Xu, and D. Yang, "Sequential occurrence of ZnO nanopaticles, nanorods, and nanotips during hydrothermal process in a dilute aqueous solution," *Mater. Lett.*, vol. 59, no. 27, pp. 3393–3397, 2005.

[72] H. Y. Xu, H. Wang, Y. C. Zhang, S. Wang, M. K. Zhu, and H. Yan, "Asymmetric twinning crystals of zinc oxide formed in a hydrothermal process," *Cryst. Res. Technol.*, vol. 38, no. 6, pp. 429–432, 2003.

[73] M. Krunks and E. Mellikov, "Zinc oxide thin films by the spray pyrolysis method," *Thin Solid Films*, vol. 270, no. 1–2, pp. 33–36, 1995.

[74] J.-H. Lee, I.-C. Leu, Y.-W. Chung, and M.-H. Hon, "Fabrication of ordered ZnO hierarchical structures controlled via surface charge in the electrophoretic deposition process," *Nanotechnology*, vol. 17, no. 17, p. 4445, 2006.

[75] J. Y. Kim, J. W. Cho, and S. H. Kim, "The characteristic of the ZnO nanowire morphology grown by the hydrothermal method on various surface-treated seed layers," *Mater. Lett.*, vol. 65, no. 8, pp. 1161–1164, 2011.

[76] S. Baruah and J. Dutta, "pH-dependent growth of zinc oxide nanorods," *J. Cryst. Growth*, vol. 311, no. 3, pp. 2549–2554, 2009.

[77] A. Sugunan, H. C. Warad, M. Boman, and J. Dutta, "Zinc oxide nanowires in chemical bath on seeded substrates: Role of hexamine," *J. Sol-Gel Sci. Technol.*, vol. 39, pp. 49–56, 2006.

[78] M. N. R. Ashfold, R. P. Doherty, N. G. Ndifor-Angwafor, D. J. Riley, and Y. Sun, "The kinetics of the hydrothermal growth of ZnO nanostructures," *Thin Solid Films*,

vol. 515, no. 3, pp. 8679–8683, 2007.

[79]   F. T. O.G. Suchil, G.Abadal, "Effect of temperature and pH level on the hydrothermal growth of ZnO finewires," *Nano Energy Lett.*, vol. 5, no. February, pp. 12–14, 2013.

[80]   et al. Öztürk, Sadullah, "Fabrication of ZnO nanowires and nanorods," *Phys. E Low-Dimensional Syst. Nanostructures*, vol. 44, no. 6, pp. 1062–1065, 2012.

[81]   Y. J. and Z. Z.-K. Wang Z, Qian X-F, "No Title," *J. Solid State Chem.*, vol. 177, no. 2148, 2004.

[82]   K. Govender, D. S. Boyle, P. B. Kenway, and P. O'Brien, "Understanding the factors that govern the deposition and morphology of thin films of ZnO from aqueous solution," *J. Mater. Chem.*, vol. 14, pp. 2575–2591, 2004.

[83]   L. E. Greene, M. Law, D. H. Tan, M. Montano, J. Goldberger, G. Somorjai, and P. Yang, "General route to vertical ZnO nanowire arrays using textured ZnO seeds," *Nano Lett.*, vol. 5, no. 7, pp. 1231–1236, 2005.

[84]   L. E. Greene, M. Law, J. Goldberger, F. Kim, J. C. Johnson, Y. Zhang, R. J. Saykally, and P. Yang, "Low-temperature wafer-scale production of ZnO nanowire arrays," *Angew. Chemie - Int. Ed.*, vol. 42, no. 26, pp. 3031–3034, 2003.

[85]   Http://gwyddion.net, "gwyddion." .

[86]   G. A. and F. T. OG. Súchil, "Storing Deformation Energy of ZnO fine wires in a Mechanical Battery," *J. Phys. Conf. Ser.*, vol. 12043, no. 557, 2014.

[87]   E. G. Nicolae Lobontiu, *Mechanics of Microelectromechanical Systems*, vol. 2. 2005.

[88]   M. Riaz, a. Fulati, L. L. Yang, O. Nur, M. Willander, and P. Klason, "Bending flexibility, kinking, and buckling characterization of ZnO nanorods/nanowires grown on different substrates by high and low temperature methods," *J. Appl. Phys.*, vol. 104, no. 10, p. 104306, 2008.

[89]   T. Asahi, O. Oda, Y. Taniguchi, and A. Koyama, "Characterization of 100 mm diameter CdZnTe single crystals grown by the vertical gradient freezing method," *J. Cryst. Growth*, vol. 149, no. 1–2, pp. 23–29, 1995.

[90]   M. C. Peter Y.Yu, *Fundamentals of Semiconductors Physics and Materials Properties*. 2000.

[91]   M. Kriesch and M. Goelke, "Linear Bucklin ng Analysis," in *Linear Buckling Analysis*, 2000.

[92]   W.-F. Chen and E. M. Lui, *Structural stability : theory and implementation*. Upper Saddle River, N.J. : PTR Prentice Hall, 1987.

[93]   W. F. Chen, "Structural stability: from theory to practice," *Eng. Struct.*, vol. 22, pp. 116–122, 2000.

[94]   and R. G. B. J.E.Shigley, C.R.Mischke, *Mechanical Engineering Design, 7th ed. McGraw-Hill*. 2004.

[95]   E. O. F. Enzymes, A. From, I. Fungi, M. Characterisation, and O. F. Indoor, "Module

10," pp. 32–36.

[96] M. Riaz, A. Fulati, L. L. Yang, O. Nur, M. Willander, and P. Klason, "Bending flexibility, kinking, and buckling characterization of ZnO nanorods/nanowires grown on different substrates by high and low temperature methods," *J. Appl. Phys.*, vol. 104, no. 10, 2008.

[97] M. Riaz, a Fulati, Q. X. Zhao, O. Nur, M. Willander, and P. Klason, "Buckling and mechanical instability of ZnO nanorods grown on different substrates under uniaxial compression.," *Nanotechnology*, vol. 19, no. 41, p. 415708, Oct. 2008.

[98] M. Riaz, O. Nur, M. Willander, and P. Klason, "Buckling of ZnO nanowires under uniaxial compression," *Appl. Phys. Lett.*, vol. 92, pp. 19–22, 2008.

[99] M. Riaz, A. Fulati, G. Amin, N. H. Alvi, O. Nur, and M. Willander, "Buckling and elastic stability of vertical ZnO nanotubes and nanorods," *J. Appl. Phys.*, vol. 106, no. 3, pp. 1–7, 2009.

[100] M. Riaz, O. Nur, M. Willander, and P. Klason, "Buckling of ZnO nanowires under uniaxial compression," *Appl. Phys. Lett.*, vol. 92, no. 10, p. 3, 2008.

[101] C. Chen and J. Zhu, "Bending strength and flexibility of ZnO nanowires," *Appl. Phys. Lett.*, vol. 90, no. 4, p. 43105, 2007.

[102] L. W. Ji, S. J. Young, T. H. Fang, and C. H. Liu, "Buckling characterization of vertical ZnO nanowires using nanoindentation," *Appl. Phys. Lett.*, vol. 90, no. 3, 2007.

[103] J. M. Meza, E. E. Franco, M. C. M. Farias, F. Buiochi, and R. M. Souza, "Using the ultrasound and instrumented indentation techniques to measure the elastic modulus of engineering materials," *Rev. Met.*, vol. 44, no. 70, pp. 52–65, 2008.

[104] S. J. Young, L. W. Ji, S. J. Chang, T. H. Fang, T. J. Hsueh, T. H. Meen, and I. C. Chen, "Nanoscale mechanical characteristics of vertical ZnO nanowires grown on ZnO:Ga/glass templates," *Nanotechnology*, vol. 18, p. 225603, 2007.

[105] R. Agrawal, B. Peng, E. E. Gdoutos, and H. D. Espinosa, "Elasticity size effects in ZnO nanowires--a combined experimental-computational approach. SUPPORTING INFORMATION PARAGRAPH," *Nano Lett.*, vol. 8, pp. 3668–74, 2008.

[106] U.Ozgur, Y. I. Alivov, C. Liu, A. Teke, M. A. Reshchikov, S. Do??an, V. Avrutin, S. J. Cho, and H. Morko??, "A comprehensive review of ZnO materials and devices," *J. Appl. Phys.*, vol. 98, no. 4, pp. 1–103, 2005.

[107]   a. V. Desai and M. a. Haque, "Mechanical properties of ZnO nanowires," *Sensors Actuators, A Phys.*, vol. 134, no. April 2006, pp. 169–176, 2007.

[108] V. A. Coleman and C. Jagadish, "Basic Properties and Applications of ZnO," pp. 1–20, 2006.

[109] K. K. G. H.J. Qi, K.B.K. Teo, K.K.S. Lau, M.C. Boyce, W.I. Milne, J. Robertson, "Determination of mechanical properties of carbon nanotubes and vertically aligned carbon nanotube forests using nanoindentation, in: Proceedings of a Symposium on Dynamic Failure and Thin Film, 16 Jan- uary 2003, Pasadena, United States, 2003."

[110] S. L. X.S. Mao, M. Zhao, C.B. Jiang, "Nanomechanical behaviour of piezo- electric nanowire," *JOM 56*, vol. 261, 2004.

[111] Y.-K. K. X. Li, P. Nardi, C.-W. Back, J.-M. Kim, "Direct nanomechanical machining of gold nanowires using a nanoindenter and an atomic force microscope," *J. Micromech. Microeng*, vol. 15, no. 551–556, 2005.

[112] R. R. T. S. Bansal, E. Toimil-Molares, A. Saxena, "Nanoindentation of single crystal and polycrystalline copper nanowires, in: Proceedings of the 55th Electronic Components and Technology Conference, ECTC, 31 May–4 June 2005, Lake Buena Vista, FL, United States, 2005."

[113] W.-J. C. T.-H. Fang, "Nanolithography and nanoindentation of tantalum-oxide nanowires and nanodots using scanning probe microscopy," *Phys. B Condens. Mat. 352*, vol. 190–199, 2004.

[114] W. D. N. G. Feng, Y. Yong, C.J. Lee, K. Cho, "Mechanical properties of GaN and ZnO nanowires using nanoindentation," *JOM 56*, vol. 35.

[115] A. C. Fischer-Cripps, "A review of analysis methods for sub-micron indentation testing," *Vacuum*, vol. 58, no. 4, pp. 569–585, 2000.

[116] *Hertz H. On hardness. Verh Ver BefoK rderung Gewerbe Fleisses 1881;61:410. Translated and reprinted in English. In: Hertz's miscellaneous papers. London: Macmillan and Co., 1896 [Chapter 6]. .*

[117] *Hertz H. On the contact of elastic solids. J Reine Angew Math 1881;92:156,71. Translated and reprinted in English. In: Hertz's miscellaneous papers. London: Macmillan & Co., 1896 [Chapter 5]. .*

[118] *Oliver WC, Pharr GM. J Mater Res 1992;7(4):1564,83. .*

[119] "Catalan Institution for Research and Advanced Studies (ICREA)," *https://www.icrea.cat/. .*

[120] "Jordi Sort, ICREA Proffesor," *http://jsort-icrea.uab.cat/. .*

[121] "Ultra Micro Indentation System, UMIS 2000 by CSIRO," *https://www.csiro.au. .*

[122] "Anton Paar Table Top Nanoindentation Tester TTX-NHT2." .

[123] J. Zhou, P. Fei, Y. Gu, W. Mai, Y. Gao, R. Yang, G. Bao, and Z. L. Wang, "Piezoelectric-Potential-Controlled-Polarity-Reversible Schottky Diodes and Switches of ZnO Wires," vol. 8, no. 3973–3977, pp. 1–5, 2008.

[124] N. Focus, "Piezoelectric Picomotor 8302," *https://www.artisantg.com/info/New_Focus_8302_Datasheet.pdf. .*

[125] N. Focus, "Picomotor Controller and Driver Module, Open-Loop 4 Channel.," *Model 8742,https://www.newport.com/p/8742. .*

[126] H. Well, "Honeywell FSGSeries FSG15N1A," *Piezoresistive Force Sens.*

[127] N. Instruments, "USB-6001 DAQ," *http://sine.ni.com/nips/cds/view/p/lang/es/nid/212383.*

[128] P. C. Driver, "Model 8742," 2012.

[129] L. D. A. Q. U. S. B. Device, "Ni usb-6001/6002/6003."

[130] L. O. W. O. Voltage, L. O. W. Drift, L. O. W. Input, B. Current, H. C. Rejection, I. O. Protection, W. S. Range, L. O. W. Q. Current, P. I. N. Plasticsol-, T. Ina, B. Amplifier, T. Amplifier, R. T. D. S. Amplifier, M. Instrumentation, and D. Acquisition, "INSTRUMENTATION AMPLIFIER q DATA ACQUISITION," *Current*, pp. 1–13, 1998.

[131] L. C. Preamplifier, "Datasheet for Model SR570 Low-Noise Preamplifier," *Stanford Res. Syst.*, vol. 7, no. 408, pp. 1–54, 2005.

[132] MathWorks, "MATLAB Primer R 2015 a," p. 204, 2015.

[133] P. Anton, "Software Manual," 2011.

[134] A. Kožušníková, "Determination of Microhardness and Elastic Modulus of Coal Components by Using Indentation Method," *GeoLines*, vol. 22, pp. 40–43, 2009.

[135] I. R. Shein, V. S. Kiĭko, Y. N. Makurin, M. A. Gorbunova, and A. L. Ivanovskiĭ, "Elastic parameters of single-crystal and polycrystalline wurtzite-like oxides BeO and ZnO: Ab initio calculations," *Phys. Solid State*, vol. 49, no. 6, pp. 1067–1073, 2007.

[136] D. Kwak, J. Kim, S. Park, H. Ko, and D.-I. Cho, "Why Is (111) Silicon a Better Mechanical Material for MEMS: Torsion Case," vol. 2, no. 111, pp. 259–264, 2003.

[137] "Flexural Properties," *ASTM D790, ISO 178*. [Online]. Available: http://www.ptli.com/testlopedia/tests/flex-d790.asp.

[138] "Mechanical properties of Methacrylates."

[139] "Mechanical properties of Polycarbonates." [Online]. Available: http://matweb.com/search/DataSheet.aspx?MatGUID=84b257896b674f93a39596d00d999d77.

[140] "Mechanical properties of Acrylics."

[141] P. Antunes, F. Domingues, M. Granada, and P. André, "Mechanical Properties of Optical Fibers," *INTECH Open Access Publ.*, pp. 1–15, 2012.

[142] R. Romaniuk, "Tensile strength of tailored optical fibres," *Opto-electronics Review*, vol. 8, no. 2. pp. 101–116, 2000.

[143] G. A. Olah, A. Goeppert, and G. K. S. Prakash, "Beyond Oil and Gas: The Methanol Economy: Second Edition," *Beyond Oil Gas Methanol Econ. Second Ed.*, pp. 1–334, 2009.

[144] R. P. Sear, "Nucleation: theory and applications to protein solutions and colloidal suspensions," *J. Phys. Condens. Matter*, vol. 19, no. 3, p. 33101, 2007.

[145] K. A. Grosberg AY, *Statistical Physics of Macromolecules*. 1994.

[146] P. K. Flinn, Richard A.; Trojan, *Engineering Materials and their Applications*. 1975.

CONCEPTS